



Lida Janeth Collazos Paz

**The role of defects on the efficiency of
intermediate band solar cells based on III-V
semiconductors**

Tese de Doutorado

Thesis presented to the Programa de Pós-graduação em Engenharia Elétrica of PUC-Rio in partial fulfillment of the requirements for the degree of Doutor em Engenharia Elétrica.

Advisor : Prof. Patricia Lustoza de Souza
Co-advisor: Prof. Maurício Pamplona Pires

Rio de Janeiro
September 2019



Lida Janeth Collazos Paz

**The role of defects on the efficiency of
intermediate band solar cells based on III-V
semiconductors**

Thesis presented to the Programa de Pós-graduação em Engenharia Elétrica of PUC-Rio in partial fulfillment of the requirements for the degree of Doutor em Engenharia Elétrica. Approved by the Examination Committee.

Prof. Patricia Lustoza de Souza

Advisor

Departamento de Engenharia Elétrica – PUC-Rio

Prof. Maurício Pamplona Pires

Co-advisor

Universidade Federal do Rio de Janeiro – UFRJ

Prof. Paulo Sérgio Soares Guimarães

Universidade Federal de Minas Gerais – UFMG

Prof. Roberto Jakomin

Universidade Federal do Rio de Janeiro - Campus Xerém –

UFRJ-Xerém

Prof. Marcelo Martins Sant'Anna

Universidade Federal do Rio de Janeiro – UFRJ

Prof. Daniel Micha

Centro Federal de Educação Tecnológica - Campus Petrópolis –

CEFET-Petrópolis

Rio de Janeiro, September the 9th, 2019

All rights reserved.

Lida Janeth Collazos Paz

Graduated in physics by Universidad del Valle (Cali, Colombia), 2011. Master degree in physics by Universidade Federal do Rio de Janeiro-UFRJ (Rio de Janeiro, Brazil), 2014. Developed her doctoral research at the laboratory of semiconductors- LabSem, PUC-Rio.

Bibliographic data

Collazos Paz, Lida Janeth

The role of defects on the efficiency of intermediate band solar cells based on III-V semiconductors / Lida Janeth Collazos Paz; advisor: Patricia Lustoza de Souza; co-advisor: Maurício Pamplona Pires. – Rio de Janeiro: PUC-Rio, Departamento de Engenharia Elétrica, 2019.

v., 139 f: il. color. ; 30 cm

Tese (doutorado) - Pontifícia Universidade Católica do Rio de Janeiro, Departamento de Engenharia Elétrica.

Inclui bibliografia

1. Engenharia Elétrica – Teses. 2. Defeitos;. 3. Células solares;. 4. Eficiência de conversão de energia;. 5. Recombinação;. 6. Crescimento MOVPE.. I. Lustoza de Souza, Patricia. II. Pamplona Pires, Maurício. III. Pontifícia Universidade Católica do Rio de Janeiro. Departamento de Engenharia Elétrica. IV. Título.

CDD: 621.3

Para todas las personas, conocidas y desconocidas, que construyen este mundo con su genialidad, coraje y amabilidad... el mundo sería un aburrido lugar primitivo sin ellos.

Acknowledgments

I wish to thank my advisor, Prof. Patrícia Lustoza de Souza, for her support and comprehension during the development of my doctoral research and prof. Mohamed Henini for their kindness during my stay in England and for giving access to his DLTS lab and allow the DLTS study of my samples in his lab.

Also, I would like to thank the following individuals: prof. Rubem Sommer for providing the interface GPIB-USB to develop the PL measurements, Luciana Dornelas for her unconditional support and for growing the samples and collaborating to perform the PL measurements, Diego Gonzáles for his valuable advice and support and for developing the simulations and graphic analysis methods, and Rudy M.S.K. for his kindness and for offering me technical support in the lab.

Special thanks to my friends and colleagues of LabSem for their love and support: Elaine, Marcelo L., Eleonora, Guilherme, Lesslie, Victor C., Renato, Daniel, Roberto, José and Carlos.

Finally, I thank Conselho Nacional de Desenvolvimento Científico e Tecnológico (CNPq) for financing my doctoral scholarship and the fellowship of research in England.

Abstract

Collazos Paz, Lida Janeth; Lustoza de Souza, Patricia (Advisor); Pamplona Pires, Maurício (Co-Advisor). **The role of defects on the efficiency of intermediate band solar cells based on III-V semiconductors**. Rio de Janeiro, 2019. 139p. Tese de doutorado – Departamento de Engenharia Elétrica, Pontifícia Universidade Católica do Rio de Janeiro.

Defects present in structures of intermediate band (IB) solar cells of GaAs with InAs quantum dots (QDs) grown by MOVPE have been investigated. The three studied IB solar cells differ in the growth temperature of the spacer layers that separate the InAs QD layers in the active region and the thickness of the thin layer that capping each QD layer. Previously, the energy conversion efficiencies of these cells were measured and the cell with the highest spacer layer-growth temperature (700 °C) and thinner capping layer (3 nm) showed the highest efficiency, about 6.9%. The cells with thicker capping layers (6 nm) showed lower efficiencies, one of them, with spacer layers grown at 700 °C, reaching 5.1%, and the other one, with spacer layers grown at 600°C, reaching only 2.8%. In this work, DLTS and Laplace DLTS studies show that the cell with the lowest efficiency has the largest number and highest concentrations of defects, unlike the other two cells, which have only one trap, EL2, in lower concentrations. These results demonstrate that the different growth conditions are determinant for the formation of defects and that the defect reduction leads to the increase of the IB solar cell efficiencies. Other samples were also grown and studied by the same techniques: three solar cells with identical structure as the IB solar cells, but without QDs, and individually doped GaAs samples that represent the *p* and *n* contact sides of the IB solar cells. From the study of the cells without QDs, the origin of some defects in the IB solar cells was found to be related to the QD growth conditions or related to the spacer layer-growth temperature. The study of the GaAs samples indicated the presence of defects in the *p* and *n* sides that could trap photo-excited carriers collected through these contacts during cell operation and thus reduce the efficiency. The results of this work allow developing new strategies to improve the epitaxial growth quality of IB solar cells in the laboratory of semiconductors LabSem of PUC-Rio where the studied samples were grown.

Keywords

Defects; Solar cells; Energy conversion efficiency; Recombination; MOVPE grown.

Resumo

Collazos Paz, Lida Janeth; Lustoza de Souza, Patricia; Pamplona Pires, Maurício. **A influência dos defeitos cristalinos na eficiência de células solares de banda intermediária baseadas em semicondutores III-V**. Rio de Janeiro, 2019. 139p. Tese de Doutorado – Departamento de Engenharia Elétrica, Pontifícia Universidade Católica do Rio de Janeiro.

Neste trabalho tem sido investigado a presença de defeitos em células solares de banda intermediária (IB) de GaAs com pontos quânticos (PQs) de InAs. As três células estudadas contêm camadas de separação entre as camadas de PQs, as quais foram crescidas à diferentes temperaturas, e camadas delgadas de recobrimento dos PQs de diferentes espessuras. As eficiências de conversão de energia destas células foram medidas previamente, sendo que a célula com camadas de separação crescidas à 700 °C e com camadas de recobrimento de 3 nm é a mais eficiente (6.9%). As outras duas células com camadas de recobrimento de 6 nm apresentam menores eficiências: uma, com camadas separadoras crescidas à 700 °C, com 5.1% , e a outra, com camadas separadoras crescidas à 630 °C, com 2.8%. Estudos de DLTS e Laplace DLTS mostram que há um grande número de defeitos em altas concentrações na célula menos eficiente, enquanto nas outras duas células só é detetado o mesmo defeito EL2 em menores concentrações. Portanto, a redução dos defeitos induz o incremento da eficiência das células IB. Amostras adicionais foram crescidas e estudadas pelas mesmas técnicas, entre elas, três células solares com estruturas idênticas às das células IB, mas sem PQs, e quatro amostras GaAs mono-camada dopadas com carbono e silício, similares às camadas de contacto *p* e *n* das células IB. Do estudo das três células sem PQs foi possível determinar que alguns defeitos nas células IB são induzidos pelas condições de crescimento dos PQs ou são induzidos pela temperatura de crescimento das camadas separadoras. O estudo das amostras mono-camada indicou a presença de defeitos nos contatos *p* e *n* que podem armadilhar os portadores foto-excitados nas células sob operação e, portanto, limitar a eficiência delas. Os resultados deste trabalho contribuem para desenvolver novas estratégias para crescimento epitaxial de células IB no laboratório LabSem na PUC-Rio.

Palavras-chave

Defeitos; Células solares; Eficiência de conversão de energia; Recombinação; Crescimento MOVPE.

Table of contents

1	Introduction	19
2	Description of the project	24
2.1	Method of growth	24
2.2	Description of the samples	25
2.2.1	Additional samples: solar cells without QDs and individually doped GaAs samples	28
3	Experimental techniques	30
3.1	Deep Level Transient Spectroscopy - (Conventional DLTS)	30
3.2	Laplace DLTS - (LDLTS)	34
3.3	Instrumentation for DLTS and Laplace DLTS	37
3.4	Details of the samples and their processing for DLTS and Laplace DLTS	38
3.5	Photoluminescence - (PL)	41
3.5.1	Radiative recombinations observed in PL spectrum	42
3.5.2	Methods of analysis	46
4	DLTS and Laplace DLTS results	49
4.1	Electrical characterization	49
4.2	DLTS and Laplace DLTS results	53
4.2.1	Trap identification	59
4.2.1.1	Traps related to EL2 defect	60
4.2.1.2	Traps related to the double donor state of the Arsenic antisite and trap M3, and other traps without identification	61
4.3	Discussion of the results of DLTS and Laplace DLTS	69
4.3.1	C-doped and Si-doped GaAs samples	69
4.3.2	Solar cells without QDs	72
4.3.3	IB Solar cells	75
4.4	Summary	82
5	Photoluminescence results	84
5.1	Measured PL spectra and identification of the emission peaks	86
5.1.1	Sample p570	86
5.1.2	Sample n630	91
5.1.3	Solar cells without QDs, samples SC630, SC700, and SCycle	96
5.1.4	IB solar cells, samples QD630, QD700, and QD-s-700	105
5.2	Discussion of the PL results	117
5.2.1	PL results of the solar cells without QDs and samples p570 and n630	117
5.2.2	PL results of the IB solar cells	119
5.3	Summary	121
6	Conclusions	123
	Bibliography	126

List of figures

- Figure 1.1 Scheme of the energy ranges of the sunlight spectrum absorbed by a tandem solar cell composed by two junctions, GaInP and GaAs. The shown spectrum, AM 1.5, is one of the standard global spectra. Taken from (2). 19
- Figure 1.2 (a) Theoretical prediction of the conversion efficiency of an IB solar cell as a function of the energy level of the intermediate band (top line). This efficiency can be compared to the efficiency of a double p - n tandem solar cell (middle line) and the efficiency of a single p - n junction (bottom line). The numbers above the lines represent the band gap for each data point. Taken from (6). (b) Schematic of a typical quantum dot IB solar cell. The dots are usually doped with carriers and grown between thin spacer layers of about 100 nm, forming a stack of quantum dot layers. (c) Band diagram of an intermediate band solar cell. The intermediate band (IB) appears in the upper half of the band gap, and allows the absorption of three different photon energies: (1) E_H , corresponding to the valence band-to-IB transition, (2) E_L , corresponding to the IB-to-conduction band transition, and (3) E_G , corresponding to the band-to-band transition. The splitting of the Fermi energy due to the creation of electron-hole pairs by photon absorption is also shown. Taken from reference (8). 21
- Figure 1.3 Non-radiative Shockley-Read-Hall recombination through a defect level E_T . The energy is released by means of phonons. 22
- Figure 2.1 (a) Scheme of a MOVPE reactor, with coupled reservoirs of gas sources (hydride and MO sources), and a growth chamber. Taken from (17). (b) A general scheme of the processes involved in MOVPE growth occurring in the growth chamber. From (18). 25
- Figure 2.2 (a) Structures of the IB solar cells (QD630, QD700, and QD-s-700). (b) and (c) Structures of the solar cells without QDs (SC630, SC700, and SCycle). (d) The structure of the individually doped GaAs samples (p570, p630, n570, and n630). 26
- Figure 2.3 IV characteristics and energy conversion efficiencies of the investigated IB solar cells. The IV of a reference cell with a 1 μ m-thick GaAs active layer, equivalent to cell SC700, is also shown for comparison. Reprinted with permission after (12). 27

- Figure 3.1 Injection and subsequent emission of electrons from traps inside the depletion region of the Schottky diode by application of a bias pulse. The corresponding capacitance variation is shown on the right side. W denotes the depletion region, λ is the portion of the depletion region below the semiconductor Fermi level E_{FS} , E_{Fm} is the metal Fermi level and ΔW is the effective region contributing to the electron emission. 31
- Figure 3.2 Formation of DLTS spectrum based on the measurement of the capacitance change along the time window $[t_1, t_2]$. 32
- Figure 3.3 Example of DLTS spectra of a n -doped Si sample from reference (24). Spectra are obtained for two different bias pulses, $-2\text{ V}/0\text{ V}/-2\text{ V}$ and $-5\text{ V}/0\text{ V}/-5\text{ V}$, applied during 1 ms, and for a time window of 1/2000 s. 34
- Figure 3.4 Emission rate spectrum of an hydrogenated silicon sample containing gold (28). The corresponding DLTS spectrum (inset) shows a single broad peak centered at 260 K. The emission rate spectrum performed at 260 K reveals two defects, a gold-acceptor and a gold-hydrogen G4. 36
- Figure 3.5 (a) DLTS spectrum of sample n630. (b) Color map with the emission rate spectra of highest intensity DLTS peak as a function of temperature. The x-axis is the emission rate logarithm. The color scale represents the amplitude of spectral density function in which red is the one with highest amplitude. (c) Arrhenius type curve containing averaged emission rates calculated from the color map spectral distribution. The x-axis is the natural logarithm of averaged emission rate divided by square temperature and y-axis is the inverse temperature. The numbered points help to identify the values on both figures. 37
- Figure 3.6 Scheme of basic instruments used to DLTS and Laplace DLTS techniques. On the top, an image of the inside of cryostat where the sample device is placed. 38
- Figure 3.7 Scheme of the samples processed into devices for DLTS and Laplace measurements. The images show the final device. The pins connect the device to the instruments. 41
- Figure 3.8 Scheme of the experimental arrangement for PL measurements. The incident laser and the emitted light from the sample follow the green and red paths, respectively. 42
- Figure 3.9 Most typical radiative recombinations in semiconductors obtained by optical excitation during photoluminescence measurements. These recombinations are described in the text. 43
- Figure 3.10 Radiative recombinations in a quantum dot. The emission energies correspond to the difference between the hole and electron confined levels. 46
- Figure 4.1 Width of the depletion region of the solar cells without QDs (left) and the IB solar cells (right) as a function of the reverse bias voltage. 49

- Figure 4.2 Top: Depletion region width of the p -doped GaAs samples (left) and n -doped samples (right), with origin at metal/semiconductor interface. Bottom: Determination of carrier concentrations of the p -doped GaAs samples (left) and n -doped samples (right) from $1/C^2$ plots. 51
- Figure 4.3 $1/C^2$ plots and effective carrier concentrations of the solar cells depending on the reverse voltage, calculated from the slope of the plots. (left) Solar cells without QDs, and (right) IB solar cells. 52
- Figure 4.4 DLTS spectra (left) and corresponding Arrhenius plots (right) of the p -type doped samples ((a) and (b)), the n -type doped samples ((c) and (d)) and the solar cells without QDs ((e) and (f)). The voltage of carrier injection V_p and the reverse voltages V_r applied for the DLTS scans are detailed on the plots. The trap signatures are shown on the Arrhenius plots. 54
- Figure 4.5 (a) DLTS spectra and (b),(c) Arrhenius plots of solar cell QD630. The electron traps (majority carriers) are shown in figure (b) and the hole traps are shown in figure (c). The trap signatures are shown on the Arrhenius plots. 56
- Figure 4.6 (a) DLTS spectra and (b) corresponding Arrhenius plots of solar cell QD700. Only the traps with DLTS peaks centered around 400 K have been detected by Laplace DLTS. 57
- Figure 4.7 (a) DLTS spectra and (b) corresponding Arrhenius plots of solar cell QD-s-700. The three DLTS peaks seen at -1 V, -4 V and -6 V correspond to the same defect EL2. 58
- Figure 4.8 A possible scheme of minority injection in cells QD630 and SC630 that leads to the detection of minority carrier traps by DLTS (negative DLTS peaks). E_{Th} and E_{Te} are the energy levels of a hole trap and an electron trap, respectively. Holes are represented by circles and electrons are represented by black dots. 59
- Figure 4.9 Simulation of electric field along the active region of sample QD630 for (a) -0.25 V bias and 400 K, and for (b) -3 V bias and 300 K. These voltages and temperatures represents the parameters of detection of peaks 4*-630-0.25 and 2*-630-3. The electric field over the p and n -sides is zero. The two intense peaks seen at the edges of the active region are due to charges accumulated in the p /active region and the active region/ n interfaces. 63
- Figure 4.10 Comparison of the Arrhenius lines of hole traps of sample p630 with the ones of hole traps of the solar cells without QDs. Arrhenius line of trap E-p630 matches to the Arrhenius lines of traps A, indicating that they correspond to the same type of defect. Trap A-SC630 exhibits a slope change due to the possibly influence of electron trap H-SC630. 64
- Figure 4.11 Comparison between the Arrhenius lines of electron traps of sample QD630 obtained at -3 V and the Arrhenius line of electron trap H of sample SC630. 65

Figure 4.12 Comparison between the Arrhenius lines of electron traps C-n630 and 3-630-0.5.	67
Figure 4.13 Scheme of the possible electron emissions from the QDs to the GaAs conduction band in cell QD630.	69
Figure 4.14 Concentration of the hole traps A and EL2 detected in the active regions of the solar cells without QDs.	75
Figure 4.15 IV characteristics and percentages of the energy conversion efficiency of the IB solar cells. The IV of a reference cell with a 1 μm -thick GaAs active layer, equivalent to cell SC700, is also shown for comparison. Reprinted with permission after (12).	77
Figure 4.16 The concentration of the EL2 defect determined at the different DLTS reverse voltages in each IB solar cell. The variation of the average concentration between the cells is represented by the dotted black line.	79
Figure 4.17 External quantum efficiency (EQE) of the IB solar cells at 300 K. The light absorption by the QDs is observed within the sub-bandgap range (energy < 1.42 eV). Reprinted with permission after (12).	80
Figure 5.1 Photoluminescence spectra of sample p570 at 50 mW as a function of temperature.	87
Figure 5.2 Photoluminescence spectra of sample p570 at 20 K as a function of laser power.	88
Figure 5.3 Plots corresponding to the analysis of emissions of sample p570. The fitted peak parameters (PL Intensity, center and FWHM) are plotted as a function of temperature (left) and as a function of laser power (right).	89
Figure 5.4 Scheme of the conduction band-to-acceptor recombinations giving rise to emissions K and L at 20 K.	90
Figure 5.5 ((a) PL spectra of sample n630 at 50 mW as a function of temperature and (b) PL spectra of the same sample at 20 K as a function of laser power. Five emission peaks can be observed, including that one corresponding to the band-to-band recombination, peak ε .	92
Figure 5.6 Analysis of emission peaks emerged on the PL spectra of sample n630. The peak parameters are plotted as a function of temperature (left) and as a function of laser power (right).	93
Figure 5.7 Comparison between the PL spectra of samples p570 and n630 at 20 K and 50 mW of laser excitation.	94
Figure 5.8 Scheme of the recombination processes attributed to peaks γ , ε and θ of sample n630 at 20 K. At the right-side is also shown the recombination giving rise to peak θ at higher temperatures. The two transitions at the left-side also accounts for peaks ε_i and γ_i of the spectra of solar cells without QDs.	95
Figure 5.9 (a) PL spectra of solar cell SC630 at 50 mW as a function of temperature and (b) PL spectra of the same cell at 20 K as a function of laser power.	97

- Figure 5.10 (a) PL spectra of solar cell SC700 at 50 mW as a function of temperature and (b) PL spectra of the same cell at 20 K as a function of laser power.. 98
- Figure 5.11 (a) PL spectra of solar cell SCycle at 50 mW as a function of temperature and (b) PL spectra of the same cell at 20 K as a function of laser power. 99
- Figure 5.12 Comparison between the PL spectra of the solar cells without QDs and the PL spectrum of sample n630 at 20 K and 50 mW of excitation power. 100
- Figure 5.13 Fitted parameters of the emission peaks of sample SC630 plotted as a function of temperature (left) and as a function of laser power (right). Plot (5) only includes the FWHM of peaks γ_{LT} and ε_{LT} because the FWHM obtained for peaks α_{LT} and β_{LT} are not reliable. 102
- Figure 5.14 Fitted parameters of the PL emissions of sample SC700 plotted as a function of temperature (left) and as a function of laser power (right). 103
- Figure 5.15 Fitted parameters of the PL emissions of sample SCycle as a function of temperature (left) and as a function of laser power (right). 104
- Figure 5.16 PL spectra of solar cell QD630 at 50 mW as a function of temperature. 107
- Figure 5.17 PL spectra of solar cell QD630 at 20 K as a function of laser power. 108
- Figure 5.18 PL spectra of solar cell QD700 at 50 mW as a function of temperature. 109
- Figure 5.19 PL spectra of solar cell QD700 at 20 K as a function of laser power. The tail at the left of peak A_{HT} corresponds to peak C_{HT} . 110
- Figure 5.20 PL spectra of solar cell QD-s-700 at 50 mW as a function of temperature. The tail seen at the left of peak A_s above 75 K corresponds to peak B_s . 111
- Figure 5.21 PL spectra of cell QD-s-700 at 20 K as a function of laser power. The tail at the left of peak A_s corresponds to peak B_s . 112
- Figure 5.22 Intensity of peaks A_{LT} , A_{HT} , and A_s as a function of temperature (a) and as a function of laser power (b). 113
- Figure 5.23 Dependence of the intensities of peaks B_{LT} , C_{LT} , B_{HT} , and C_{HT} with the laser power. Peaks B_{LT} and C_{LT} are analyzed in (a), and peaks B_{HT} and C_{HT} are analyzed in (b). The behaviour of the relative intensities are also shown. 114
- Figure 5.24 (a)-(c) Illustration of the QD morphology evolution during capping layer procedure and annealing. The Indium-Gallium intermixing takes place during the capping layer growth. (d)-(e) Removal of the tip of the QD that protrudes above the capping layer by Indium flush, shown for the case of cell QD-s-700. The formation of the InGaAs layer above the QDs of this cell is also shown at the bottom. All these figures were taken from (21). 115

Figure 5.25 (a)-(c) Energies of the ground and first excited states transitions E1-H1 ad E2-H2 obtained by simulation. E1-H1 ad E2-H2 are schematized in (d). The QD PL emissions of solar cells QD630 and QD700 are compared to the simulations in (a) and (b), while the QD PL emission of cell QD-s-700 is compared to the simulations in (c). Figure (c) was taken from (21).	116
Figure 5.26 Emissions identified on the PL spectra of the solar cells QD630 (i=LT), QD700 (i=HT), and QD-s-700 (i=s). B_i and C_i are the PL emissions from the QDs and represent the ground and the first excited states transitions, respectively. The spectra of cell QD-s-700 show only the ground state transition, peak B_s .	117
Figure 5.27 Comparison between the QD emissions observed in spectra of cells QD630, QD700, and QD-s-700 below 1.45 eV (figures 5.16 to 5.21).	120
Figure A.1 Emission rate spectra of the individually doped GaAs samples p570, p630, n570, and n630 taken at -1 V.	135
Figure A.2 Emission rate spectra of the solar cells without QDs (SC630, SC700, and SCycle).	136
Figure A.3 Emission rate spectra of solar cell QD630 taken at different reverse voltages.	137
Figure A.4 Emission rate spectra of solar cell QD700 taken at different reverse voltages. The spectrum at -4 V (lower right figure) did not show clearly the peak 2-700-4 measured by DLTS around 400 K.	138
Figure A.5 Emission rate spectra of solar cell QD-s-700 taken at different reverse voltages.	139

List of tables

Table 2.1	Growth parameters of the individually doped GaAs samples which are studied to determine the defects present in the p and n -sides of the IB solar cells.	29
Table 4.1	Simulated energy levels of the QD energy states identified in cell QD630 with respect to the top of the GaAs conduction band energy barrier.	68
Table 4.2	Details of the traps detected in the active regions of the solar cells without QDs and in the individually doped GaAs samples. The hole traps are highlighted in grey. The rest of the traps are electron traps. The term un. means unidentified. The errors of ΔE_T and σ were calculated depending on the degree of fit of the Arrhenius data points to straight lines. The trap concentrations N_T were calculated from the DLTS peak heights determined by fitting the DLTS peaks with Gaussian functions. The errors of N_T derive from the degree of these fits.	70
Table 4.3	Details of the traps detected in the active regions of the IB solar cells by DLTS and Laplace DLTS. The hole traps are highlighted in grey. The rest of the traps are electron traps. The term un. means unidentified. The errors of ΔE_T and σ were calculated depending on the degree of fit of the Arrhenius data points to straight lines. The trap concentrations N_T were calculated from the DLTS peak heights determined by fitting the DLTS peaks with Gaussian functions. The errors of N_T derive from the degree of these fits.	76
Table 5.1	Thermal activation energies E_a of emissions K and L of sample p570	89
Table 5.2	Thermal activation energies E_a and constants k of the emissions of sample n630.	93
Table 5.3	Constants k of the PL emissions of the solar cells without QDs.	104
Table 5.4	Activation energies E_a and constants k of peaks A_{LT} , A_{HT} , and A_s of the spectra of the IB solar cells. These values were calculated from the intensity data shown in figures 5.22.(a) and (b).	113

List of Abbreviations

GaAs – Gallium Arsenide

InAs – Indium Arsenide

IB-SC – Intermediate Band Solar Cell

QD – Quantum dot

DLTS – Deep Level Transient Spectroscopy

LDLTS – Laplace Deep Level Transient Spectroscopy

PL – Photoluminescence

MOVPE – Metal-Organic Vapor Phase Epitaxy

... – ...

"In spite of everything I shall rise again: I will take up my pencil, which I have forsaken in my great discouragement, and I will go on with my drawing". - Vincent Van Gogh.

1 Introduction

The energy production based on fossil fuels like oil and natural gas is among the main responsible for the emission of carbon dioxide (CO_2) to the atmosphere (1). CO_2 is the most known greenhouse gas that contributes to global warming. For this reason, many efforts have been dedicated in the last decades to seek alternative energy sources less harmful to the environment. The devices based on the capture of solar energy, including the solar cells, are a special topic of investigation inside the field of alternative and renewable energy sources (2). Their energy production has increased fastly in recent years and many large photovoltaic plants have been installed around the world (3).

Currently, the tandem (or multi-junction) solar cells exhibit the highest energy conversion efficiencies, reaching a maximum of 46% of efficiency under highly concentrated sunlight (4). These cells are mostly obtained by stacking $p-n$ junctions of III-V materials, in which each junction is able to absorb energy within a different range of the sunlight spectrum, as schematized in figure 1.1. In this way, a large portion of the spectrum is covered by only one tandem solar cell. However, these cells are expensive, and for this reason, they are mostly used in space applications (5). Moreover, the lattice mismatch between the

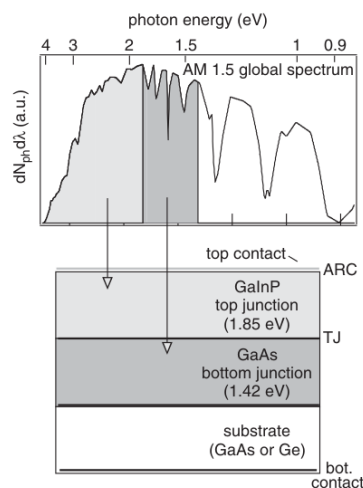


Figure 1.1: Scheme of the energy ranges of the sunlight spectrum absorbed by a tandem solar cell composed by two junctions, GaInP and GaAs. The shown spectrum, AM 1.5, is one of the standard global spectra. Taken from (2).

used materials and the bond between the p - n junctions have been the main challenges for the tandem solar cells (2).

The intermediate band (IB) solar cell is a more simple solar cell concept, based on a single p - i - n junction. These solar cells are cheaper than the tandem solar cells, and, theoretically, they can reach efficiencies as high as 63% without concentrated light, according to calculations by Luque and Martí [(6),(7)], shown in figure 1.2.(a).

The most typical IB solar cell is that with the intermediate band produced by the coupling of quantum dots (QDs), schematized in figure 1.2.(b). Several layers of QDs are distributed across a host material, in the case of the figure, GaAs, and this structure is sandwiched between two highly doped p and n layers. The intermediate band is formed by the confined energy levels for electrons in the quantum dots and, as shown in the energy band diagram of figure 1.2.(c), the IB level allows the absorption of photons with lower energy (E_L) than the energy gap of the host material (E_G). In this way, only one IB solar cell is able to absorb a broad part of the solar spectrum and this fact avoids the need to stack several p - n junctions as in the case of the tandem solar cells.

Although high efficiencies have been predicted for the IB solar cells, they have not been experimentally achieved, most likely due to the presence of undesired recombination centers and carrier traps inside the cells. Both the recombination centers and traps are defects formed in the crystalline lattices of the materials that comprise an IB solar cell and are represented by discrete energy levels lying within the band gap of the host material, figure 1.3. As shown in the figure, the defect levels serve as paths to release part of the photon energy absorbed by the cell by means of non-radiative recombinations of electrons and holes (also called *Shockley-Read-Hall recombination*). The loss of absorbed energy causes the decrease of the photocurrent collected by the solar cell, which is generated by the free electrons and free holes created by light absorption.

In a general view, the photocurrent of the cell is affected by a *recombination current* that depends on the concentrations and characteristics of the recombination centers and traps, like the capture cross-section of carriers and the energy level (E_T). The recombination current hence affects the performance of the IB solar cells, which is evidenced by low energy conversion efficiencies.

Therefore, it is desirable to reduce the concentration of defects in the layers of the cells and, for that, it is strictly necessary to identify their nature and origin. Some defects can be intrinsic or native of the semiconductor material, while others can be impurities or dopants atoms incorporated into the

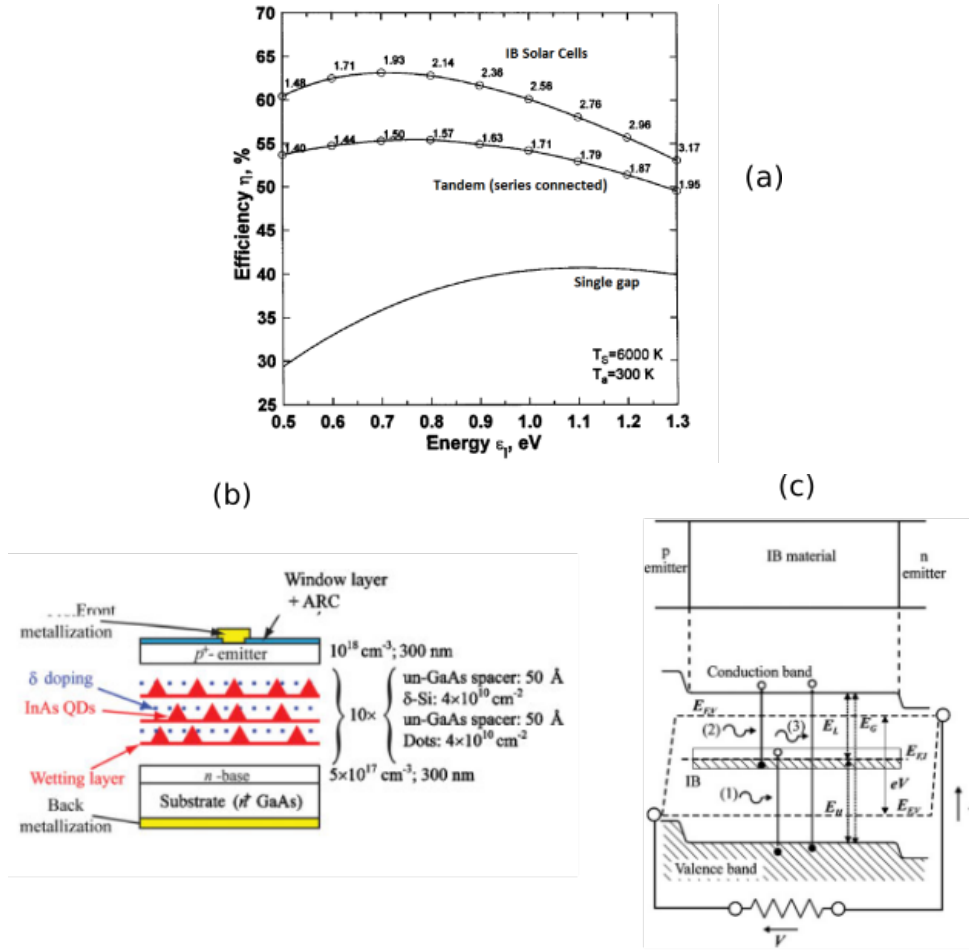


Figure 1.2: (a) Theoretical prediction of the conversion efficiency of an IB solar cell as a function of the energy level of the intermediate band (top line). This efficiency can be compared to the efficiency of a double p - n tandem solar cell (middle line) and the efficiency of a single p - n junction (bottom line). The numbers above the lines represent the band gap for each data point. Taken from (6). (b) Schematic of a typical quantum dot IB solar cell. The dots are usually doped with carriers and grown between thin spacer layers of about 100 nm, forming a stack of quantum dot layers. (c) Band diagram of an intermediate band solar cell. The intermediate band (IB) appears in the upper half of the band gap, and allows the absorption of three different photon energies: (1) E_H , corresponding to the valence band-to-IB transition, (2) E_L , corresponding to the IB-to-conduction band transition, and (3) E_G , corresponding to the band-to-band transition. The splitting of the Fermi energy due to the creation of electron-hole pairs by photon absorption is also shown. Taken from reference (8).

semiconductor lattice in substitutional or interstitial positions. Also, defects known as *complexes* can be formed by the interaction between intrinsic defects or by the interaction between impurities/dopants and intrinsic defects. But whatever the nature of the defects is, they are mainly formed during the growth step of the solar cells and, therefore, are strongly dependent on the growth

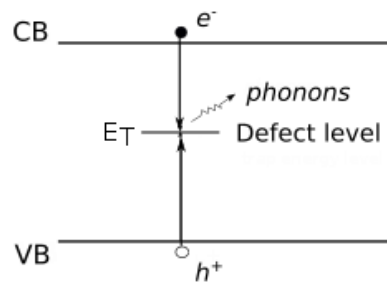


Figure 1.3: Non-radiative Shockley-Read-Hall recombination through a defect level E_T . The energy is released by means of phonons.

parameters like the growth temperature of the layers and the concentrations of doping atoms.

Improving the technology of the IB solar cell growth is then indispensable for the reduction of their defect concentrations. The current methods of epitaxial growth like Metal-Organic Vapor-Phase Epitaxy (MOVPE), Liquid-phase epitaxy (LPE), and Molecular Beam Epitaxy (MBE) have allowed a significant decrease in the concentrations of defects and impurities in semiconductor materials in comparison to older methods such as the Bridgman and Czochralski methods (9). But despite the high-quality production achieved by the epitaxial techniques, defects are still formed in the materials as a consequence of some non-optimal growth conditions.

A large variety of defects can be found in the literature for different types of combinations of semiconductor materials, mainly, for III-V compounds, and for different types of epitaxial growth techniques. However, only a few reports about defects in solar cell structures have been published up to now. [(10), (11)]. The structure of the cells of these studies are very simple and do not contain more complex sub-structures like quantum wells and quantum dots which may be constituents of solar cells. Moreover, there is not any similar work in the literature, to our knowledge, for the special case of the IB solar cells. Therefore, there is still much room within the field of defects in solar cells to be explored.

Precisely, the aim of this work is to perform experimental studies to identify the defects present in the individual layers of IB solar cells of Gallium Arsenide (GaAs) with quantum dots of Indium Arsenide (InAs) grown by MOVPE, and determine the dependence of the found defects on the growth parameters. Based on these dependencies, we will establish the influence of the defects on the efficiencies of the solar cells. Furthermore, from the results of this work, new strategies shall derive to improve the quality of the epitaxial

growth of IB solar cells, in particular, the quality of IB solar cells grown in the laboratory of semiconductors LabSem of PUC-Rio where the investigated IB solar cells were grown.

2

Description of the project

Three IB solar cells were chosen to investigate the influence of crystalline defects on their energy conversion efficiencies. These cells were grown by the LabSem group [(12), (13)]. A series of additional samples were also grown with the aim to determine the influence of the growth parameters of these IB solar cells on the crystalline defects.

A brief description of the method of growth of the IB solar cells and the additional samples, as well as the description of their structures, are presented in the following sections.

2.1

Method of growth

The solar cells were grown by MOVPE (metal-organic vapor phase epitaxy) [(14), (15)], also called MOCVD. This epitaxial technique is broadly used in the industry of semiconductors where the purpose is large-scale production with high crystalline quality. The growth takes place inside a reactor chamber to where the gas sources are transported, as schematized in figures 2.1.(a). These sources contain the chemical elements necessary to grow the solid sample, in our case, Arsenic and Gallium, and are mixed with a carrier gas, usually hydrogen. The molecules of the gas sources are decomposed at high temperatures (> 450 °C) as shown by figure 2.1.(b), and the resulting species diffuse to the growth surface, where they can be adsorbed and incorporated into the solid. These processes are highly complex and cannot be totally controlled, so that some undesired impurities are also incorporated, as is the usual case of the residual carbon, attributed to species resulting from the decomposition of TMGa (16).

The Arsenic and Gallium sources for our solar cells were Arsine (AsH_3) and the metal-organic Trimethylgallium or TMGa ($Ga(CH_3)_3$), respectively. To the silicon and carbon doping, the silane (SiH_4) and tetrabromocarbon (CBr_4) precursors were used, respectively.

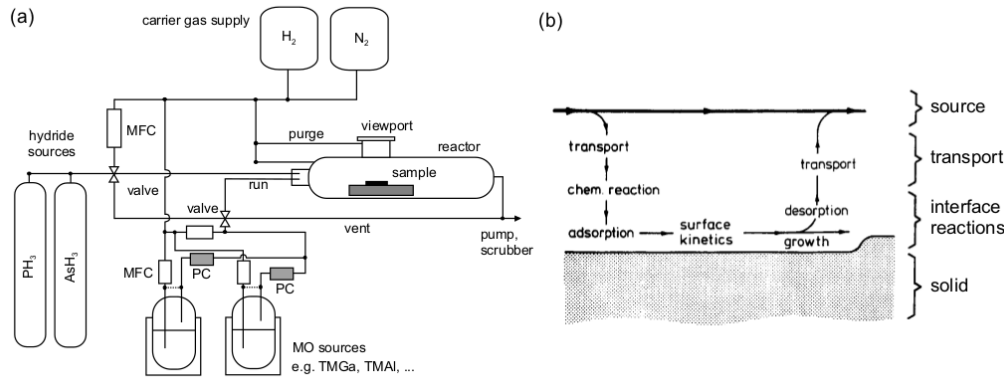


Figure 2.1: (a) Scheme of a MOVPE reactor, with coupled reservoirs of gas sources (hydride and MO sources), and a growth chamber. Taken from (17). (b) A general scheme of the processes involved in MOVPE growth occurring in the growth chamber. From (18).

2.2 Description of the samples

The structure of the IB solar cells, named QD630, QD700, and QD-s-700, consists of a *p-i-n* junction, shown schematically in figure 2.2.(a), in which the *i*-side, also called the *active region*, is the side comprising the stack of QDs of InAs (10 layers of QDs). The confined energy levels for electrons of these QDs form the intermediate band of each cell. The *n*-side is the first side to be grown, followed by the growth of the active region, and ending with the growth of the *p*-side. The *n* side is formed by two silicon-doped (or Si-doped) GaAs layers and a Si-doped AlGaAs layer grown at 630 °C. The *p*-side is formed by two carbon-doped (or C-doped) GaAs layers, grown at 570 °C, and an optical window layer of GaInP doped with zinc and grown at 630 °C. This window layer is used to passivate the carrier recombination on the *p*-side surface due to surface states, some of them formed during post-growth processing.

The sequence to grow the active region is as follows: first, an undoped GaAs layer is grown at 630 °C, followed by the growth of a Si-doped InAs layer of just 0.74 nm at 500 °C (InAs wetting layer). The QDs are formed at this step as a consequence of the mismatch between the lattice parameters of InAs and GaAs. This method of growth is the well-known Stranski–Krastanov self-assembly mode (19). After this step, the QDs are covered with a thin *capping GaAs layer* (of thickness h_{CL}) grown at the same temperature as that for the InAs layer, and later, the QDs are annealed at a higher temperature T_g . The covering and annealing of the QDs correspond to the Indium flush method [(20), (21)], which allows the control of the QD height by removing the tip of the QD that protrudes above the capping layer. Then, the indium flush

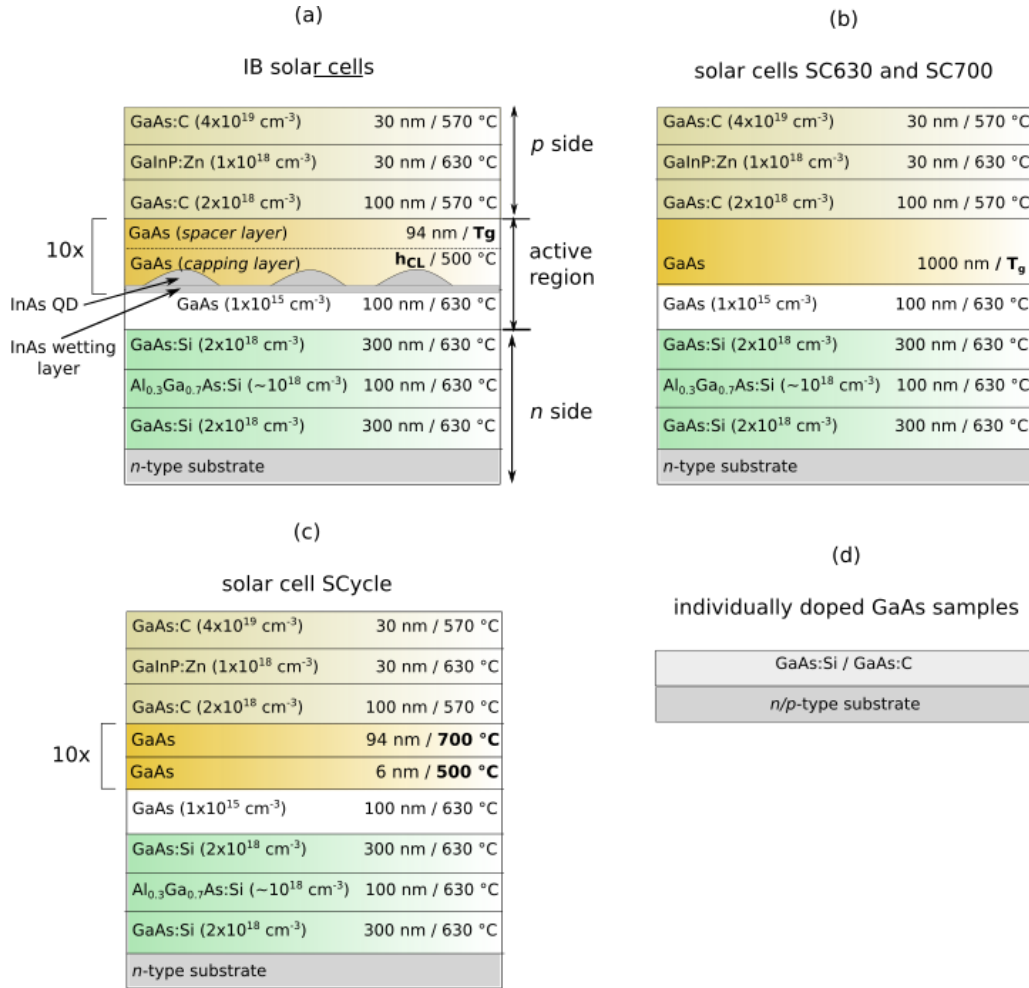


Figure 2.2: (a) Structures of the IB solar cells (QD630, QD700, and QD-s-700). (b) and (c) Structures of the solar cells without QDs (SC630, SC700, and SCycle). (d) The structure of the individually doped GaAs samples (p570, p630, n570, and n630).

prevents the formation of QDs with heights higher than the thickness of the capping layer. Finally, a thick *GaAs spacer layer* is grown above the capping layer at the same temperature T_g . The described sequence is repeated 10 times to form the active region.

The (nominal) doping concentrations of the layers of the structure are based on previous calibration data. According to these data, the undoped GaAs layer at the bottom of the active region, grown at 630 °C, and the undoped GaAs capping layers, grown at 500 °C, have residual *p*-type concentrations of the order of 10^{15} cm^{-3} . Since the InAs layers are Si-doped, the QDs are *n*-type doped with a concentration of about $2 \times 10^{17} \text{ cm}^{-3}$.

The structures of the three solar cells QD630, QD700, and QD-s-700 differ in two growth parameters of the active region: the thickness of the capping layers h_{CL} , and the growth temperature of the spacer layers T_g , which is the

same temperature for the QD annealing. These parameters have the following values:

- cell **QD630**: $T_g = 630$ °C, $h_{CL} = 6$ nm
- cell **QD700**: $T_g = 700$ °C, $h_{CL} = 6$ nm
- cell **QD-s-700**: $T_g = 700$ °C, $h_{CL} = 3$ nm

The respective temperatures T_g are indicated in the names of cells. The name of cell QD-s-700 includes the letter *s* to distinguish it from cell QD700 and to indicate the smaller thickness of its capping layers. The spacer layers grown at 630 °C and 700 °C have doping concentrations close to $1 \times 10^{15} \text{ cm}^{-3}$ according to the calibration data.

As observed from the IV characteristics of the three IB solar cells, figure 2.3, cells QD700 and QD-s-700, with spacer layers grown at 700 °C, exhibit the highest efficiencies (about 5.1% and 6.9%, respectively), while cell QD630, with spacer layers grown at 630 °C, shows the lowest efficiency (about 2.8%). The additional increase in efficiency shown by cell QD-s-700 in comparison to cell QD700 is obtained due to the reduction of the thickness of the capping layers.

Precisely, the aim of this work is to investigate the defects present in the active regions of the three solar cells QD630, QD700, and QD-s-700, relate their presence to the different growth conditions, and determine whether they affect the efficiency of the cells. The techniques chosen for the detection of defects in the solar cells are the conventional deep-level transient spectroscopy (DLTS), Laplace DLTS, and Photoluminescence (PL). These techniques will be described in detail in the next chapter.

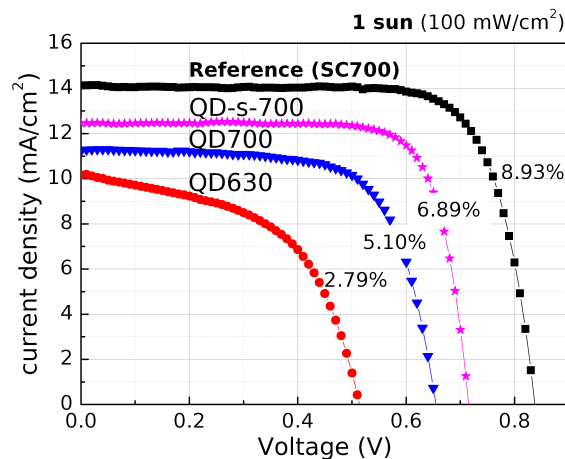


Figure 2.3: IV characteristics and energy conversion efficiencies of the investigated IB solar cells. The IV of a reference cell with a $1 \mu\text{m}$ -thick GaAs active layer, equivalent to cell SC700, is also shown for comparison. Reprinted with permission after (12).

2.2.1

Additional samples: solar cells without QDs and individually doped GaAs samples

Additional solar cells with exactly the same structure of the IB solar cells but without QDs in the active region were grown in order to be able to eventually identify defects introduced solely by the QDs. These cells were also grown by the MOVPE technique and have the structures shown in figure 2.2.(b). The description of these cells are as follows:

- **cell SC630:** the structure of this cell recreates the structure of cell QD630 without QDs. Its active region consists of an undoped GaAs layer of 1100 nm grown at 630 °C.
- **cell SC700:** the structure of this cell corresponds to the same structure of cell QD700 but without QDs. Its active region is formed by two undoped GaAs layers, one of them of 1000 nm-wide, grown at 700 °C (at the top), and the other one of 100 nm-wide and grown at 630 °C (at the bottom).

A third solar cell without QDs, shown in figure 2.2.(c), was grown to include the temperature cycle to which the QDs of cells QD700 and QD-s-700 are submitted during growth. This cycle consists of the growth of the QDs at 500 °C, followed by the subsequent annealing at 700 °C. The description of the structure of this solar cell is as follows:

- **cell SCycle:** this cell has the same p and n -sides as the IB solar cells do. Its active region is formed by one undoped GaAs layer of 100 nm grown at 630 °C (at the bottom), and a pair of undoped GaAs layers (at the top): one of 6 nm and grown at 500 °C, and the other one of 94 nm and grown at 700 °C. This pair is repeated 10 times.

Cell SCycle has been studied to determine which defects in the active region are influenced or induced by the growth temperature cycle of the QDs.

It is worth to note that the active regions of all the cells without QDs have the same total thickness as the active regions of the IB solar cells (1100 nm). The doping concentrations of all the undoped GaAs layers grown between 500 °C and 700 °C are of the order of 10^{15} cm^{-3} .

The presence of defects in the p and n -sides of the IB solar cells was also determined based on four individually C-doped and Si-doped GaAs samples. These samples recreate separately the C-doped and Si-doped layers of the p and n -sides. The structure of these samples is schematized in figure 2.2.(d), while their growth parameters are shown in table 2.1. Sample p570 was grown

C-doped GaAs samples			
	layer thickness	doping concentration	growth temperature
p570	271 nm	$1.1 \times 10^{17} \text{ cm}^{-3}$	570 °C
p630	1000 nm	$2.4 \times 10^{16} \text{ cm}^{-3}$	630 °C
Si-doped GaAs samples			
n570	600 nm	$6.5 \times 10^{16} \text{ cm}^{-3}$	570 °C
n630	1000 nm	$1.1 \times 10^{17} \text{ cm}^{-3}$	630 °C

Table 2.1: Growth parameters of the individually doped GaAs samples which are studied to determine the defects present in the p and n -sides of the IB solar cells.

at 570 °C like the respective layers of the p -side. Similarly, sample n630 was grown at 630 °C as the layers of the n -side.

On the other hand, sample p630 was designed to study the effect of the higher growth temperature of the window GaInP layer (630 °C) on the defects of the p -side. In a similar way, sample n570 was designed to study the influence of the lower growth temperatures, to which each IB solar cell is subjected after the n -side is grown, on the defects on this side.

The solar cells without QDs and the individually doped GaAs samples were also studied by DLTS, Laplace DLTS and PL. The processing of the samples necessary for DLTS and Laplace DLTS measurements will be described in detail in the next chapter.

3

Experimental techniques

In this chapter will be presented the theory related to the techniques used to detect defects in the samples under investigation. The used techniques are three: the two electrical techniques of DLTS and Laplace DLTS, and the optical technique of Photoluminescence. These techniques will be described in detail in the next sections.

3.1

Deep Level Transient Spectroscopy - (Conventional DLTS)

This technique developed by (22) in 1974 is a common tool of detection of traps in semiconductor materials. It allows the estimation of trap concentration and can also identify them to be holes or electrons traps. The DLTS technique is based on the measurement of capacitance transient of a semiconductor device during carrier thermal emission from traps to conduction or valence band after carrier injection by an applied pulse bias. A Schottky diode is formed by evaporation of a metal with a suitable work function on the semiconductor surface of the investigated material ¹. As it is known, a Schottky diode behaves as a simple parallel plate capacitor when reverse biased and its charge is stored within a depletion region which begins at the metal/semiconductor interface and extends into the semiconductor side. The depletion thickness increases as the reverse voltage increases. In DLTS, the traps enclosed by the depletion region are thermally activated and emit their trapped carriers to the bands, inducing a capacitance change in time. Measuring this capacitance change allows the detection of the traps and the estimation of their concentration.

Usually, the majority carrier traps are of main interest and much easier to measure than the minority carrier traps as it is the case of this work. For this purpose, the traps are filled with majority carriers by submitting the Schottky diode to a bias pulse whose bottom reverse voltage is V_r and top is $0V$, as shown on the left side of figure 3.1. In this figure, the energy band diagram of a Schottky diode formed by the union of an n -type semiconductor and a metal is schematized as an example. The semiconductor has electron traps of a single

¹ $\phi_m > \phi_s$ for n -type semiconductor and $\phi_m > \phi_s$ for p -type, where ϕ_m, ϕ_s are the work functions of metal and semiconductor, respectively

energy level E_T . When the diode remains biased at a specific reverse voltage as shown in figure 3.1.(a), most of the traps inside the depletion region have their corresponding energy level above the semiconductor Fermi level E_{FS} , and hence they are empty of electrons. The capacitance of the diode, seen on the right side of the figure, is at its stationary value C_2 . However, when the voltage jumps to $0V$ as seen in figure 3.1.(b), these traps fall below the level E_{FS} , so they can be filled with electrons (majority carriers). After returning rapidly to reverse voltage, figure 3.1.(c), the traps along ΔW are again above the level E_{FS} and, therefore, they are forced to emit the electrons to the conduction band. Meanwhile, the capacitance does not return immediately to its stationary value but increases exponentially until the traps are emptied. The case of a Schottky diode formed with a p -type semiconductor is analogous: hole traps with energy level E_T are injected and subsequently emptied, emitting holes to the valence band and producing the same exponential decay of capacitance to

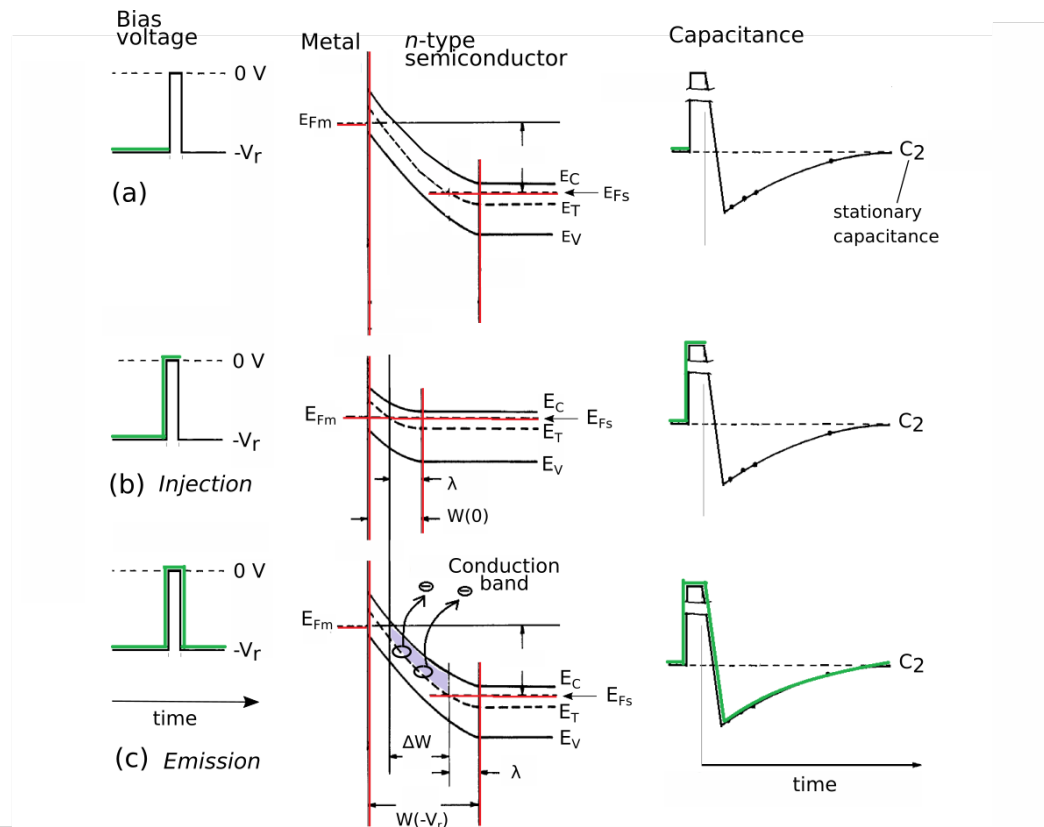


Figure 3.1: Injection and subsequent emission of electrons from traps inside the depletion region of the Schottky diode by application of a bias pulse. The corresponding capacitance variation is shown on the right side. W denotes the depletion region, λ is the portion of the depletion region below the semiconductor Fermi level E_{FS} , E_{Fm} is the metal Fermi level and ΔW is the effective region contributing to the electron emission.

its stationary value.

In this way, the capacitance change evidences the presence of the trap energy level E_T . The decay time constant defining the capacitance transient curve is the inverse of the emission rate of carriers e_j , which characterizes the particular trap level E_T :

$$C_2 - C(t) \propto \exp(-e_j t) \quad (3-1)$$

In addition, the emission rate depends on the temperature of the diode as follows (22):

$$e_j = A m_e^* \sigma_j T^2 \exp[-(\Delta E_T)/K_B T] \quad (3-2)$$

where A is a constant independent of temperature, m_e^* is the majority carriers effective mass, σ_j is the capture cross-section of the traps and ΔE_T is the difference between the conduction band minimum level and the trap energy level (or in the case of hole traps, the difference between the trap energy level and the valence band maximum level). ΔE_T is also called *thermal activation energy*.

The detection of the trap level by DLTS is made by defining a *time window* $[t_1, t_2]$ of about 1 ms, which serves to measure variations of capacitance and give rise to the DLTS spectrum, as schematized in figure 3.2. The capacitance variation along the window ($C(t_2) - C(t_1)$) is registered as the DLTS signal, and this signal is recorded as the temperature increases, forming the spectrum seen at the right side of the figure. The maximum signal ΔC_0 (the top of the peak) is reached when the trap emission rate is within the window. Following equation 3-1, the signal can be mathematically described

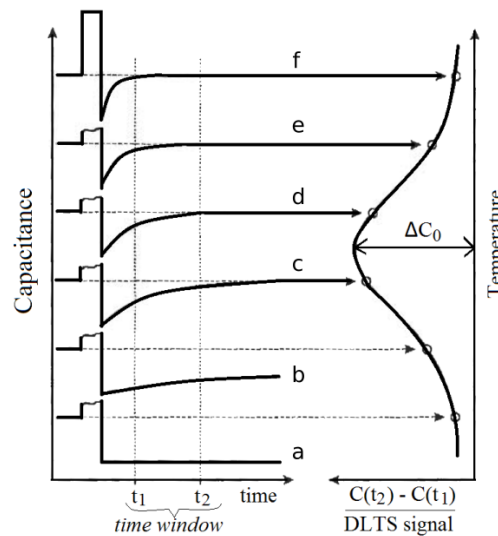


Figure 3.2: Formation of DLTS spectrum based on the measurement of the capacitance change along the time window $[t_1, t_2]$.

as follows, according to Lang (22):

$$C(t_2) - C(t_1) \propto \exp(-e_j t_1) - \exp(-e_j t_2) \quad (3-3)$$

The two equations 3-2 and 3-3 explain the variation of the DLTS signal with the temperature. At very low temperature e_j and $C(t_2) - C(t_1)$ approach zero, therefore, there is no carrier emission and the capacitance is kept constant, as observed in the lowest curve of figure 3.2, curve a. e_j and $C(t_2) - C(t_1)$ gradually increase with raising temperature, so the carrier emission takes place and the amount of emitted carriers to the conduction (or valence) band gradually increases. The capacitance transient takes an exponential form, as observed in curves b and c. At higher temperatures, the emission rate e_j reaches relative high values, so the carrier emission is faster and the capacitance decays rapidly to its stationary value C_2 within a time equal or shorter than t_2 , as observed in curves d and e. In curve f, the decay takes a shorter time than t_1 , hence the reason to measure no signal between t_1 and t_2 ($C(t_1) = C(t_2) = C_2$).

The maximum DLTS signal ΔC_0 helps to determine the concentration of the corresponding trap:

$$N_T \approx 2N_d \Delta C_0 / C_2 \quad (3-4)$$

where N_d is the concentration of majority carriers. A more accurate calculation of N_T takes into account that the effective region contributing to emission is not the entire depletion region, but ΔW (23). The equation above takes the following form:

$$N_T = 2N_d \frac{\Delta C_0}{C_2} \left\{ \frac{W^2(V_r)}{(W(V_r) - \lambda)^2 - (W(0) - \lambda)^2} \right\} \quad (3-5)$$

with

$$\lambda = \left\{ \frac{2\varepsilon}{e^2 N_d} (E_F - E_T) \right\}^{1/2} \quad (3-6)$$

where $W(V_r)$ and $W(0)$ represent the depletion depth at reverse bias and zero bias, respectively. ε is the GaAs permittivity and E_F is the Fermi energy level. E_F is determined based on the carrier concentration. For n -type semiconductor:

$$E_{Fn} = E_i + K_B T \ln \left(\frac{N_d}{n_i} \right) \quad (3-7)$$

where K_B is the Boltzmann constant and E_i and n_i are the intrinsic Fermi level and the intrinsic carrier concentration of undoped GaAs at the temperature T , respectively.

Until here it was supposed an amount of traps within the depletion region corresponding to a single defect defined by the energy level E_T . However, several types of defects can be within the depletion region. A distribution of

energy levels of defects across the band gap separated down to 200 meV from each other can be easily resolved on the DLTS spectrum. In this case, the DLTS spectrum consists of a set of peaks in which each one represents a single defect. The distribution of these peaks over the spectrum is also explained following equation 3-2. Shallow defects with energy level close to the conduction or valence band, i.e., low activation energy ΔE_T , have higher emission rates and then they are detected at lower temperature. Defects deeper inside the band gap with higher activation energies and lower emission rates appear at higher temperatures on the right side of the spectrum. An example is shown in fig.3.3 for an n -doped Si sample. Two defects E_{Si1} and E_{Si2} with levels at 0.25 eV and 0.47 eV below the conduction band minimum level appear on the spectrum, respectively. E_{Si2} is best resolved when using a higher reverse bias of -2 V, letting a trap concentration of about one order of magnitude lower than the trap concentration of E_{Si1} .

In this work DLTS spectra were recorded at a constant heating rate of 2 K/min from 10 K or 50 K to 450 K. The investigated samples were submitted to single bias pulses of 1 ms every 1 K or 2 K whereas the signal was recorded along a window time of 1/200 s and within a 20 pF scale.

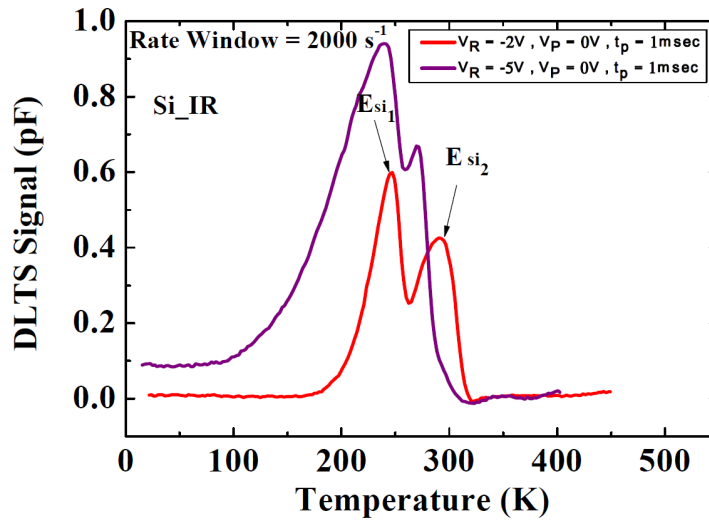


Figure 3.3: Example of DLTS spectra of a n -doped Si sample from reference (24). Spectra are obtained for two different bias pulses, -2 V/0 V/-2 V and -5 V/0 V/-5 V, applied during 1 ms, and for a time window of 1/2000 s.

3.2 Laplace DLTS - (LDLTS)

In addition to the conventional DLTS, a second technique to determine the thermal activation energies and capture cross-sections of the defects detected by DLTS is required. These two parameters are the *fingerprints* that

characterize a particular defect. Laplace Deep Level Transient Spectroscopy – LDLTS or Laplace DLTS (25, 26) was the chosen complementary technique. Laplace DLTS not only allows the estimation of the defect parameters, but also addresses the broadening of the peaks derived mainly from instrumental effects and thermal broadening. Additionally, this technique is able to resolve overlapped peaks on the DLTS spectrum, corresponding to defects with very similar energy levels (or close emission rates). In Laplace DLTS, a capacitance transient, measured at a fixed temperature, is defined by an emission rate spectrum rather than a single emission rate, as in conventional DLTS described by equation 3-1. The capacitance transient signal can be fitted by the following function:

$$f(t) = \int_0^{\infty} F(s)e^{-st}ds \quad (3-8)$$

where s is the variable representing the emission rate values and $F(s)$ is the spectral density function, i.e., the contribution weight of each defect to the emission. A mathematical representation of $f(t)$ is the Laplace transform of the spectral density function $F(s)$. Thus, it is necessary to use a mathematical algorithm to apply an inverse Laplace transform to the function $f(t)$ in order to obtain the emission rate spectrum. In this work, the algorithms CONTIN, FTIKREG and FLOG were used, but their description will not be offered here because it is out of the scope of this thesis. The reference (27) contain further information. The resulting spectrum is an intensity output as a function of emission rate in which delta-like peaks are observed. Each one of these peaks represents a single defect. An example of emission rate spectrum obtained by Laplace DLTS is shown in fig.3.4, where a better resolution of two defects in a silicon sample at 260 K is observed.

The Laplace DLTS scan is similarly performed as in conventional DLTS, i.e., applying the same bias pulse to the semiconductor device for thermal carrier emission and recording the resulting capacitance transient, except that this time the inverse Laplace algorithms is applied to the transient in order to obtain the corresponding emission rate spectrum, specifically, one emission rate spectrum for each fixed temperature. The Laplace DLTS scan takes a long time when performed as a function of temperature. For this reason, the scan is performed only within the temperature ranges of the DLTS peaks. More precisely, several emission rate spectra are obtained at different fixed temperatures within the DLTS peaks temperature range. The chosen temperatures to calculate the emission rate spectra of a peak were every 2 K or 3 K around the temperature for which the DLTS signal is maximum.

In this work, the emission rate spectra of the samples as a function of temperature have been collected in color maps like the one of figure 3.5.(b).

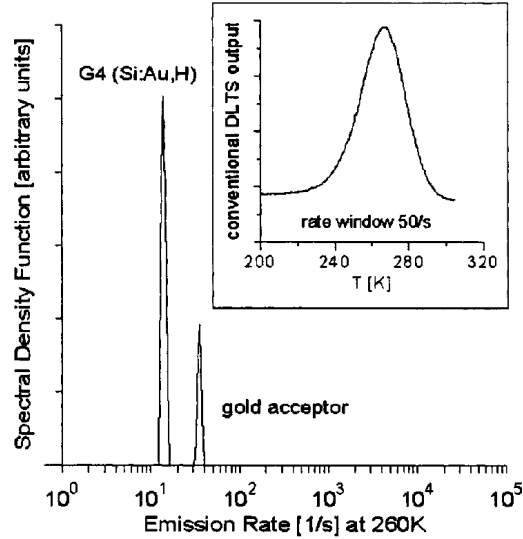


Figure 3.4: Emission rate spectrum of an hydrogenated silicon sample containing gold (28). The corresponding DLTS spectrum (inset) shows a single broad peak centered at 260 K. The emission rate spectrum performed at 260 K reveals two defects, a gold-acceptor and a gold-hydrogen G4.

This figure shows a single defect evidenced by a highest intensity red region that moves to the right as the temperature increases from 350 K to 425 K. This peak corresponds to the DLTS peak around the same temperature region of figure 3.5.(a). The displacement is due to the increase in emission rate, according to equation 3-2. To calculate the thermal activation energy and the capture cross-section of the defect, an Arrhenius type curve, seen in figure 3.5.(c), is plotted with the averaged emission rates per temperature, calculated from the spectral distribution of color map (black points). The linear behavior seen in the Arrhenius curve is in agreement with the linear form of equation 3-2:

$$\ln(\langle e_j \rangle / T^2) = \ln(Am_e^* \sigma_j) - \Delta E_T / K_B T \quad (3-9)$$

where $\langle e_j \rangle$ now represents the averaged emission rate per temperature. The thermal activation energy and capture cross-section are easily extracted from the linear regression of the Arrhenius curve. Frequently, these values are called *apparent* activation energy and *apparent* capture cross-section, since this last one has been considered as non-dependent on temperature. Some defects exhibit a capture cross-section dependent on temperature in an exponential form, so the term σ_j is replaced by the term $\sigma_j(T) = \sigma_\infty \exp(-E_a / K_B T)$, where σ_∞ and E_a are constants independent of temperature. In this case, the apparent activation energy is the sum of ΔE_T and the constant E_a , whereas the apparent capture cross-section is σ_∞ .

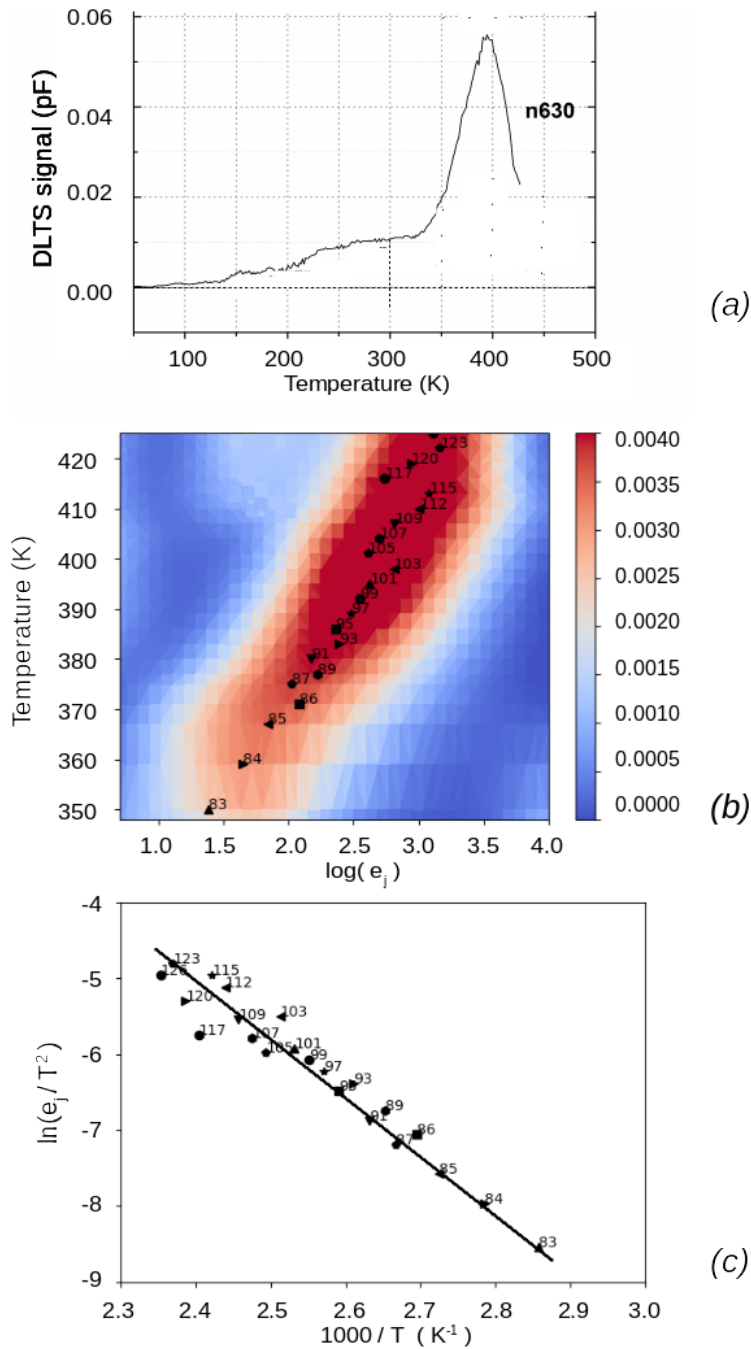


Figure 3.5: (a) DLTS spectrum of sample n630. (b) Color map with the emission rate spectra of highest intensity DLTS peak as a function of temperature. The x-axis is the emission rate logarithm. The color scale represents the amplitude of spectral density function in which red is the one with highest amplitude. (c) Arrhenius type curve containing averaged emission rates calculated from the color map spectral distribution. The x-axis is the natural logarithm of averaged emission rate divided by square temperature and y-axis is the inverse temperature. The numbered points help to identify the values on both figures.

3.3 Instrumentation for DLTS and Laplace DLTS

The instrumentation was exactly the same for the two techniques: DLTS and Laplace DLTS. Basically, four instruments were used: a cryostat to host

the sample during the temperature variation from 10 K up to 420 K, a capacitance meter of high resolution (lower than 0.01 pF) to measure variations in capacitance, a temperature controller to rise the sample temperature through a heater inside the cryostat and an interface unit to convert the temperature and capacitance measurements into data signals. This interface unit also enables the application of the bias pulses. The signals are processed by a special software that reads the capacitance transient variations and generates a DLTS spectrum. In the case of Laplace DLTS technique, a spectrum is not obtained. Instead, as explained in the last section, the device temperature is kept at a fixed value, the bias pulse is applied and then the resulting capacitance transient is recorded. An additional tool of the software is used to apply an inverse Laplace transform to the capacitance transient and draw an emission rate spectrum like the one of figure 3.4. Because of the great number of spectra recorded for each sample as a function of temperature, it was much better to construct color maps with all the spectra, as described in the last section.

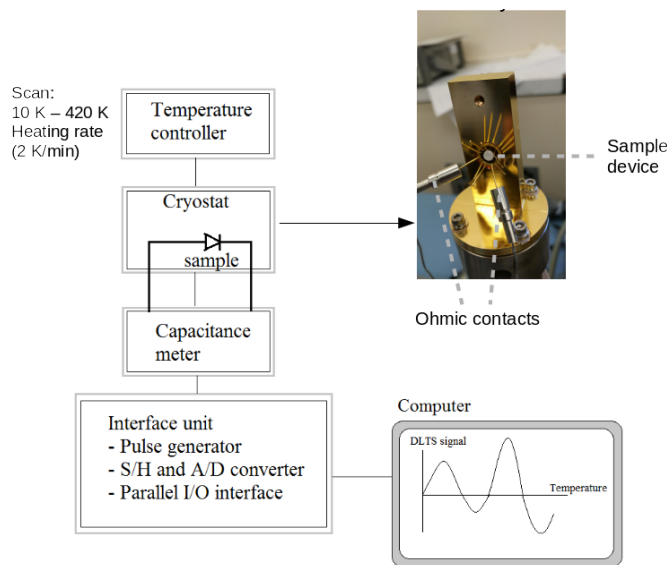


Figure 3.6: Scheme of basic instruments used to DLTS and Laplace DLTS techniques. On the top, an image of the inside of cryostat where the sample device is placed.

3.4

Details of the samples and their processing for DLTS and Laplace DLTS

The samples were processed into appropriate devices before being subjected to DLTS and Laplace DLTS scans. As explained in section 3.1, every sample should be adapted as a Schottky diode, so that the defects enclosed by the induced space-charge localized within the semiconductor side can be

detected by the DLTS and Laplace DLTS techniques. However, in this work only the individually doped GaAs samples (n570, n630, p570 and p630) were processed as Schottky diodes. The other ones, the solar cells with and without quantum dots have been processed into a different type of device since they are $p^+ - n - n^+$ and $p^+ - p - n^+$ junctions, respectively.

In the case of solar cells without QDs (SC630, SC700 and SCycle), the active region (i -region) has a slight p -type concentration of about $1 \times 10^{15} \text{ cm}^{-3}$ due to residual impurities according to the nominal doping concentrations. The p and n sides have similar concentration levels of about 10^{18} cm^{-3} . Therefore, these cells are $p^+ - p - n^+$ junctions. Each p side includes a top C-doped GaAs layer with doping concentration of $4 \times 10^{19} \text{ cm}^{-3}$, which acts as an additional p^{++} side of 30 nm thick. However, the DLTS measurements have been focused on the $p^+ - p - n^+$ regions, as will be shown in the section of electrical characterization of the next chapter. For this reason, the p^{++} side can be disregarded in the present discussion.

Concerning the IB solar cells (QD630, QD700 and QD-s-700), the doping concentration levels of the p and n sides are the same as for the previous solar cells, but the active region contains n -type InAs QD layers separated by GaAs spacer and capping layers which are expected to have residual p -doping concentration of about $1 \times 10^{15} \text{ cm}^{-3}$. Since the QD n -doping exceeds the residual p -doping concentration of the GaAs layers, the net concentration of the active region should be n -type. This fact is confirmed by the following simple calculation, taking an average between the different layers:

$$\begin{aligned}
 \langle N \rangle &= -2 \times 10^{17} \text{ cm}^{-3} \times V[\text{InAs layers}] \\
 &\quad + 1 \times 10^{15} \text{ cm}^{-3} \times V[\text{GaAs spacer layers}] \\
 &\quad + 1 \times 10^{15} \text{ cm}^{-3} \times V[\text{GaAs capping layers}] \\
 &\quad + 1 \times 10^{15} \text{ cm}^{-3} \times V[100\text{nm} - \text{bottom GaAs layer}] \quad (3-10)
 \end{aligned}$$

where V is the volume fraction occupied within the active region by each type of layer. The resulting net concentrations are $-2.8 \times 10^{15} \text{ cm}^{-3}$ for sample QD700, $-2.5 \times 10^{15} \text{ cm}^{-3}$ for QD630 and $-2.9 \times 10^{15} \text{ cm}^{-3}$ for QD-s-700. Therefore, these samples are $p^+ - n - n^+$ junctions.

However, in both cases of solar cells, the active regions have a doping level three orders of magnitude lower than the p and n -sides, so we can consider the cells as ideal p - i - n junctions with an intrinsic middle region. The depletion region of an ideal p - i - n junction occupies completely the intrinsic region in the absence of bias voltage. At high reverse bias, the depletion crosses the

interfaces p/i and i/n and extends short distances x_p and x_n inside the p and n -sides, respectively.

The DLTS technique has been specifically developed for Schottky diodes and no papers have offered any detailed physical description of DLTS applied to $p-i-n$ junctions. However, the technique is widely used in this type of junctions. The energy band diagram for a $p-i-n$ junction is similar to the ones shown in figure 3.1 for zero and reverse bias, exchanging the metal side by p -type material and putting the n -type at the right side of the depletion. Therefore, carrier injection and carrier emission processes are expected to occur over the depletion region in a similar manner as for the Schottky diodes. The same theory described for DLTS in section 3.1 and equations 3-2, 3-5 and 3-6 are also applied to the case of $p-i-n$ junctions.

We also have considered the same basic DLTS theory and we have applied Laplace DLTS to all our samples without distinction. Moreover, a slightly modified version of equation 3-5 has been used in the case of the solar cells, as it will shown in the next chapter of results. The traps that can be detected by DLTS in $p-i-n$ junctions are the ones localized throughout the depletion region, therefore, traps within the x_p and x_n distances are also detected at high reverse bias. In this work, we have avoided the depletion region to spread into the p and n -sides by using reverse voltages lower than 6 V in order to detect solely the traps over the active region of the solar cells.

Finally, we will describe the sample processing that has been made according to the type of sample. All the samples were processed into mesa-type devices using photolithography and wet chemical etching methods. The C-doped and Si-doped GaAs samples (p570, p630, n570 and n630) were converted into Schottky diodes by evaporation of Ti/Au (10 nm/ 160 nm) over GaAs mesas and Ge/Au/Ni/Au (30 nm/45 nm/30 nm/1.50 nm) over the n -type substrate, as seen in figure 3.7. The IB solar cells and solar cells without QDs (SC630, SC700, SCycle, QD630, QD700 and QD-s-700) are $p-i-n$ junctions and have intrinsic regions, so they only need ohmic contacts of Au/Zn/Au (15 nm/30 nm/130 nm) on the p top side of mesas and Ge/Au/Ni/Au (30 nm/45 nm/30 nm/1.50 nm) on the n -type substrate. Once processed, the devices were mounted on sample holders with ohmic contact pins linked to the top of mesas and one pin linked to the substrate.

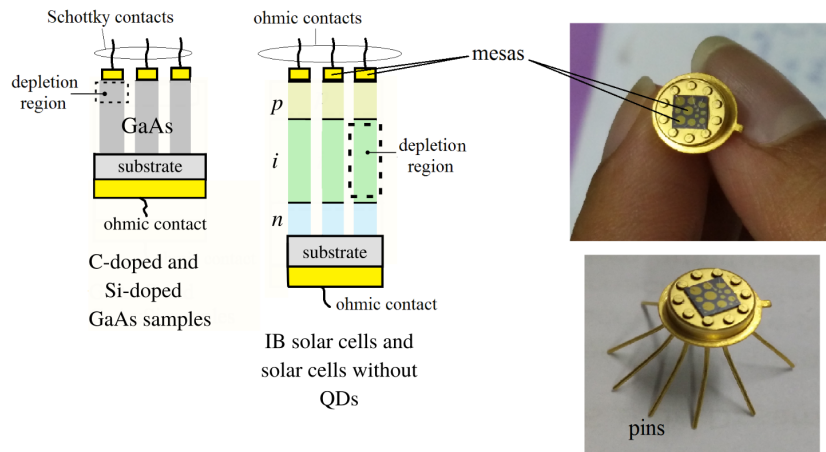


Figure 3.7: Scheme of the samples processed into devices for DLTS and Laplace measurements. The images show the final device. The pins connect the device to the instruments.

3.5 Photoluminescence - (PL)

This technique is broadly used to qualitatively detect impurities and defects in semiconductors. Also, confined energy levels of quantum structures in semiconductor devices (for example, quantum wells and quantum dots) can be determined. In photoluminescence, a semiconductor material is illuminated with a continuous wave laser beam of fixed wavelength and the absorbed photons in the material induce the creation of electron-hole pairs (e-h) that later recombine to return to the minimal energy condition. The recombination process of an e-h pair is followed by an emission of a photon in order to release the energy excess. Therefore, the whole material radiates polychromatic light comprised of the different photon energies that characterize the recombinations band-to-band and recombinations through impurities, defects and quantum structures energy levels. Measurements of photoluminescence at low temperature are appropriate to avoid the decrease of intensity of emissions due to non-radiative recombinations activated by thermal excitation. It is clear that non-radiative recombinations are not detected by photoluminescence.

Figure 3.8 shows a scheme of the experimental arrangement used for photoluminescence measurements. The sample is mounted in a cryostat which is temperature controlled. A Nd:YAG laser with light emission at 532 nm is used to illuminate the sample. This light is chopped to impose a fixed phase that serves as reference. The resultant luminescence is focused into a monochromator to be decomposed in a spectrum as a function of the wavelength. A germanium detector is located at the exit of the monochromator, allowing the detection of luminescence intensity per photon energy. An integrated lock-in

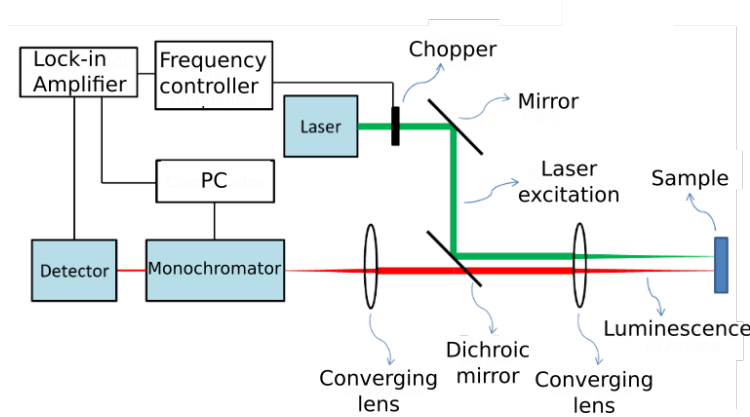


Figure 3.8: Scheme of the experimental arrangement for PL measurements. The incident laser and the emitted light from the sample follow the green and red paths, respectively.

measures and amplifies the response of the detector using the reference phase and exports a final voltage signal proportional to the light intensities. For this work, we have used two cryostats to measure at two different ranges of temperatures, one for [20–100] K, and another for [100–290] K. This was necessary to study the temperature dependence of emission intensities.

In the next subsection, it will be showed a review of the most typical recombination processes resulting from optical excitation of semiconductors.

3.5.1 Radiative recombinations observed in PL spectrum

Figure 3.9 shows an energy band diagram with some of the most common types of radiative recombination observed in PL. Among these recombinations, the most simple form is the band-to-band recombination that corresponds to an electron from conduction band recombining with a hole in the valence band. The energy of the subsequent photon emission corresponds to the energy gap of the semiconductor material, which depends on temperature and generally follows the Varshni formula:

$$E_g(T) = E_g(T = 0 \text{ K}) - \frac{aT^2}{T + b} \quad (3-11)$$

where a and b are material specific constants. $E_g(T = 0 \text{ K})$ is approximately 1.52 eV for GaAs. The band-to-band recombination PL peak dominates at room temperature and its intensity decreases at lower temperatures because of the increase of non-radiative recombinations.

In a case of an extremely pure GaAs, besides the band-to-band recombination, free exciton recombination can be also observed. A free exciton is an e-h pair for which the electron remains bound to the hole by a Coulom-

bic attractive force. The e-h pair moves together through the semiconductor as a free quasi-particle. When the electron recombines with the hole (exciton decay) a photon is created with an energy slightly lower than the energy gap.

Radiative recombinations involving shallow impurities are usually observed in PL spectra. These are the donor-valence band (D^0, h) and conduction band-acceptor (A^0, e) recombinations, donor-acceptor ($D - A$) pair recombination and bound exciton decay. Emissions derived from these recombinations serve to detect and identify shallow impurities. (D^0, h), (A^0, e) and ($D - A$) recombinations are also schematized in figure 3.9.

(D^0, h) and (A^0, e) recombinations involve donors and acceptors with energy levels close to the band edges (energy difference < 100 meV). (D^0, h) recombination occurs when an electron in a neutral donor recombines with a hole in the valence band. Similarly, (A^0, e) recombination occurs when an electron in the conduction band recombines with a hole in a neutral acceptor. The donor-acceptor ($D - A$) recombination is the recombination process between an electron in a neutral donor and a hole in a neutral acceptor. The last three types of recombination are highly probable at very low temperature when the most shallow impurities are neutral. As the temperature increases, donors and acceptors are ionized and the corresponding PL peaks are quenched. Donors become completely ionized before acceptors since donors have lower ionization energies and then need less thermal excitation to be ionized.

The emission peak energies of (D^0, h) and (A^0, e) recombinations are close to the difference between the energy gap and the ionization energy (E_D or E_A) of the involved shallow impurity:

$$\hbar\omega \approx E_g - E_D \quad \text{for } (D^0, h) \quad (3-12)$$

$$\hbar\omega \approx E_g - E_A \quad \text{for } (A^0, e) \quad (3-13)$$

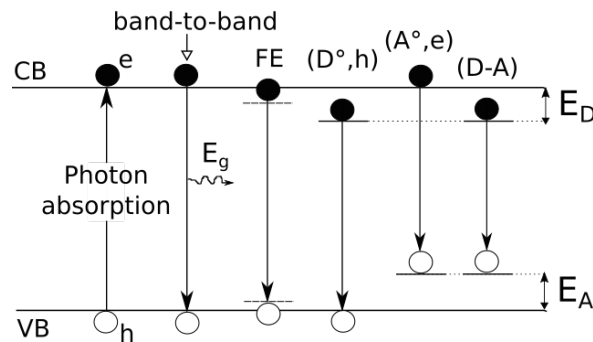


Figure 3.9: Most typical radiative recombinations in semiconductors obtained by optical excitation during photoluminescence measurements. These recombinations are described in the text.

In the case of $(D - A)$ recombinations, the energy position is modified by the Coulombic interaction of the donor-acceptor pair:

$$\hbar\omega = E_g - (E_A + E_D) + \frac{e^2}{K\varepsilon_0 r} \quad (3-14)$$

where r is the separation between the donor and acceptor and K and ε_0 are the dielectric constant of material and the vacuum permittivity, respectively. Usually, to distinguish PL peaks of $(D - A)$ recombinations, the sample is submitted to variations of laser power in order to change the probability of luminescence of $(D - A)$ pairs with different separation lengths. This occurs in the following way: the number of $(D - A)$ pairs with shorter separation lengths recombining and emitting photons are higher than the number of pairs with larger separation lengths, so when the optical excitation increases and a higher number of photons reach the material, the number of closer $(D - A)$ pairs recombining increases against the almost constant number of more distant pairs. This is frequently called as “saturation of distant pairs”. As a result, $(D - A)$ recombination peak moves to higher energies and its bandwidth becomes narrower for higher laser powers in accordance to above equation for low r values.

Now, we will mention the bound excitons. A bound exciton is formed when a free exciton is trapped by an impurity or even by a defect. Similarly to free excitons, the decay of the bound exciton yields a photon. In the case of excitons bound to impurities, there are four types of bound excitons: excitons bound to ionized donors (D^+, X), excitons bound to neutral donors (D^0, X), excitons bound to ionized acceptors (A^-, X) and excitons bound to neutral acceptors (A^0, X). The physics behind the binding of bound excitons is a complex concept that will not be detailed here. We are only interested in monitoring the presence of impurities through bound excitons decay. A simple way to confirm PL peaks of bound excitons in GaAs samples and estimate the ionization energy of the involved impurity is using the next expressions of reference (29) to predict the corresponding energy positions at very low temperature (around 2 K):

$$\hbar\omega(D^+, X) = E_g - 1.06E_D \quad (3-15)$$

$$\hbar\omega(A^-, X) = E_g - 1.4E_A \quad (3-16)$$

$$\hbar\omega(D^0, X) = E_g - E_X - 0.13E_D \quad (3-17)$$

$$\hbar\omega(A^0, X) = E_g - E_X - 0.07E_A \quad (3-18)$$

where E_D and E_A are the ionization energies of the donor and acceptor linked to the excitons, respectively, and E_X is the free exciton binding energy of about

4.1 meV (30). Usually, the PL peaks of bound excitons in GaAs are centered very close to the band-to-band recombination peak and sometimes they can not be separated into two different peaks. The higher the ionization energy of the shallow impurity, the larger the peak energy separation.

In the special case of samples QD630, QD700 and QD-s-700 with quantum dot structures, the PL spectrum exhibit additional peaks corresponding to radiative recombinations between holes and electrons confined in the dots. A scheme of these type of recombinations is illustrated in figure 3.10. The emission energies of these recombinations are characteristic of the confined energy levels for holes and electrons in the QDs, which strongly depend on the growth conditions. Parameters as growth temperature and layer width define the size and the distribution of the dots, and thus the number of confined energy levels. In QDs, the recombination yields a photon emission with energy equal to the difference between the confined energy levels, as schematized in the figure. E1-H1 and E2-H2 correspond to recombinations of holes and electrons located in the ground and the first excited states, respectively. According to the rules of coupling of wavefunctions representing the energy states of the confined energy levels, only recombinations of holes and electrons located in levels with the same order of excitation are allowed.

Finally, we will discuss the case of recombinations through deeper level impurities. These recombinations derive in photon emissions of energy lower than the energy of emissions produced by recombinations through shallow impurities. Gallium, Arsenic and impurity atoms located in antisites and interstitials of GaAs materials, and even defect complexes, can act as radiative recombination centers. For example, the Gallium antisite Ga_{As} is considered as a deep acceptor and has been reported to give rise to a low-temperature PL peak centered at 1.46 eV (31), which is lower than the emission of 1.52 eV of the band-to-band recombination.² On the other hand, some defect complexes have been detected by photoluminescence. For example, the complex $Si_{As} - V_{As}$, resulting from the Coulombic attraction between a Si_{As} acceptor and a vacancy of Arsenic V_{As} , has been associated with an emission at 1.37 eV (31). Also, the complex $Si_{Ga} - V_{Ga}$, resulting from the Coulombic attraction between a silicon shallow donor Si_{Ga} (a silicon atom in a Gallium site, derived from silicon doping) and a Gallium vacancy V_{Ga} , is associated with emissions of 1.18 eV (32), 1.24 eV (33) and 1.23 eV (31).

The above complexes cannot be represented by energy levels within the gap, as in the case of acceptors and donors, because the corresponding photon

²the corresponding energy levels are at 60 meV and [80-90] meV above the valence band edge, respectively. In contrast, shallow impurities typically have levels below 100 meV with respect to the conduction or the valence band edge.

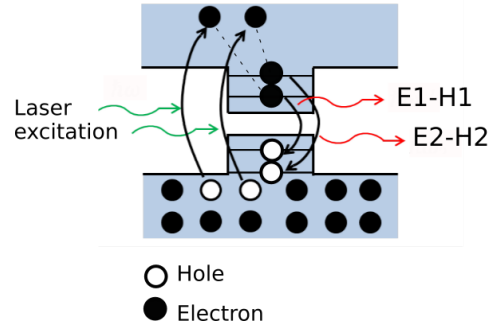


Figure 3.10: Radiative recombinations in a quantum dot. The emission energies correspond to the difference between the hole and electron confined levels.

emissions derive from internal transitions. However, the Photoluminescence is able to detect these defects of complex behavior in a simple way, which renders this technique very attractive for the study of defects.

3.5.2

Methods of analysis

In accordance to the characteristics described in the last section, the radiative recombinations depend strongly on temperature. The impurities become ionized as the temperature increases, while the non-radiative recombinations and phonons are activated. In consequence, the PL peaks experience a thermal quenching, it means, the emission peaks gradually diminish. The next well-known expression [(34), (35)] qualitatively describes this process:

$$I = \frac{I_0}{\left(1 + A \exp\left(\frac{-E_a}{k_B T}\right)\right)} \quad (3-19)$$

where I_0 is the intensity at $T=0$ K, A is a constant independent of temperature, and E_a is the activation energy. In the case of (D^0, h) and (A^0, e) recombinations, E_a is equal to the ionization energy of the shallow impurity. In general, E_a represents the thermal energy necessary to deactivate the recombination process and is characteristic of the type of recombination.

In this work, we have measured the PL spectra of our samples as a function of temperature in order to calculate the thermal activation energies related to the emission peaks and so determine the type of impurities and defects present in the samples. The temperature was varied from 20 K up to 290 K while keeping constant the incident excitation power at 50 mW. The peak activation energy was determined from the slope of the curve $\ln(\text{PL Intensity})$ Vs. $1/T$, in accordance with the linear form of equation 3-19 for high temperatures:

$$\text{For } A \gg 1 \text{ and } K_B T \geq E_a, \quad (3-20)$$

$$\ln(I) \cong \ln\left(\frac{I_0}{A}\right) - \frac{E_a}{K_B T}$$

The type of PL emissions were determined based on the resulting activation energies and the relations described by equations 3-11 to 3-18. The full width at a half maximum (FWHM) of some peaks was calculated to determine the behavior of the linewidth with increasing temperature.

Emissions related to $(D - A)$ recombinations were verified through a second series of PL measurements as a function of the incident laser power, from 0.7 mW up to 250 mW at 20K, searching for peak shift to higher energies. Besides the $(D - A)$ recombinations, this second series of measurements were also used to recognize other types of emissions, based on the results found by Schmidt and Lischka (36), which state the following relations between the PL peak intensity and the laser power (L):

$$I \sim L^k \quad (3-21)$$

$$1 \leq k < 2 \quad \text{for emissions type (I)}$$

$$k < 1 \quad \text{for emissions type (II)}$$

where emissions type (I) include the band-to-band, free exciton, (A^-, X) and (D^+, X) emissions, and emissions type (II) include (D^0, h) , (A^0, e) and $(D - A)$ emissions. The above relations were established for a maximum variation of power of two orders of magnitude, and describe the increase of the PL peak intensity as a function of the excitation power according to the type of emission.

For emissions type (I), the intensity of emission can increase linearly ($K \approx 1$) or quadratically ($K \approx 2$) with the increase of excitation power, i.e., with the increase in incident photons. This is because each e-h pair involved in these types of recombinations is created by the absorption of one ($K \approx 1$) or two incident photons ($K \approx 2$) (one photon to create the electron and one more photon to create the hole).

The case of emissions type (II) is different since they are dominated by shallow impurities. The number of donors and acceptors impurities in an extrinsic semiconductor is finite, so these numbers limit the recombination rates of emissions type (II). Furthermore, the donors and acceptors can be ionized by thermal excitation, impacting the number of available neutral impurities for recombination. Therefore, the intensity increases at a lower rate than the excitation power ($K < 1$).

All the details presented in this section will be useful to understand the analysis presented in the chapter of Photoluminescence results, chapter 5. The DLTS and Laplace DLTS results will be presented before in the next chapter 4 in order to present all the results in an understandable form.

4 DLTS and Laplace DLTS results

In this chapter, the results obtained from the DLTS and Laplace DLTS studies on the IB solar cells (samples QD630, QD700, and QD-s-700), solar cells without QDs (samples SC630, SC700, and SCycle) and individually doped GaAs samples (p570, p630, n570, and n630) are presented. The results are shown in two sections: the first section presents the electrical characterization of the samples, and the second one focus on the DLTS and Laplace DLTS measurements and the identification of the detected traps. The third section presents the analysis of the traps and their probable influence on the energy conversion efficiency of the solar cells.

4.1 Electrical characterization

The samples were electrically characterized by Capacitance-Voltage measurements at 300 K before DLTS and Laplace DLTS measurements. The characterization was necessary to choose suitable reverse voltages for the bias pulse of those techniques. Also, the carrier concentrations of the individually doped GaAs samples and active regions of the solar cells were determined from capacitance measurements.

Figure 4.1 shows the depletion region width of the solar cells as a function of the reverse bias voltage which was determined from capacitance-voltage measurements. The depletion width is easily calculated from the capacitance,

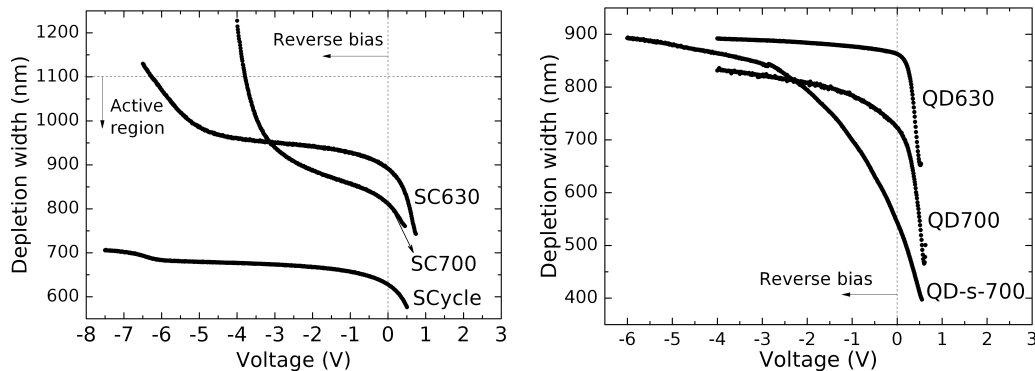


Figure 4.1: Width of the depletion region of the solar cells without QDs (left) and the IB solar cells (right) as a function of the reverse bias voltage.

C, as $W = A\varepsilon/C$, where A is the contact path area of the cell and ε is the GaAs permittivity. As the purpose of the DLTS measurements on the solar cells is to determine the traps over the active regions, the depletion region should not exceed the active regions. This is true when applied voltages below -3.8 V and -6.2 V to samples SC700 and SC630, respectively, as seen in the figure. Sample SCycle has a thinner depletion that does not reach the active region edge for the measured voltage range. For samples SC630 and SC700, a slope change is observed for increasing reverse voltage. This is a consequence of depletion spreading into the *p* and/or *n*-sides. The depletion regions of samples QD630 and QD700 are shorter than the active region thickness for reverse voltage lower than -4 V, or -6 V in the case of sample QD-s-700.

Based on the above results, the reverse voltages for DLTS measurements have been fixed as follows:

- $V_r = -2.5$ V, -2 V and -3 V for SC630, SC700 and SCycle, respectively
- $V_r = -0.25$ V, -0.5 V, -1 V, -3 V and -4 V for QD630.
- $V_r = -0.25$ V, -0.5 V, -1 V, -2 V, -3 V and -4 V for QD700.
- $V_r = -1$ V, -4 V and -6 V for QD-s-700.

The individually doped GaAs samples were measured by DLTS only at -1 V yielding depletion regions of about 182 nm, 325 nm, 457 nm and 193 nm for samples p570, p630, n570 and n630, respectively (see the top plots of figure 4.2). The nominal carrier concentrations of the individually doped GaAs samples were confirmed by plotting $1/C^2$ as a function of reverse voltage. The concentration N_d is extracted from the slope according to the next relation:

$$\frac{1}{C^2} = \left(\frac{2}{A^2 \varepsilon \varepsilon_0 N_d} \right) (V_{bi} - V_r) \quad (4-1)$$

where V_{bi} is the built-in voltage of the Schottky diode. The above equation stated for Schottky diodes can be found in many semiconductor books [(37), (38)]. Bottom plots of figure 4.2 show the $1/C^2$ plots for the individually doped GaAs samples and the corresponding N_d concentrations. These values are similar to the nominal concentrations which are $1.1 \times 10^{17} \text{ cm}^{-3}$ (sample p570), $2.4 \times 10^{16} \text{ cm}^{-3}$ (p630), $6.5 \times 10^{16} \text{ cm}^{-3}$ (n570) and $1.1 \times 10^{17} \text{ cm}^{-3}$ (n630). The linear behaviour of plots of samples p630 and n630 between 0 V and -4 V indicates uniform concentrations, in good agreement with equation 4-1. In fact, the monitored distances up to -4 V of about 575 nm and 300 nm, respectively, are within the GaAs layers of both samples, which have thicknesses of 1000 nm (see plots of depletion width). It means, the doping concentrations of samples p630 and n630 are uniform along 575 nm and 300 nm within the GaAs layers from the metal/semiconductor interface, respectively. Samples p570 and n570

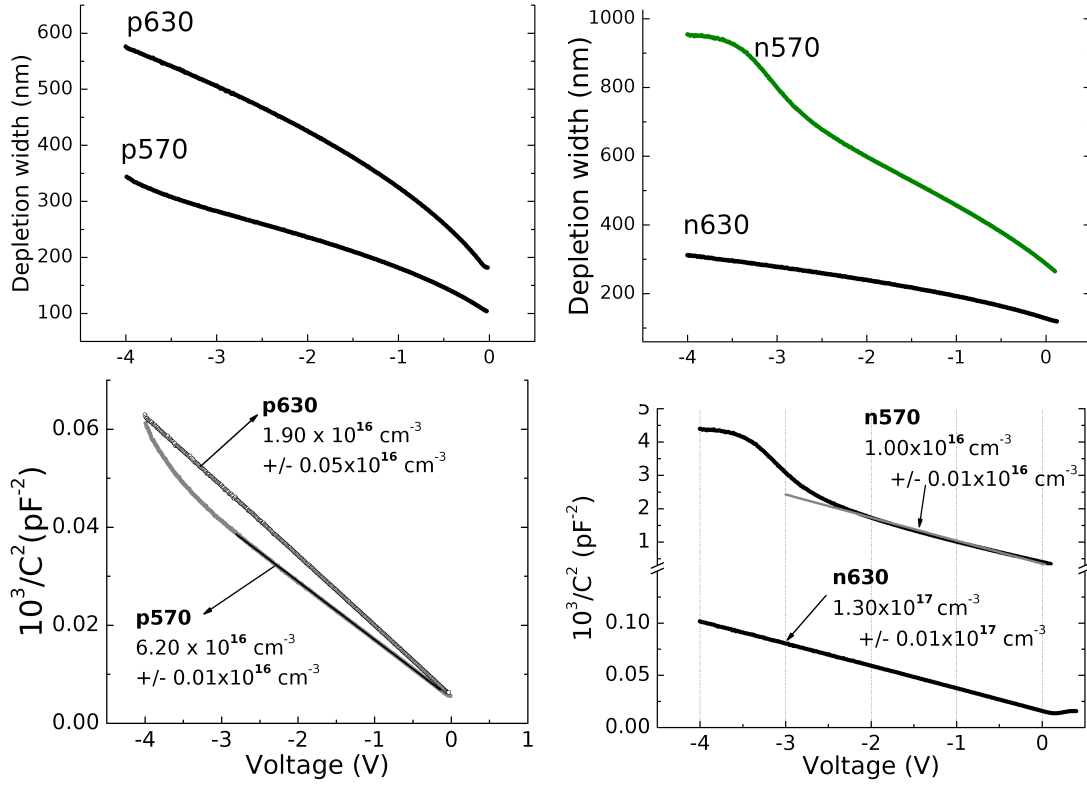


Figure 4.2: Top: Depletion region width of the *p*-doped GaAs samples (left) and *n*-doped samples (right), with origin at metal/semiconductor interface. Bottom: Determination of carrier concentrations of the *p*-doped GaAs samples (left) and *n*-doped samples (right) from $1/C^2$ plots.

exhibit uniform concentrations along the GaAs layers width, which are 271 nm and 600 nm, respectively and correspond to measurements above -2.5 V and -3 V, respectively. The slope changes of $1/C^2$ plots seen for these last two samples below -3 V and -2.5 V, therefore, are due to the depletion width exceeding the GaAs layer thickness and extending into the highly doped substrate.

The concentrations of the traps found in the individually doped GaAs samples were determined based on the N_d concentrations, using equations 3-5, 3-6 and 3-7. To calculate the length λ in the case of the *p*-doped GaAs samples, $E_F - E_T$ was replaced by $E_T - E_F$ because the Fermi level lies next to the valence band edge, below the trap deep levels E_T . The trap concentrations will be shown later during the discussion of DLTS results.

Figure 4.3 shows the $1/C^2$ plots of the solar cells. In the case of *p-i-n* junctions, equation 4-1 takes the form of (39):

$$\frac{1}{C^2} = \left(\frac{2}{A^2 \epsilon e} \right) \left(\frac{N_p + N_n}{N_p N_n} \right) (V_{bi} - V_r) + \frac{d^2}{A^2 \epsilon^2} \quad (4-2)$$

where d is the intrinsic region width and N_p and N_n are the carrier concentrations on the *p* and *n*-sides, respectively.

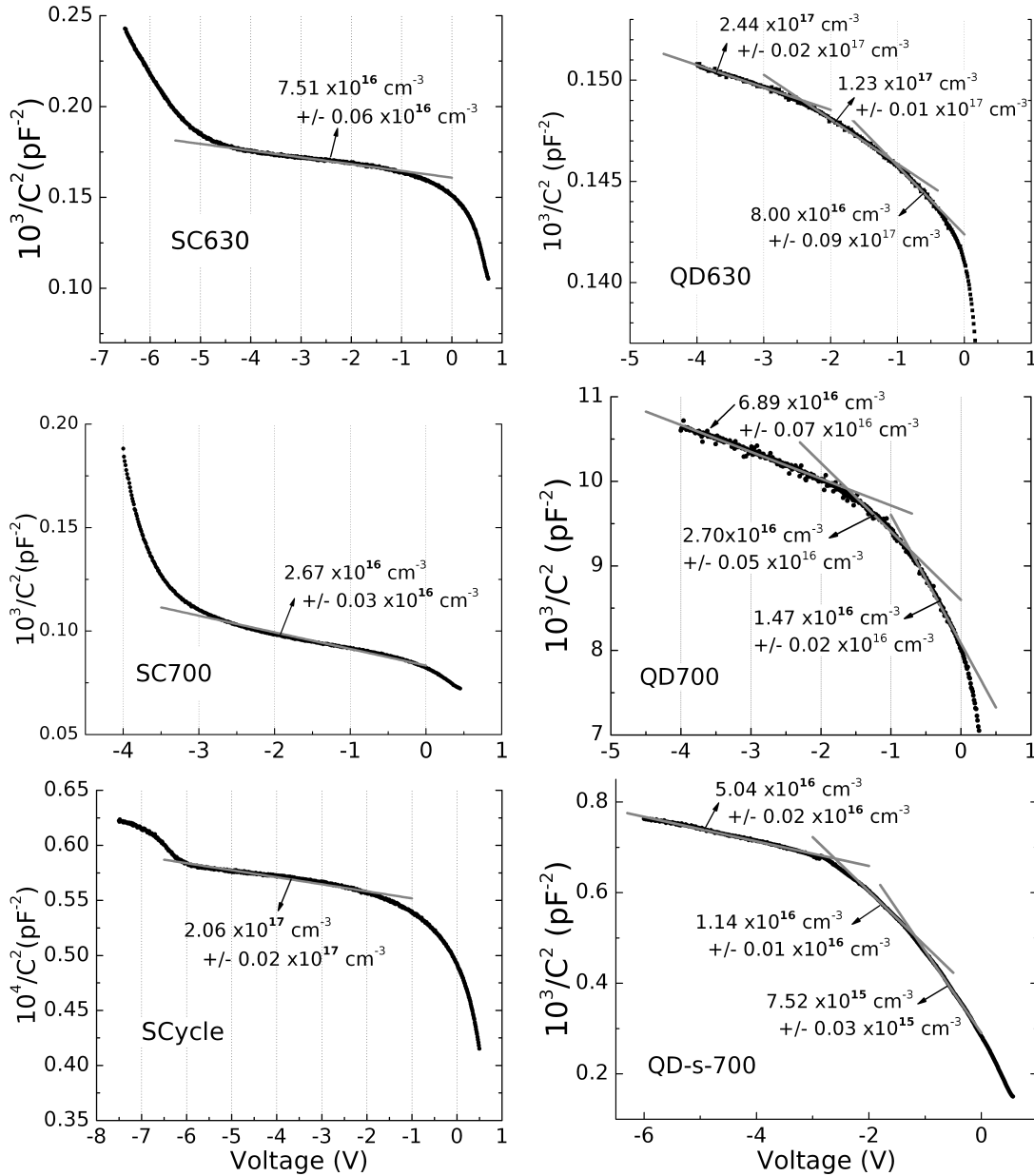


Figure 4.3: $1/C^2$ plots and effective carrier concentrations of the solar cells depending on the reverse voltage, calculated from the slope of the plots. (left) Solar cells without QDs, and (right) IB solar cells.

In the above equation, we must consider an important question: the equation does not involve the carrier concentration N_d over the depletion region, as in the case of Schottky diodes (equation 4-1). Instead, the equation involves an "effective" carrier concentration equal to $\frac{N_p N_n}{N_p + N_n}$, which I will call N_{eff} from now on. Effective carrier concentrations have been calculated for all the six solar cells along the reverse voltage range of capacitance measurements, in a similar way as for the individually doped GaAs samples. These concentrations are shown on the $1/C^2$ plots of figure 4.3. As observed, the plots of the IB solar cells exhibit three reverse voltage ranges with different

effective concentrations. This may be due to the depletion width gradually increasing with the increase of the reverse voltage which sequentially include more QD InAs layers. The effective doping concentrations of the IB solar cells, therefore, increase with the reverse voltage. On the other hand, the $1/C^2$ plots of the solar cells without QDs exhibit uniform effective concentrations within the reverse voltage range of DLTS measurements (between -3 V and -2 V), since these cells have no QDs.

The calculated effective concentrations N_{eff} have been used to calculate the concentrations of the traps found in the six solar cells. For this purpose, the term N_d has been replaced for $N_{eff}(V_r)$ in equations 3-5 and 3-6, as it has also been done in reference (40). The depletion width at reverse voltage $W(V_r)$ and at zero bias $W(0)$ were taken from the plots of 4.1. The Fermi level E_F in equation 3-6 has also been calculated based on the effective concentrations $N_{eff}(V_r)$. The difference $E_F - E_T$ was replaced by $E_T - E_F$ for the solar cells without QDs with p -type active regions. The trap concentrations will be shown in the section of discussion of DLTS results.

The plots $1/C^2$ do not offer information about the type of net charge, n or p -type, over the active regions. For this reason, it will be considered the same net charges discussed in section 3.4. The active regions of the solar cells without QDs are considered p -type since their nominal doping concentration are based on p -type measurements. The active regions of the IB solar cells are considered n -type in agreement to the n -type net concentrations calculated with equation 3-10. Despite the fact that the carrier concentrations of the active regions of the six solar cell are higher than those initially considered in section 3.4, the solar cells remain being $p^+ - p - n^+$ and $p^+ - n - n^+$ junctions. All the considerations made for these type of junctions are still valid.

4.2 DLTS and Laplace DLTS results

The DLTS spectra of all the samples and the corresponding Arrhenius plots resulting from Laplace DLTS measurements are presented in this section. The raw Laplace DLTS data, i.e., the emission rate spectra, are shown in appendix A in the form of colorplots. The samples were measured and analyzed using the DLTS technique, Laplace DLTS technique and methods described in sections 3.1, 3.2 and 3.4. The DLTS peaks were fitted by Gaussian curves in order to estimate the peak heights and to determine the concentrations of the traps.

Figures 4.4.(a) to (f) correspond to the DLTS spectra and the Arrhenius plots of the individually doped GaAs samples and the solar cells without QDs,

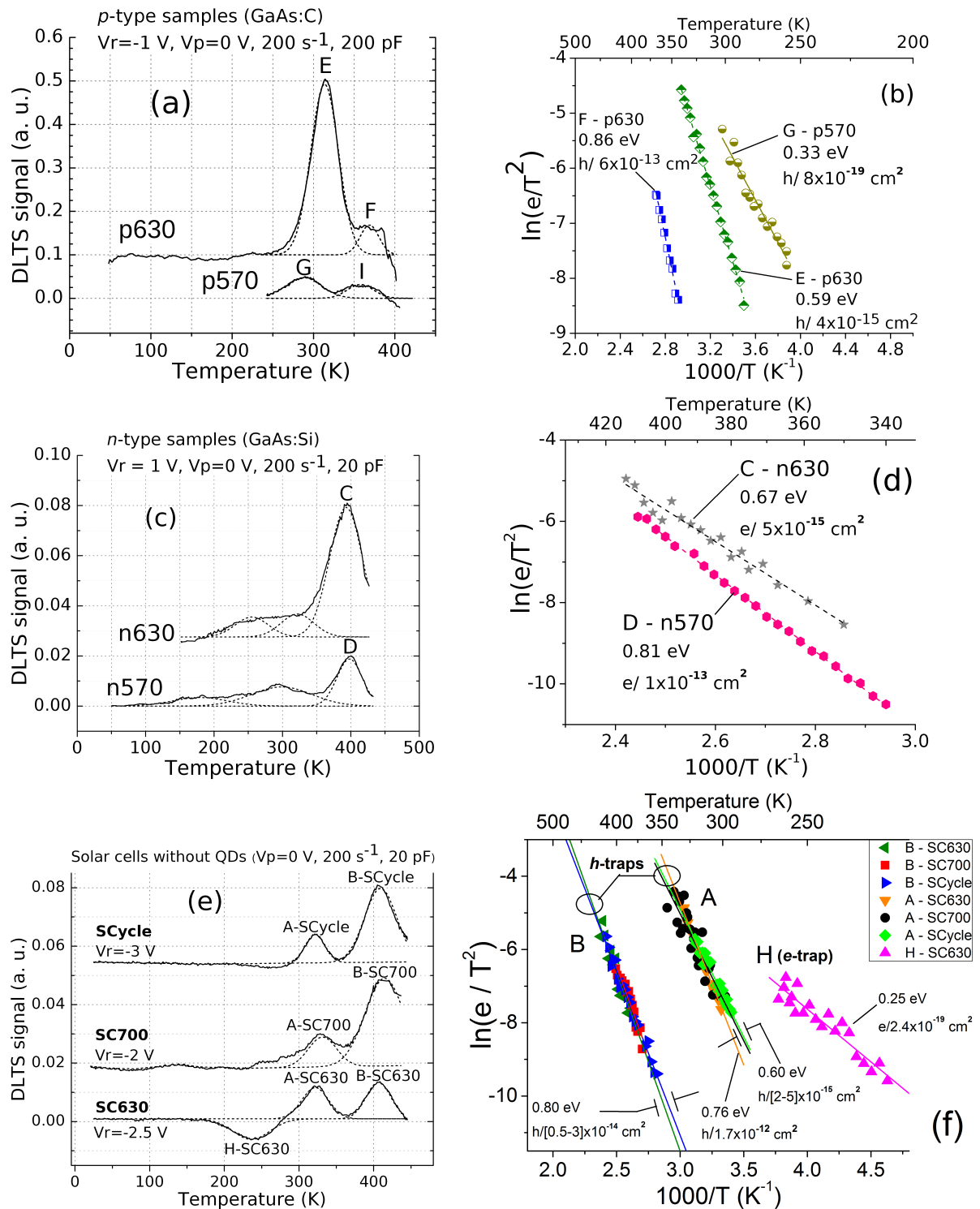


Figure 4.4: DLTS spectra (left) and corresponding Arrhenius plots (right) of the *p*-type doped samples ((a) and (b)), the *n*-type doped samples ((c) and (d)) and the solar cells without QDs ((e) and (f)). The voltage of carrier injection V_p and the reverse voltages V_r applied for the DLTS scans are detailed on the plots. The trap signatures are shown on the Arrhenius plots.

as detailed in the figure description. The thermal activation energies and the capture cross-section of the detected traps are exhibited on the Arrhenius plots. From here on, these two parameters will be called trap signatures and they will be used to identify the respective type of trap.

Several traps are observed in the DLTS spectra, but only those included in the Arrhenius plots have been clearly identified in the emission rate spectra. The rest of the traps have been ruled out and will not be analyzed in this work.

As observed from figure 4.4.(e), a similar pair of peaks, labeled A and B, appear in the DLTS spectra of the solar cells without QDs around the same temperature ranges. The Arrhenius lines ascribed to peaks B (B-S630, B-SC700, and B-Scycle) match each other and exhibit very similar trap signatures, as seen in figure 4.4.(f). Therefore, they are attributed to the same type of defect. The same occurs with the Arrhenius lines ascribed to peaks A of cells SC700 and SCycle, showing that they correspond to a second type of defect. However, the Arrhenius line of peak A of sample SC630 exhibits a small change in both the slope and the y -intersection, in comparison to the two other Arrhenius lines of A-SC700 and A-SCycle. Since the activation energies and the capture cross-sections are determined from the slope and the y -intersection of the Arrhenius lines according to equation 3-9, any change of these parameters induces a change in the trap signatures. For this reason, trap A-SC630 exhibits higher activation energy and higher capture cross-section.

A possible explanation for the change in the characteristics of trap A-SC630 is the presence of trap H-SC630, which is only observed in sample SC630. The DLTS and Laplace DLTS measurements do not offer any information that explains how one trap can alter the characteristics of the other trap. Despite this, we think the three peaks A correspond to the same type of defect since their temperature ranges coincide, and since their respective Arrhenius lines are similar in position and orientation.

The DLTS spectra and Arrhenius plots of the IB solar cells are shown in figures 4.5, 4.6, and 4.7. The label of the traps of these cells includes a reference of the cell (600 for cell QD630, 700 for cell QD700, and QD-s for cell QD-s-700), and the reverse voltage at which they are measured.

A high number of traps have been measured in the DLTS spectrum of cell QD630, but only those with higher DLTS signals could be clearly identified by Laplace DLTS. A very interesting fact is that, for this n -type active region, minority carrier (hole) traps have also been measured by DLTS in the form of negative peaks at -0.25 V and -0.5 V. This result was not expected since reverse bias pulses were applied to the cell to inject majority carriers (electrons) into the traps.

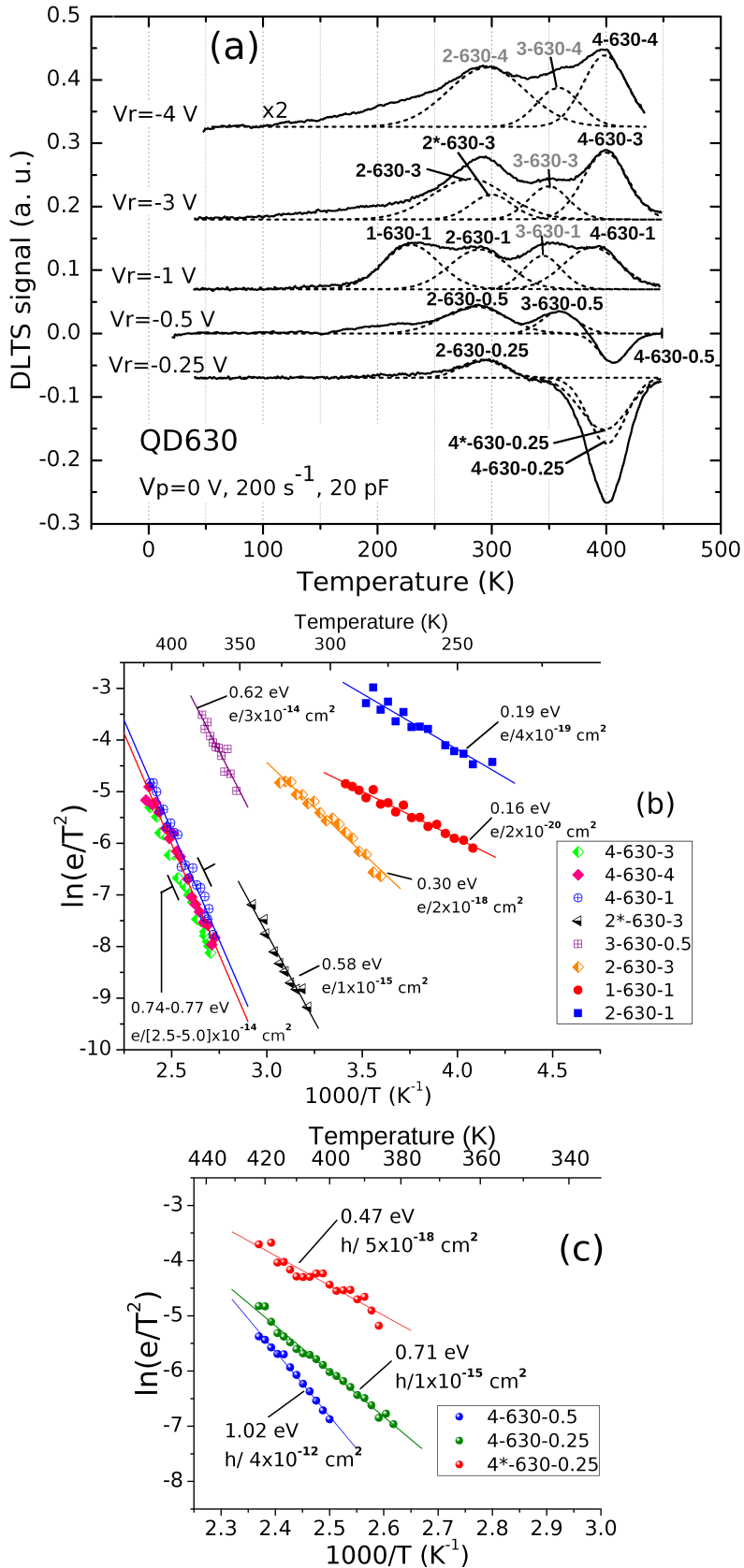


Figure 4.5: (a) DLTS spectra and (b),(c) Arrhenius plots of solar cell QD630. The electron traps (majority carriers) are shown in figure (b) and the hole traps are shown in figure (c). The trap signatures are shown on the Arrhenius plots.

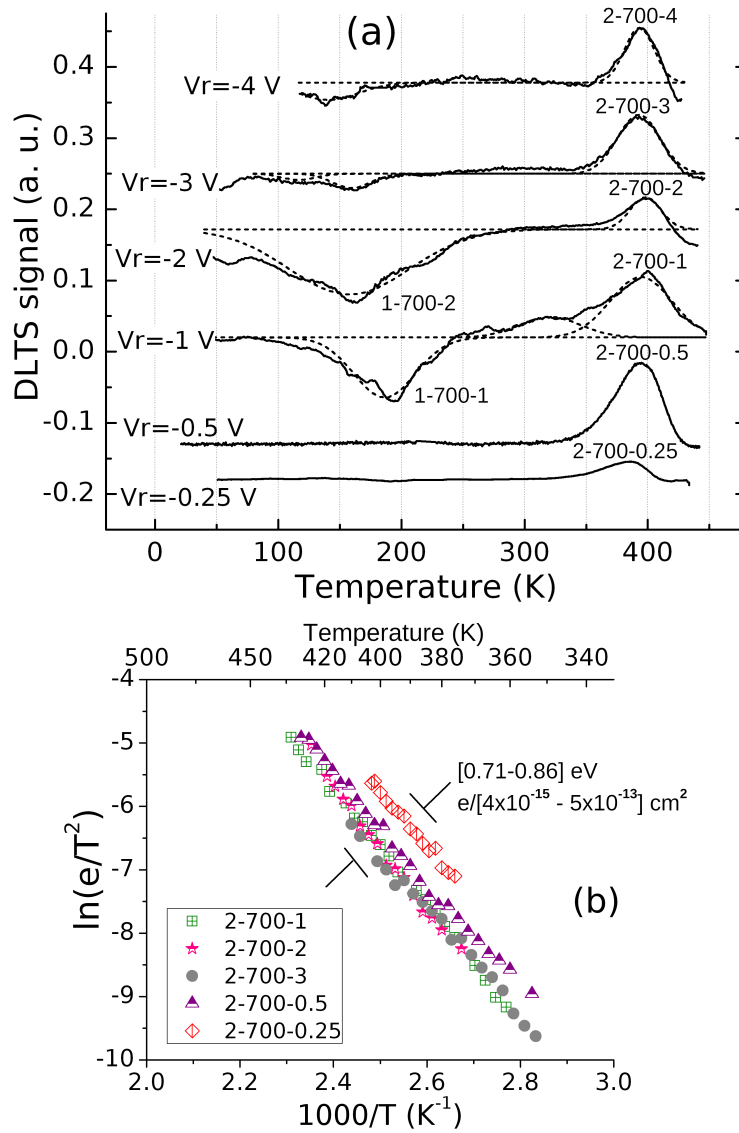


Figure 4.6: (a) DLTS spectra and (b) corresponding Arrhenius plots of solar cell QD700. Only the traps with DLTS peaks centered around 400 K have been detected by Laplace DLTS.

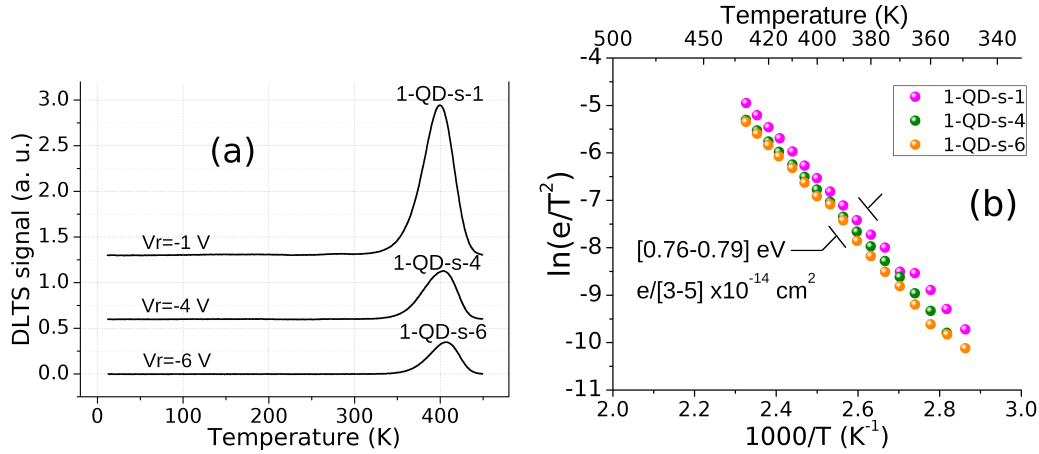


Figure 4.7: (a) DLTS spectra and (b) corresponding Arrhenius plots of solar cell QD-s-700. The three DLTS peaks seen at -1 V, -4 V and -6 V correspond to the same defect EL2.

In this way, the majority carrier traps are detected, according to the theory. However, a flux of minority carriers must have been injected into the cell when the pulses from -0.25 V and -0.5 V to 0 V are applied, so as to induce the detection of the hole traps. We assume that the minority carrier injection has been possible due to the highly doped p -side of the cell. Figure 4.8.(a) was drawn to explain this assumption in terms of the energy band scheme. The energy barrier seen by the holes in the p side (indicated in the figure) usually avoids that the holes reach the depletion during the carrier injection step at 0 V. But due to the high thermal excitation at 400 K (temperature at which the hole traps are detected), and the high hole concentration on the p -side, probably a significant amount of holes cross the barrier and reach the depletion. The distance covered by the holes from the p -side/active region interface must be short, so that they could be trapped by hole traps localized close to the interface. Once the reverse voltage is restored, the holes are emitted to the valence band and constitute a current of enough intensity to be detected. At higher reverse voltage ($V_r < -1$ V), this current is negligible in comparison to the current of electrons emitted by electron traps 4-630-1, 4-630-3, and 4-630-4 and, hence, only these electron traps are detected.

Cell SC630 also exhibits a minority carrier trap, the electron trap H (see figures 4.4.(e) and (f)). For this cell, we assume an analogous case of minority carrier injection at 0 V. But, instead of a flux of holes, a large flux of electrons is injected from the highly doped n -side, being captured by centers of trap H localized close to the active region/ n -side interface, as schematized in figure 4.8.(b). The temperature of detection of trap H (about 250 K) should be enough to induce the electron emission from the traps to the conduction band when the reverse voltage is restored. Hence, an electron current is yielded

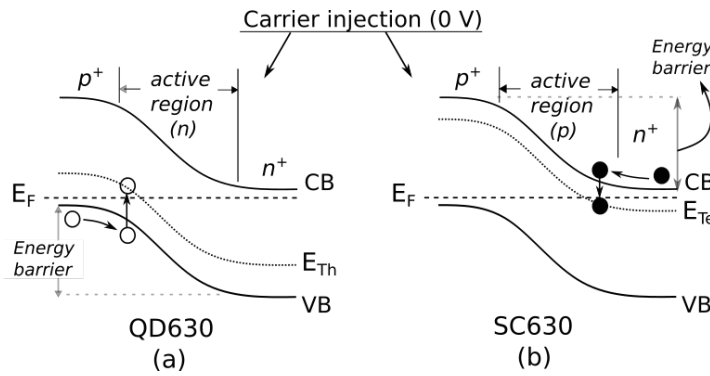


Figure 4.8: A possible scheme of minority injection in cells QD630 and SC630 that leads to the detection of minority carrier traps by DLTS (negative DLTS peaks). E_{Th} and E_{Te} are the energy levels of a hole trap and an electron trap, respectively. Holes are represented by circles and electrons are represented by black dots.

and measured as the DLTS signal of the trap. Obviously, the temperature of detection of trap H is lower than the ones of traps A and B since trap H is a shallower trap (evidenced by its lower activation energy) and, hence, it needs less thermal excitation to emit.

Turning our attention to cells QD700 and QD-s-700, a lower number of traps is observed in the DLTS spectra and Arrhenius plots of these cells, shown in figures 4.6 and 4.7, in comparison to cell QD630. In fact, traps 1-700-1 and 1-700-2 were not detected by Laplace DLTS, so there is only one trap detected for each reverse voltage in the case of these two cells. All the traps are localized around the same temperature range and show similar signatures. Therefore, they correspond to the same type of defect, EL2, as will be shown in the next section.

4.2.1

Trap identification

In this section, the resulting traps will be compared with traps found in the literature in an attempt to identify their nature. The identification is based on a survey of traps reported in the literature whose nature have been determined or suggested by comparison with already known defects. The survey is based on traps of GaAs samples grown by epitaxial techniques such as MBE (Molecular Beam Epitaxy), VPE (Vapor Phase Epitaxy), as well as the MOVPE technique used for this work. Traps related to the EL2 defect will be analyzed first, whereas the remaining traps will be discussed later.

4.2.1.1

Traps related to EL2 defect

From the results exhibited in figures 4.4.a-f, it is possible to recognize the most important defect in GaAs, the well-known EL2 associated with Arsenic antisites (As_{Ga}). The hole traps related to peaks F-p630, B-SC630, B-SC700 and B-SCycle have the same characteristics of EL2, which currently are detected by DLTS around 400 K and have similar trap signatures, about [0.7-0.8] eV of activation energy and $[10^{-15} - 10^{-13}]cm^2$ of capture cross-section. Therefore, these traps are identified as EL2 centers which behave as hole traps. Schmieder *et. al.* (10) have also reported EL2 hole traps in GaAs samples, evidencing that the EL2 is able to trap both electrons and holes, a feature that is not well known in the literature.

Peak I-p570, seen in figure 4.4.a, was not resolved by Laplace DLTS, but it may correspond to EL2 defect. As the growth temperature decreases, Arsenic antisites in GaAs are more likely to form because the mobility of atoms on the growing surface becomes lower, so a portion of the Arsenic atoms does not reach their correct sites in the crystal but gallium sites. Since EL2 defect is identified in sample p630 as peak F, it is expected that this defect be also present in sample p570 as it was grown at a lower temperature. Peak I is then attributed to EL2 in sample p570 because it is located at about the same temperature range as peak F-p630.

Trap D-n570, shown in figures 4.4.c and 4.4.d, also has similar signatures to the ones of EL2, hence it can be identified as a EL2 center behaving as an electron trap. No trap has been detected in n630 with characteristics similar to EL2 defect, in contrast to sample p630 grown at the same temperature. Maybe the EL2 concentration in sample n630 is very low and produce a small change in capacitance under reverse bias voltage during DLTS and Laplace DLTS measurements. In such condition, the small change can be below the minimum resolution scale of the techniques (around 10^{-3} pF) and cannot be detected.

The EL2 defect also appears in the solar cell QD630. Traps 4-630-1, 4-630-3 and 4-630-4, seen in figures 4.5.a and 4.5.b, with activation energies of about 0.7 eV and capture cross-sections about $10^{-14} cm^2$, can be associated with EL2 behaving as an electron trap. Trap 4-630-0.25 also has similar activation energy but its capture cross-section is of about one order of magnitude lower, however, it can still be associated with EL2 behaving as a minority carrier (hole) trap. This is an interesting result because the EL2 defect turns from hole to electron trap as the minority carrier injection decreases for reverse voltages above -0.25 V. These features will be discussed in detail in the section of discussion of

DLTS results.

Another important result is that all the traps detected in solar cells QD700 and QD-s-700 are EL2 electron traps, as can be confirmed by the signatures and temperature ranges of DLTS peaks in figures 4.6 and 4.7. In contrast to solar cell QD630, no EL2 minority carrier (hole) traps are detected in cells QD700 and QD-s-700.

4.2.1.2

Traps related to the double donor state of the Arsenic antisite and trap M3, and other traps without identification

Now, the remaining traps will be analyzed here. Traps of different samples with similar signatures will be analyzed together in order to better organize the discussion. The hole traps will be treated first and later the electrons traps will be discussed.

The hole trap G of sample p570, with activation energy of 0.33 eV and capture cross-section of $8 \times 10^{-19} \text{ cm}^2$ (shown in figures 4.4.a and 4.4.b), has a signature similar to the one reported by Wang *et. al.* (41) for hole traps HMC and HZA. Those traps are found in GaAs samples doped with Magnesium and Zinc, respectively. Traps HMC and HZA are considered as being the same type of defect by the authors, so this defect seems to be independent of the type of dopant atom (the molecular configuration of the defect does not involve dopant atoms or the defect does not interact with the dopant atoms). This means that the defect probably corresponds to a native or intrinsic GaAs defect. The trap signatures of HMC and HZA exhibit a strong dependence on the hole doping concentration. For example, the HMC activation energy increases from 0.18 eV up to 0.39 eV and the capture cross-section varies from $2.7 \times 10^{-20} \text{ cm}^2$ to $1.2 \times 10^{-18} \text{ cm}^2$ when the hole concentration decreases from $4.6 \times 10^{17} \text{ cm}^{-3}$ to $1.4 \times 10^{17} \text{ cm}^{-3}$. On the other hand, the emission rates e_j of the traps HMC and HZA have been found to depend on the electric field of the depletion region, according to the Frenkel-Poole effect [(42), (43)]. This effect corresponds to a mechanism of carrier emission in which high electric fields reduce the attractive force that keeps the carriers trapped in a trap. The carriers hence require less energy to escape from the trap and reach the valence or conduction band. The carrier emission rate e_j from the trap is enhanced by the field.

The maximum electric field along the depletion region of a Schottky diode depends on the doping concentration N_d of the semiconductor as follows (39):

$$E_{max} = \frac{e}{\epsilon} N_d W(V_r) \quad (4-3)$$

where $W(V_r)$ is the depletion region width at the applied reverse voltage V_r . Since the signatures of traps HMC and HZA vary with the change in

doping concentration, it means that the signatures also vary with changes in electric field. For this reason, the emission rate e_j , linked to the trap signatures ΔE_T and σ_j as described by equation 3-2, depends on the electric field. Furthermore, the trap signatures and the emission rates can vary under different electric fields generated by different reverse voltage applied during DLTS measurements.

Another work (44) reported a very similar hole trap HM1 whose signature also depends on the electric field according to the Frenkel-Poole effect ¹. This trap was studied by an alternative DLTS technique, the double correlation DTLS, that allows the measurement of the electric field. The corresponding DLTS peak is centered at about 300 K, as well as traps HMC, HZA and our trap G-p570. The activation energy of HM1 decreases from 0.61 eV to 0.29 eV when increasing the electric field from 1.4×10^7 V/m to 2.8×10^7 V/m through variation of the reverse voltage. As the DLTS peaks of traps HM1, HMC and HZA appear on the same temperature range, and the three traps depend on the electric field according to the Frenkel-Poole model, we believe traps HM1, HMC and HZA are likely to be the same defect.

HM1 has been identified by the authors as the double donor state of the Arsenic antisite [(45),(46), (47)], mainly based on the similarity of the thermal stability of HM1 with that of the antisite. Usually, the Arsenic antisite is recognized as a defect with two donor levels, one corresponding to a singly charged state (0/+), attributed to the EL2 defect, and another one corresponding to the doubly charged state (+/+ +). The notations between brackets represent the charge of the levels when occupied by an electron, followed by the charge of the levels when empty.

We consider that trap G-p570 can be the same type of defect related to traps HM1, HMC and HZA, and hence, the double donor state of the Arsenic antisite. In fact, a very similar activation energy is measured for trap HM1 when the electric field matches that of sample p570. The electric field in sample p570 is of 2.8×10^7 V/m, calculated with equation 4-3 for -1 V (the same reverse voltage applied during DLTS measurements). Under this electric field, the activation energy of trap G-p570 is 0.33 eV, while trap HM1 exhibits an activation energy of 0.29 eV. Based on this similarity, we identify trap G-p570 as the double donor state of the Arsenic antisite.

In relation to the hole trap 4*630-0.25 of sample QD630 ($\Delta E_T = 0.47$ eV, $\sigma = 5 \times 10^{-18}$ cm²), seen in figures 4.5.a and 4.5.c, the double donor state of the Arsenic antisite is the only trap found in the literature with signatures similar to this trap depending on the electric field. According to the above

¹The Frenkel-Poole effect is verified at electric fields below 2.2×10^7 V/m by the authors

mentioned results of HM1, the electric field has to be above 1.4×10^7 V/m and below 2.8×10^7 V/m to reach an activation energy of 0.47 eV. We have calculated the electric field along the active region of cell QD630 to verify if the above condition is fulfilled. The electric field was determined by simulation using the Poisson–drift–diffusion (PDD) method of program Solcore (48). The result is shown in figure 4.9.(a). The depletion of the simulated structure covers entirely the active region, so it is about 200 nm thicker than the depletion reported for the cell at -0.25 V in figure 4.1. However, the simulation is the best approximation obtained. As observed in the figure, the electric field varies between 1.0×10^6 V/m and 1.6×10^6 V/m along the active region, approximately. These values lie outside the interval expected for trap HM1. Therefore, trap 4*630-0.25 cannot be attributed to the double charge state of the Arsenic antisite.

There is another defect behaving as a hole trap that appears in parallel in the solar cells without QDs as well as in sample p630. As can be observed in figure 4.10, the Arrhenius line of trap E-p630, initially shown in figure 4.4.(b), matches with the Arrhenius lines of traps A of samples SC700 and SCycle, initially shown in figure 4.4.(f). The corresponding trap signatures are also very similar, about 0.6 eV of activation energy and capture cross-section of $[2 - 5] \times 10^{-15}$ cm². These results demonstrate that the three traps A-SC700, A-SCycle, E-p630, and possibly also trap A-SC630, correspond to the same type of defect.

An important feature is that the signatures of traps A-SC700, A-SCycle,

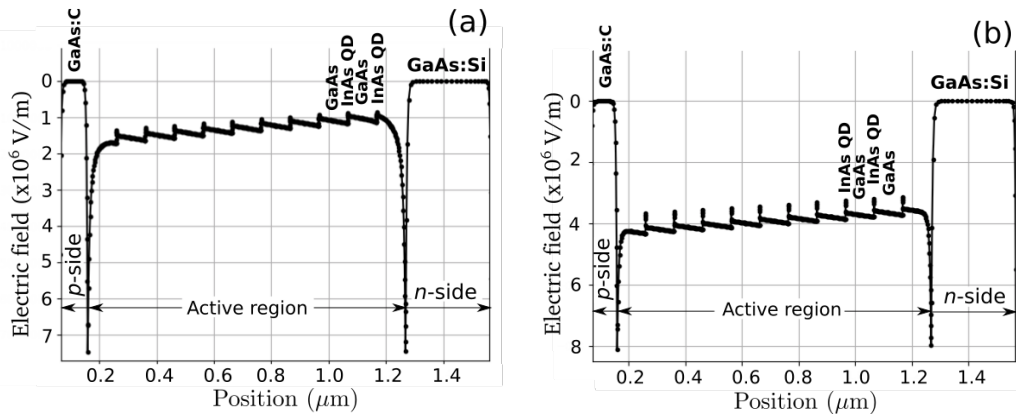


Figure 4.9: Simulation of electric field along the active region of sample QD630 for (a) -0.25 V bias and 400 K, and for (b) -3 V bias and 300 K. These voltages and temperatures represents the parameters of detection of peaks 4*-630-0.25 and 2*-630-3. The electric field over the *p* and *n*-sides is zero. The two intense peaks seen at the edges of the active region are due to charges accumulated in the *p*/active region and the active region/*n* interfaces.

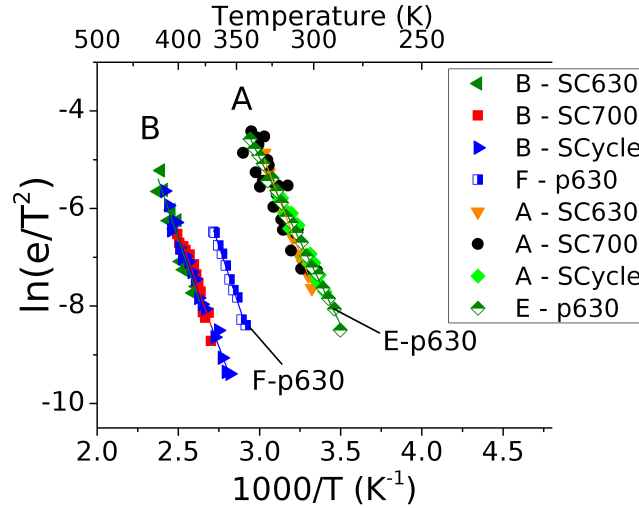


Figure 4.10: Comparison of the Arrhenius lines of hole traps of sample p630 with the ones of hole traps of the solar cells without QDs. Arrhenius line of trap E-p630 matches to the Arrhenius lines of traps A, indicating that they correspond to the same type of defect. Trap A-SC630 exhibits a slope change due to the possibly influence of electron trap H-SC630.

and E-p630 do not vary under the different reverse voltages of measurement, from -1 V (sample p630) to -3 V (cell SCycle). These reverse voltage can be confirmed in figures 4.4.(a) and (e). Using program Solcore, we have determined the electric fields over the active regions of cells SC630, SC700, and SCycle, obtaining the following ranges: $[2.9 - 4.4] \times 10^6$ V/m, $[2.3 - 4.0] \times 10^6$ V/m, and $[2.8 - 4.3] \times 10^6$ V/m. The maximum electric field in the depletion of sample p630 was also calculated using equation 4-3, obtaining 8.7×10^6 V/m. Then, there are no significant changes in the electric field ranges of the solar cells without QDs, but a considerable increase is noted for sample p630. Despite this, the signatures of traps A-SC700, A-SCycle, and E-p630 are not influenced by the electric field. For this reason, these traps cannot be associated with the double donor state of the Arsenic antisite nor with hole trap G-p570.

A defect similar to traps A-SC700, A-SCycle, and E-p630, and independent of the electric field, is the Iron acceptor (49), (50). However, this acceptor is only found in GaAs doped with Iron or in GaAs samples grown in reactor chambers contaminated with Iron. We do not use Iron as a dopant in our laboratory nor use gas sources which contain this element. Hence, we rule out the Iron acceptor as the defect related to the traps in question. These traps remain unidentified.

Hole trap 4-630-0.5 ($\Delta E_T = 1.02$ eV, $\sigma = 4 \times 10^{-12}$ cm²), seen in figures 4.5.a and 4.5.c, has an activation energy higher than the activation energies of traps frequently found in GaAs. No traps were found in the literature with similar signatures and nearby DLTS peak position, so that trap 4-630-0.5 could

not be identified.

Now, the remaining electron traps will be discussed here. Trap H-SC630 (figures 4.4.e and 4.4.f) and trap 2-630-3 (figures 4.5.a and 4.5.b) have similar activation energies, but their capture cross-sections differ in one order of magnitude. Trap H-SC630 has an activation energy of 0.25 eV and capture cross-section of $2.4 \times 10^{-19} \text{ cm}^2$, whereas trap 2-630-3 has an activation energy of 0.30 eV and capture cross-section of $2.0 \times 10^{-18} \text{ cm}^2$. To verify if these two traps correspond to the same defect, the corresponding Arrhenius lines have been plotted together in figure 4.11. The Arrhenius lines, however, do not match, indicating that the two traps do not correspond to the same type of defect.

Two traps in the literature have been found with activation energies similar to the ones of traps H-SC630 and 2-630-3, the well-known electron traps M4(1) and M4(2) [(51), (52), (53)]². This pair of traps corresponds to one of two metastable molecular configurations of a defect attributed to a pairing of a native acceptor or complex with a shallow donor [(51), (53)]. The above features are mainly based on thermal annealing studies. The other metastable configuration corresponds to the electron trap called M3, which has the highest energy level. M4(1) e M4(2) were initially considered as a single trap, because of the single peak observed in DLTS. However, more detailed studies have shown the existence of two different traps with very similar signatures ($\Delta E_T \sim 0.3 \text{ eV}$, $\sigma \sim 10^{-15} \text{ cm}^2$), whose DLTS peaks overlap and form an apparent single DLTS peak [(53), (54)].

Despite the activation energies of traps H-SC630 and 2-630-3 being

²Also called M4(a) and M4(b)

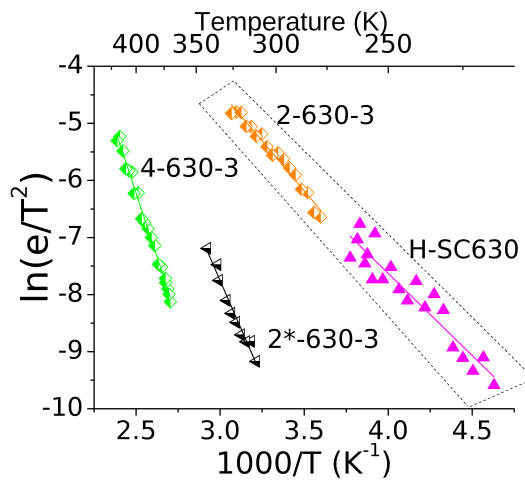


Figure 4.11: Comparison between the Arrhenius lines of electron traps of sample QD630 obtained at -3 V and the Arrhenius line of electron trap H of sample SC630.

similar to the ones of traps M4(1) and M4(2), the respective capture cross-sections are several orders of magnitude lower. Therefore, traps H-SC630 and 2-630-3 cannot be identified.

On the other hand, the electron trap 2*-630-3 of sample QD630 ($\Delta E_T = 0.58$ eV, $\sigma = 1 \times 10^{-15}$ cm^2), shown in figures 4.5.(a) and (b), has similar signatures to the ones reported for trap M3. Moreover, the DLTS peak position of this trap has been reported around 300 K [(51), (55)], near the DLTS peak position of trap 2*-630-3, around 290 K. Trap M3 is broadly known by its dependence on the electric field, following the Frenkel-Poole model [(51),(52),(53)], so we have to take this feature into account to compare it with our traps. Buchwald *et. al.* (51) reported an activation energy of 0.61 eV and a capture cross-section of 3.1×10^{-14} cm^2 under an electric field of 2.2×10^6 V/m, while Tokuda *et. al.* (53) reported 0.47 eV and 3.6×10^{-13} cm^2 at 1.25×10^7 V/m. To compare the signatures of trap 2*-630-3 under the effect of the electric field of cell QD630 with the signatures of the above references, a second simulation of the electrostatic potential of the cell was made. The resulting electric field along the depletion region is shown in figure 4.9.(b), where a variation between 3.5×10^6 V/m and 4.3×10^6 V/m is observed. These values are slightly higher than the electric field reported by Buchwald *et. al.*, and the activation energy reported by these authors of 0.61 eV is very close to the activation energy of trap 2*-630-3, of 0.58 eV. However, the capture cross-section of trap 2*-630-3 is one order of magnitude lower. Despite this difference, we do not rule out the possibility that trap M3 is the same as trap 2*-630-3.

There is an electron trap found in a low temperature MBE-grown GaAs sample with an activation energy of 0.64 eV and a capture cross-section of 1×10^{-14} cm^2 reported by Mooney *et. al.* (56). The signatures of this trap are similar to the ones of trap 3-630-0.5 (figures 4.5.a and 4.5.b), which has an activation energy of 0.62 eV and a capture cross-section of 3×10^{-14} cm^2 . Also, the corresponding DLTS peak position of that trap is around 370 K, near the DLTS peak position of trap 3-630-0.5, around 360 K. The trap in the MBE-grown GaAs sample has been associated with an Arsenic antisite-related defect previously detected in the same type of sample by other techniques than DLTS (optically detected electron paramagnetic resonance -ODEPR-, magnetic circular dichroism of the absorption -MCDA- and photocurrent [(57), (58)]). The antisite related to this defect is different from the doubly charged Arsenic antisite since it is found as singly charged ($(As_{Ga})^+$), and probably form a complex with the negatively charged Gallium vacancy (V_{Ga}) [(59), (60)]. This complex is different from the EL2 complex which is more probably formed

with a singly charged Arsenic antisite and an Arsenic interstitial (As_i) [(61), (62)].

This may be the first detection of such $(As_{Ga})^+$ antisite-related defect in a MOVPE-grown GaAs sample. However, future studies are needed to prove if the charge and the electrical and thermal behavior of trap 3-630-0.5 correspond to an Arsenic antisite.

Concerning the electron trap C-n630, seen in figures 4.4.c and 4.4.d, this trap has an activation energy of 0.67 eV and a capture cross-section of $5 \times 10^{-15} \text{ cm}^2$. Despite the similarity of its signatures with the signatures of trap 3-630-0.5, those traps are not the same type of defect, because their Arrhenius lines do not match each other, as seen in figure 4.12. However, the activation energy of trap C-n630 is also close to the activation energy of 0.65 eV of the already mentioned Arsenic antisite-related defect found in low MBE-grown GaAs. Additional studies are needed to prove if such defect is related to trap C-n630 or trap 3-630-0.5. On the other hand, the possibility of trap C-n630 being related to trap M3 is ruled out, because the DLTS peak position of trap C-n630, around 395 K, is far away from the DLTS peak position reported for trap M3, around 300 K.

Finally, we discuss peaks 1-630-1 and 2-630-1 of cell QD630 (figures 4.5.(a) and (b)) which have activation energies of 0.16 eV and 0.19 eV, respectively, and capture cross-sections in the range of $2 \times 10^{-20} \text{ cm}^2$ to $4 \times 10^{-19} \text{ cm}^2$. These low activation energies and very low capture cross-sections are comparable to the ones obtained for electron emissions from the confined energy levels of InAs QDs embedded in GaAs reported by references (63) and (64). If peaks 1-630-1 and 2-630-1 correspond to this same type of emission,

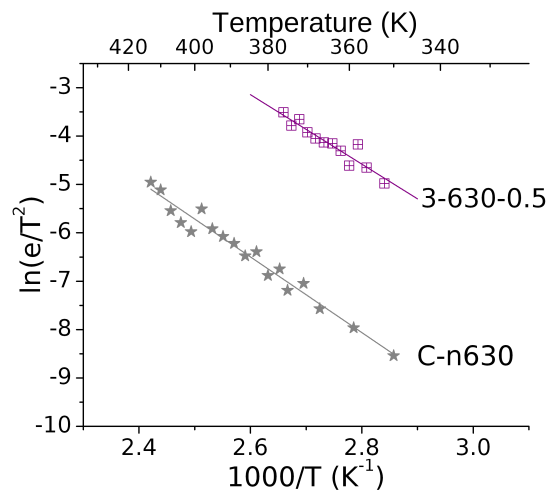


Figure 4.12: Comparison between the Arrhenius lines of electron traps C-n630 and 3-630-0.5.

their activation energies have to match with the energy difference between some QD confined energy level for electrons and the GaAs conduction band minimum level.

Simulations of the band structure and the QD confined energy levels of cell QD630 have been performed with nexnato3 program (65) based on photoluminescence measurements. The details of these simulations are not presented here, but in the next chapter of photoluminescence results, where the respective PL spectra are shown and analyzed. The analysis of the spectra of cell QD630 leads to the identification of the ground and the first excited states for electrons and holes in the QDs. In addition, the simulations combined with the photoluminescence experimental data show that the QDs may contain Gallium in percentages up to 40%. It means that the QDs are composed of InAs or $In_{1-x}Ga_xAs$ with $x \leq 0.4$. All these results will also be described in the next chapter.

The energy levels of the two QD energy states identified in cell QD630, the ground state (E1) and the first excited state (E2), have been calculated based on the above results and for three possible Gallium contents of the QDs, 0%, 20%, and 40%. Table 4.1 shows these energy levels with respect to the GaAs conduction band (CB) at the temperatures of the maxima of peaks 1-630-1 (230 K) and 2-630-1 (300 K). It has also been considered a possible height range of the QDs for each Gallium content. For this reason, the respective energy levels are within a certain range of values.

The activation energies of peaks 1-630-1 (0.16 eV) and 2-630-1 (0.19 eV) fall within the energy ranges calculated for the E1-CB and E2-CB electron transitions inside QDs with 0% of Gallium content. Therefore, it is appropriate to say that these peaks probably correspond to electron emissions from QDs with less than 20% of Gallium. Furthermore, the temperatures of measurement of the peaks are more than enough to induce thermally such electron emissions (66).

It is worth to note that the additional energy for electron escape from the QDs energy levels due to *strain effects* (~ 0.1 eV) has been taken into account

Transition	Temperature	Transition energy (meV)		
		Ga 0%	Ga 20%	Ga 40%
E1-CB	230 K	165-223	107-158	86-130
E2-CB		141-166	92-114	65-92
E1-CB	300 K	151-211	99-149	74-127
E2-CB		128-150	83-107	59-84

Table 4.1: Simulated energy levels of the QD energy states identified in cell QD630 with respect to the top of the GaAs conduction band energy barrier.

for the calculations of the E1-CB and E2-CB transition energies. Strain effects are intrinsic to the GaAs/InAs QDs systems [(67), (68)]. It is well-known that the mismatch between the lattice parameters of GaAs and InAs materials allows the spontaneous formation of the InAs QDs and, in this way, the strain due to the mismatch is reduced. However, the strain is not totally compensated and, in consequence, strain fields usually extend from the top of the QDs into the surrounding GaAs layers. These strain fields add energy barriers at the interfaces of the QDs with the GaAs layers as schematized in figure 4.13, so the energy necessary for electrons to escape from the QD energy levels to the conduction band becomes higher.

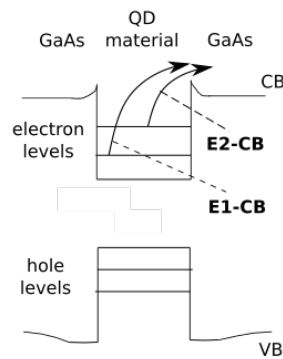


Figure 4.13: Scheme of the possible electron emissions from the QDs to the GaAs conduction band in cell QD630.

4.3

Discussion of the results of DLTS and Laplace DLTS

4.3.1

C-doped and Si-doped GaAs samples

The parameters of the traps detected in the individually doped GaAs layers are detailed in table 4.2. The signatures, concentrations, and the types of defects attributed to the traps are also included. The concentrations were calculated as described at the end of section 4.1.

Three hole traps were detected in the *p*-doped samples and two electron traps were detected in the *n*-doped samples. Among all these traps, two traps were identified as EL2, being one a hole trap in sample p630 (trap F) and being the other one an electron trap in sample n570 (trap D). We consider trap I, detected in sample p570, also as an EL2 trap since it is detected by DLTS around the same temperature range as trap F (see figure 4.4.(a)), and since an increase in the EL2 concentration at low growth temperatures is expected.

SOLAR CELLS WITHOUT QDs						
Sample	V_r (V)	Trap	ΔE_T (eV)	σ (cm^2)	N_T (cm^{-3})	Identity
SC630	-2.5	H	0.25 +/- 0.02	(2.4 +/- 2.3) $\times 10^{-19}$	(1.26 +/- 0.01) $\times 10^{14}$	un.
		A	0.76 +/- 0.03	(1.7 +/- 1.7) $\times 10^{-12}$	(2.34 +/- 0.02) $\times 10^{14}$	un;
		B	0.84 +/- 0.07	(3.5 +/- 7.2) $\times 10^{-14}$	(2.80 +/- 0.04) $\times 10^{14}$	EL2
SC700	-2	A	0.60 +/- 0.05	(1.8 +/- 4.9) $\times 10^{-15}$	(3.31 +/- 0.06) $\times 10^{13}$	un.
		B	0.82 +/- 0.06	(2.3 +/- 4.1) $\times 10^{-14}$	(1.15 +/- 0.02) $\times 10^{14}$	EL2
SCycle	-3	A	0.60 +/- 0.03	(5.2 +/- 5.2) $\times 10^{-15}$	(2.80 +/- 0.01) $\times 10^{14}$	un.
		B	0.77 +/- 0.02	(4.9 +/- 3.5) $\times 10^{-15}$	(6.86 +/- 0.02) $\times 10^{14}$	EL2
INDIVIDUALLY DOPED GaAs SAMPLES						
p570	-1	G	0.33 +/- 0.02	(8.5 +/- 6.6) $\times 10^{-19}$	(7.3 +/- 0.5) $\times 10^{13}$	(AsGa) ⁺⁺
p630	-1	E	0.59 +/- 0.01	(3.7 +/- 1.0) $\times 10^{-15}$	(3.4 +/- 0.2) $\times 10^{14}$	un.
		F	0.86 +/- 0.02	(5.8 +/- 4.5) $\times 10^{-13}$	(1.1 +/- 0.1) $\times 10^{14}$	EL2
n570	-1	D	0.81 +/- 0.01	(1.5 +/- 0.3) $\times 10^{-13}$	(1.2 +/- 0.1) $\times 10^{14}$	EL2
n630	-1	C	0.67 +/- 0.03	(5.0 +/- 4.5) $\times 10^{-15}$	(2.4 +/- 0.1) $\times 10^{14}$	un.

Table 4.2: Details of the traps detected in the active regions of the solar cells without QDs and in the individually doped GaAs samples. The hole traps are highlighted in grey. The rest of the traps are electron traps. The term un. means unidentified. The errors of ΔE_T and σ were calculated depending on the degree of fit of the Arrhenius data points to straight lines. The trap concentrations N_T were calculated from the DLTS peak heights determined by fitting the DLTS peaks with Gaussian functions. The errors of N_T derive from the degree of these fits.

Another hole trap was identified as the double donor state of the Arsenic antisite, trap G, which is dependent on the electric field following the Frenkel-Poole model. The rest of the traps could not be identified, although one of them, trap C of sample n630, has characteristics similar to an electron trap commonly found in low-temperature MBE-grown GaAs attributed to an Arsenic antisite-related defect.

To discuss the results of DLTS and Laplace DLTS of the individually doped GaAs samples, it should be kept in mind the aim of the study on these samples. Samples p570 and n630 represent the C-doped and Si-doped GaAs layers comprising the *p* and the *n*-sides of the IB solar cells. The growth temperatures of these samples are also the same as those for the *p* and *n* sides (570 °C and 630 °C, respectively), although they were doped with lower carbon and silicon concentrations to produce Schottky diodes for the DLTS and Laplace DLTS measurements. The hole concentration in sample p570 and the electron concentration in sample n630 are about $1 \times 10^{17} \text{ cm}^{-3}$, whereas the concentrations in the *p* and *n*-sides of the IB solar cells reach $2 \times 10^{18} \text{ cm}^{-3}$.

Sample p630 was designed to study the effect of the higher growth temperature of the window GaInP layer (630 °C) on the defects of the *p*-side. In a similar way, sample n570 was designed to study the influence of the lower growth temperatures, to which each cell is subjected after the *n*-side is grown, on the defects on this side. Hence it can be assumed that the traps detected in samples p630 (hole traps E and EL2) and n570 (EL2 electron trap) can also be present in the *p* and *n*-sides of the solar cells, respectively.

The identification of the EL2 defect in the individually GaAs samples (as traps I, F and D) indicates the presence of this defect in the *p* and *n*-sides of all the solar cells. This result was expected since EL2 is also detected as traps B in the GaAs active regions of the cells without QDs with *p*-type residual doping³, and detected around 400 K in the *n*-doped GaAs active regions⁴ of the IB solar cells (see figures 4.4.(e) and (f), 4.5, 4.6, and 4.7). It means that the defect is present in our GaAs layers, regardless of whether they are intentionally doped or not or if they are doped with carbon or silicon.

It is not possible to establish if exist a relation between the *p* and *n*-type concentrations of the individually GaAs doped samples and the EL2 concentration since this defect was only detected in one of the two C-doped samples (only detected in sample p630) and in one of the two Si-doped samples (only detected in sample n570). Hence, we are not able to determine the effect of the higher concentrations of the *p* and *n*-sides of the solar cells on the EL2

³This residual doping is assumed to be due to residual carbon.

⁴This *n*-type doping is assumed to be due to the silicon over the InAs QDs

concentrations.

In relation to traps G (sample p570) and E (sample p630), they were detected by DLTS within nearby temperature ranges. Despite this, they are related to different types of defects. Since trap G corresponds to an Arsenic antisite (the double donor of the Arsenic antisite), it is expected to decrease in concentration at higher growth temperatures. This is because the rate of the decomposition of the Arsine (the gas source for Arsenic) is increased during growth (15), leading to higher incorporation of Arsenic in the GaAs lattice and the reduction of the Arsenic antisites (69). Therefore, if trap E was also the double donor of the Arsenic antisite as trap G, trap E should have a lower concentration than trap G, it means, lower than $7.3 \times 10^{13} \text{ cm}^{-3}$. Instead, the concentration of trap E is found to be of $3.4 \times 10^{14} \text{ cm}^{-3}$. In conclusion, trap E cannot be related to the same type of defect as trap G.

In any way, the identification of the double donor of the Arsenic antisite as trap G in sample p570 proves that this defect is present in the *p*-sides of our solar cells in a relatively low concentration. This concentration should not be increased by the increase of the temperature to 630 °C during the growth of the windows layer, according to the above discussion. However, the defect related to trap E could be formed during this growth step, as indicated by its detection in sample p630.

Finally, in relation to the unidentified trap C, detected in sample n630, no similar trap is detected in sample n570 (see figures 4.4.(c) and (d)). Then, it is clear that the related defect has only an appreciable concentration at temperatures above 570 °C. This fact is an evidence that trap C is not related to Arsenic antisites since the concentrations of these centers are expected to decrease with the increase in the growth temperature. Hence, trap C cannot be the Arsenic antisite-related defect found in low-temperature MBE-grown GaAs despite their signatures being similar. Since the *n*-sides of the solar cells were grown at 630 °C, the presence of the trap C-related defect in these sides is expected.

4.3.2

Solar cells without QDs

The information of the traps detected in the active region of the solar cells without QDs are also included in table 4.2. The majority carrier traps A and B were detected in all the three cells, and an additional minority carrier trap H was detected only in cell SC630. Only traps B have been properly identified and attributed to EL2. Trap A could not be identified, but it was concluded that it corresponds to the same type of defect, which is independent

of the electric field, at least, within the reverse voltage range of measurement ($[-2 \text{ V}, -3 \text{ V}]$).

It should be considered that the purpose of the study of cells SC630 and SC700 is to detect defects present in the active regions of cells QD630 and QD700 that are not related to (or induced by) the growth of the QDs. In other words, the aim is to detect the traps induced solely by the growth conditions, mainly, by the growth temperature of the GaAs spacer layers. With that said, hole traps A and trap EL2 should also be present in the active regions of cells QD630 and QD700, as well as trap H in cell QD630, and related to the respective growth temperatures of $630 \text{ }^\circ\text{C}$ and $700 \text{ }^\circ\text{C}$.

On the other hand, solar cell SCycle was studied to determine the influence of the temperature cycle under which the QDs of cells QD700 and QD-s-700 are grown (the cycle of InAs growth at $500 \text{ }^\circ\text{C}$, followed by the annealing at $700 \text{ }^\circ\text{C}$). No additional traps are detected in cell SCycle besides the hole traps already detected in cells SC630 and SC700. It means that the temperature cycle does not induce the formation of additional hole traps.

It is important to note that the IB solar cells, as well as the solar cells without QDs, were studied under the effect of majority carrier injection to focus on the detection of majority carrier traps. For this reason, hole traps were mainly detected in the active regions of the solar cells without QDs, and electrons traps were mainly detected in the active regions of the IB solar cells⁵. It means that we have indirectly measured the minority carrier (hole) traps of the active regions of the IB solar cells based on the study of the solar cells without QDs. These traps are, of course, the hole traps A and EL2 and, as already mentioned, their formation is not induced by the growth of the QDs.

Despite to apply a DLTS majority carrier (hole) injection pulse to cell SC630, the electron trap H was detected in its active region as a result of a small electron injection, as deduced at the beginning of section 4.2 and schematized in figure 4.8.(b). It is clear that trap H corresponds to a majority carrier (electron) trap in the active region of cell QD630.

We believe that the small electron injection has also occurred in the active regions of cells SC700 and SCycle since the structures of these cells are very similar to that of cell SC630. Thus, trap H could be detected in these cells if present. But, since it was not detected, it is valid to affirm that the increase in the growth temperature to $700 \text{ }^\circ\text{C}$ inhibits the formation of trap H in the active regions of cells SC700 and SCycle or reduce its concentration to a value under the limit of detection by DLTS and Laplace DLTS. In addition, trap H

⁵This is due to the type of doping of the active regions: (unintentionally) p -doped in the case of cells without QDs and n -doped in the case of the IB solar cells

should not be present in the active regions of cells QD700 and QD-s-700 since it is not detected in cells SC700 and SCycle.

Curiously, trap H does not appear among the electron traps directly detected in the active region of cell QD630. This fact can be confirmed comparing the signatures of trap H (figure 4.4.(f)) with the ones of traps of cell QD630 (figure 4.5.(b)). Only the signatures of trap 2-630-3 are similar, but the Arrhenius lines of this trap and trap H do not match each other (see figure 4.11), meaning that these traps correspond to different types of defects. However, probably trap H is in the active region of cell QD630, but its observation in the DLTS spectra and Arrhenius plots of this cell is not possible because other traps of higher concentration are detected around the same temperature range that trap H ([180 K-280 K]). These traps are 1-630-1, 2-630-1 and 2-630-3, whose concentrations are of the order of 10^{15} cm^{-3} , about one order of magnitude higher than the concentration of trap H of $1.3 \times 10^{14} \text{ cm}^{-3}$. As they are more concentrated, they generate greater DLTS signals and may overshadow the DLTS signal of trap H.

Now, the influence of the growth temperature of the spacer layers and the temperature cycle on traps A and EL2 can be seen through the variation of their concentration, figure 4.14. Evidently, a decrease in concentration of both traps is obtained with the increase of the growth temperature to 700 °C. This means that there is a lower density of these hole traps in the active regions of cells QD700 and QD-s-700 compared to cell QD630. This result also agrees with the higher efficiencies of cells QD700 and QD-s-700. On the other side, the implementation of the temperature cycle increases the concentration of both traps, probably due to the decrease of the temperature to 500 °C during each cycle. Indeed, the concentration of the Arsenic antisite and, hence, the concentration of EL2 are expected to increase at lower growth temperatures. This is due to reduced Arsenic incorporation into the GaAs lattice and the reduced mobility of the Arsenic atoms on the growth surface that avoids part of them to reach the correct sites in the lattice and induces them to take the nearby antisites.

It is very probable that the real concentration of trap A in cell QD630 is higher than that measured on cell SC630 because of the temperature cycle, which was not included in the growth steps of this last cell. On the other hand, the concentration of trap A, measured in cell SCycle, should be closer to the real concentrations in cells QD700 and QD-s-700. In any case, the reduction of the trap A density must be achieved with the increase in the growth temperature.

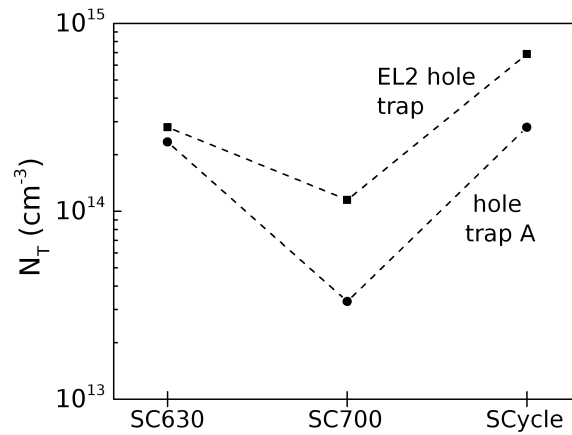


Figure 4.14: Concentration of the hole traps A and EL2 detected in the active regions of the solar cells without QDs.

4.3.3

IB Solar cells

The traps detected in the active regions of the IB solar cells are listed in table 4.3. EL2 is the common defect in the three solar cells. In cell QD630, this defect shows two roles: as majority carrier (electron) trap at reverse voltages above -1 V, and as a minority carrier (hole) trap at -0.25 V. Other hole traps were also detected below -0.5 V. However, among the hole and electron traps of this cell, only the EL2 defect and trap M3 could be identified.

The most important feature observed from the DLTS and Laplace DLTS results of the IB solar cells is the high number of traps detected in the active region of cell QD630, contrary to the single EL2 electron trap observed in the active regions of cells QD700 and QD-s-700. We deduce that the electrons and holes traps not related to EL2 are suppressed or reduced to a low concentration, below the minimum level of DLTS detection by increasing the growth temperature of the GaAs spacer layers and the annealing temperature of the QDs from 630 °C to 700 °C. Probably, this reduction of trap concentration contributes to the increase in energy conversion efficiency of cells QD700 (5.1%) and QD-s-700 (6.9%) in comparison to cell QD630 (2.8%), as shown in figure 4.15.

We assume the above assumption, even without taking into consideration the nature of each one of the traps. But it is clear that each one has a particular influence on the efficiency of the cell. Next, we will discuss the probable influence of the traps which were identified, traps EL2 and M3, on the IB cells.

Sample	Trap	ΔE_T (eV)	σ (cm ²)	N_T (cm ⁻³)	Identity
QD630	4-630-0.25	0.71 +/- 0.02	(1.3 +/- 0.7) × 10 ⁻¹⁵	(1.7 +/- 0.4) × 10 ¹⁶	EL2
	4*-630-0.25	0.47 +/- 0.04	(5.5 +/- 5.9) × 10 ⁻¹⁸	(1.4 +/- 0.3) × 10 ¹⁶	un.
	3-630-0.5	0.62 +/- 0.07	(2.7 +/- 5.8) × 10 ⁻¹⁴	(2.4 +/- 0.5) × 10 ¹⁵	un.
	4-630-0.5	1.02 +/- 0.03	(4.2 +/- 4.1) × 10 ⁻¹²	(4.6 +/- 1.0) × 10 ¹⁵	un.
	1-630-1	0.16 +/- 0.01	(1.9 +/- 0.6) × 10 ⁻²⁰	(4.4 +/- 0.9) × 10 ¹⁵	un.
	2-630-1	0.19 +/- 0.01	(4.3 +/- 2.8) × 10 ⁻¹⁹	(4.0 +/- 0.9) × 10 ¹⁵	un.
	4-630-1	0.74 +/- 0.03	(2.8 +/- 2.4) × 10 ⁻¹⁴	(4.5 +/- 1.0) × 10 ¹⁵	EL2
	2-630-3	0.30 +/- 0.01	(2.0 +/- 1.0) × 10 ⁻¹⁴	(6.9 +/- 1.4) × 10 ¹⁵	un.
	2*630-3	0.58 +/- 0.04	(1.4 +/- 1.7) × 10 ⁻¹⁵	(4.3 +/- 0.9) × 10 ¹⁵	M3
	4-630-3	0.77 +/- 0.02	(5.1 +/- 2.6) × 10 ⁻¹⁴	(1.2 +/- 0.2) × 10 ¹⁶	EL2
QD700	4-630-4	0.74 +/- 0.02	(2.5 +/- 1.8) × 10 ⁻¹⁴	(1.5 +/- 0.4) × 10 ¹⁵	EL2
	2-700-0.25	0.74 +/- 0.02	(2.8 +/- 1.7) × 10 ⁻¹⁴	(1.8 +/- 0.8) × 10 ¹⁵	EL2
	2-700-0.5	0.73 +/- 0.01	(1.5 +/- 0.5) × 10 ⁻¹⁴	(5.0 +/- 0.5) × 10 ¹⁵	EL2
	2-700-1	0.79 +/- 0.01	(5.5 +/- 1.3) × 10 ⁻¹⁴	(4.1 +/- 0.5) × 10 ¹⁵	EL2
	2-700-2	0.86 +/- 0.02	(4.9 +/- 2.8) × 10 ⁻¹³	(4.0 +/- 0.8) × 10 ¹⁵	EL2
	2-700-3	0.71 +/- 0.02	(4.2 +/- 2.0) × 10 ⁻¹⁵	(6.0 +/- 0.7) × 10 ¹⁵	EL2
	1-QD-s-1	0.76 +/- 0.01	(2.8 +/- 0.7) × 10 ⁻¹⁴	(3.0 +/- 0.1) × 10 ¹⁵	EL2
	1-QD-s-4	0.78 +/- 0.01	(3.3 +/- 0.7) × 10 ⁻¹⁴	(3.0 +/- 0.1) × 10 ¹⁵	EL2
QD-s-700	1-QD-s-6	0.79 +/- 0.01	(4.7 +/- 1.3) × 10 ⁻¹⁴	(1.9 +/- 0.1) × 10 ¹⁵	EL2

Table 4.3: Details of the traps detected in the active regions of the IB solar cells by DLTS and Laplace DLTS. The hole traps are highlighted in grey. The rest of the traps are electron traps. The term un. means unidentified. The errors of ΔE_T and σ were calculated depending on the degree of fit of the Arrhenius data points to straight lines. The trap concentrations N_T were calculated from the DLTS peak heights determined by fitting the DLTS peaks with Gaussian functions. The errors of N_T derive from the degree of these fits.

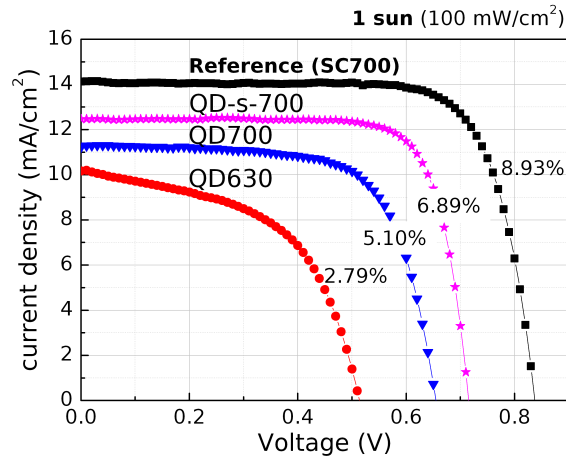


Figure 4.15: IV characteristics and percentages of the energy conversion efficiency of the IB solar cells. The IV of a reference cell with a 1 μm -thick GaAs active layer, equivalent to cell SC700, is also shown for comparison. Reprinted with permission after (12).

We believe that the EL2 defect could be a non-radiative recombination center in the active regions of the IB solar cells since this defect acts as both an electron trap and a hole trap. This double role is directly observed from the results of the DLTS spectra of cell QD630, as described above (see table 4.3). In the case of cells QD700 and QD-s-700, the role of EL2 as an electron trap is directly seen from the results of the respective spectra (table 4.3), while the role as a hole trap is indirectly observed from the results of the spectra of cells SC700 and SCycle in the form of traps B (table 4.2).

The DLTS and Laplace DLTS techniques are only able to detect defects in the form of traps, so there is no way to prove that EL2 is really a recombination center in the active regions of our cells. However, considering the double role of EL2, it might allow the recombination of e-h pairs in the presence of free excess carriers, which is the condition of the operation of the solar cell.

In fact, EL2 has its energy level near the middle of the gap. For this type of defect, the electron emission rate is lower than for electron traps with levels closer to the conduction band, according to equation 3-2. Similarly, the hole emission rate is lower than for hole traps with levels closer to the valence band. As a consequence, the re-emission of electrons and holes captured by "midgap" defects to the bands is less probable. This feature generally makes the midgap defect an efficient recombination center.

As already known, recombination centers are not desirable in a solar cell as they reduce the photocurrent generated by the cell, leading to a decrease in the energy conversion efficiency. Therefore, the double role of the EL2 could be inducing a negative effect on the performance of our solar cells.

Our assumption of EL2 as a recombination center coincides with the

recent assumptions of Schmieder *et. al.* (10). These authors also identified EL2 as both a majority and minority carrier trap in the active regions of GaAs solar cells. They assume that, at high concentration, the defect is an effective recombination center, contributing to the reduction of the quality of the cells.

Now, we turn the attention to the concentrations of EL2 in the active regions of the IB solar cells. Figure 4.16 shows the calculated EL2 concentrations, obtained at the different reverse voltages applied to the cells. A large variation in the calculated EL2 concentrations for cell QD630 is seen in the figure, while lower variations are seen in the case of cells QD700 and QD-s-700. In the case of cell QD630, we expected to obtain similar EL2 concentrations between -0.25 V and -4 V since the thickness of the depletion of this cell is almost constant along this reverse voltage range (barely increased by 20 nm, as observed from figure 4.1). It means that practically the same depletion region was monitored by DLTS between -0.25 V and -4 V.

We believe that variation in the calculated EL2 concentrations is due to the way these concentrations were calculated. The used formula (equation 3-5) includes the steady-state capacitance C_2 , which changes with the reverse voltage and the electron occupation state of the traps present in the cell. As shown in figure 3.1, C_2 is the capacitance at a certain reverse voltage V_r when the equilibrium state is restored in the diode within a large period of time after the DLTS bias pulse is applied. As the reverse voltage is increased (from one DLTS scan to another), the position of the Fermi energy level is gradually moved down, so that the traps levels lying above the Fermi level are emptied. Therefore, the electron occupation state of the traps is varied as a function of the reverse voltage.

Since many traps are present in the active region of cell QD630, the occupation states of all these traps are varied at the same time when the reverse voltage is increased. These simultaneous changes should cause large variations of C_2 which are finally reflected in the calculation of the EL2 concentrations at the different reverse voltages. In the case of cells QD700 and QD-s-700, only the occupancy of trap EL2 is varied with the reverse voltage, so a smaller variation is observed.

Considering the average between the EL2 concentrations at the different reverse voltages for each cell, an important result is seen. As shown in figure 4.16, the average EL2 concentration in cell QD630 exceeds the average EL2 concentrations in the other two cells. This result agrees with the higher EL2 concentration in cell SC630 in comparison with the EL2 concentration in cell SC700, figure 4.14. A small difference is seen between the concentrations in the

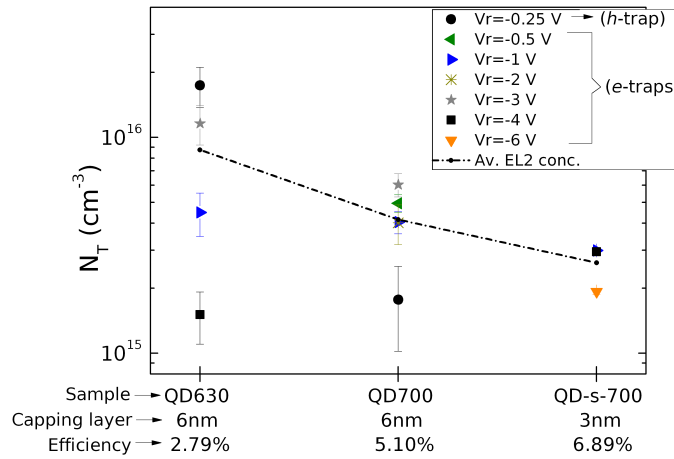


Figure 4.16: The concentration of the EL2 defect determined at the different DLTS reverse voltages in each IB solar cell. The variation of the average concentration between the cells is represented by the dotted black line.

cells QD700 and QD-s-700. Therefore, an increase in the efficiency of these cells as a consequence of a decrease in the EL2 concentration in their active regions is evident. This decrease is in agreement with the reduction of Arsenic antisites at higher growth temperatures, as already mentioned in the last section.

It is worth to note that the average EL2 concentration in cell QD630 (of $8.8 \times 10^{15} \text{ cm}^{-3}$) exceeds the EL2 concentration in cell SC630 (of $2.8 \times 10^{14} \text{ cm}^{-3}$). This excess is, therefore, a consequence of the QD growth conditions, including the temperature cycle. In a similar way, the average EL2 concentrations in cells QD700 and QD-s-700 (of $4.2 \times 10^{15} \text{ cm}^{-3}$ and $2.6 \times 10^{15} \text{ cm}^{-3}$, respectively) slightly exceeds the EL2 concentration in cell SCycle. Although the excess is small, it cannot be ruled out the possibility of an additional increase in EL2 concentration caused by other growth conditions of the QDs besides the temperature cycle.

The increase in the energy conversion efficiency for cells QD700 and QD-s-700 is also evidenced by the increase of their external quantum efficiency (EQE), figure 4.17. EQE represents the ratio of the number of electrons collected by a solar cell to the number of incident photons of a given energy. The energy range above the GaAs band gap ($> 1.42 \text{ eV}$) represents the light absorption by means of the valence band-to-conduction band transitions in the active region of the cell. The energy range below the gap (the sub-bandgap absorption range) specifically represents the light absorption by the QDs, i.e., the absorption through the electron transitions between the intermediate band, formed by the QD confined energy levels, and the conduction band. From the figure, an increase of the EQE is observed from cell QD630 to cells QD700 and QD-s-700 above 1.42 eV . This result agrees with the decrease in EL2

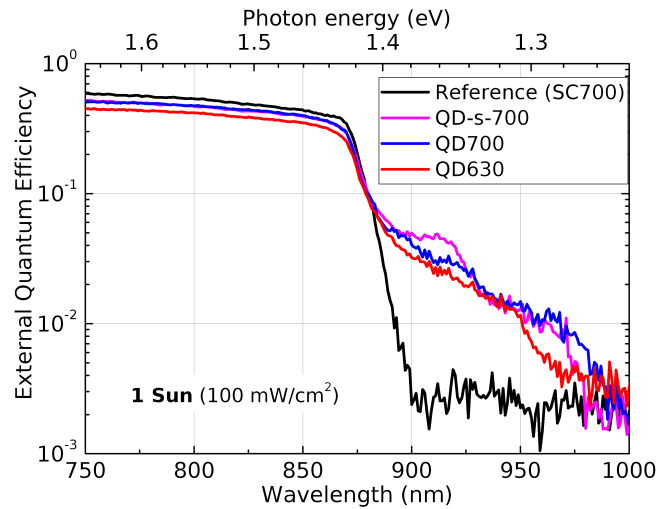


Figure 4.17: External quantum efficiency (EQE) of the IB solar cells at 300 K. The light absorption by the QDs is observed within the sub-bandgap range (energy < 1.42 eV). Reprinted with permission after (12).

concentration and the reduction of the number of detected traps. No change is observed between cells QD700 and QD-s-700 in this range, most likely due to the similar EL2 concentrations and the fact that there are no additional traps in these cells, according to our results from DLTS and Laplace DLTS.

Below 1.42 eV, the EQE increases due to the enhancement of the absorption by the QDs, mainly for cell QD-s-700, with thinner capping layers of 3 nm. As will be shown in the chapter of photoluminescence results, the reduction of the thickness of the capping layers results in a better optical quality of the QD structures, evidenced by a more intense photoluminescence emission, attributed to the improved QD size homogeneity. Therefore, the enhanced QD absorption seen for cell QD-s-700 is a result of this improvement and seems to be the main contribution to the high efficiency of this cell, as no difference in the absorption between this cell and cell QD700 is observed above 1.42 eV.

Turning our attention to the other trap identified in cell QD630 not related to EL2, trap 2*-630-3. This trap is tentatively attributed to trap M3 which, as already mentioned, is one of the two metastable configurations of a defect identified as a pairing of a native acceptor or defect complex (e^-) and a shallow donor (d^+) [(51), (53)]. The most probable shallow donor within the active region of the cell is silicon, which has been used for doping the InAs QDs layers. If trap 2*-630-3 really corresponds to M3, it means that part of the silicon is diffused into the GaAs capping layers and GaAs spacers layers, where the defect is formed. On the other hand, we do not know the possible origin of the native acceptor or defect complex. The EL2 defect complex is

ruled out because it acts as a donor.

The possible presence of trap M3 in the active region of cell QD630 is thus an interesting fact because it would derive from the QD doping and would prove the diffusion of silicon to the GaAs layers between the QD layers. This trap was not detected in cells QD700 and QD-s-700, despite the diffusion of silicon being expected to increase at higher temperatures. A possible explanation for this result is the probable decrease of the acceptor/complex concentration in the GaAs layers at 700 °C, reducing in this way the probability of formation of centers M3.

However, additional studies on trap 2*-630-3 are necessary to prove if it effectively corresponds to trap M3. Then, its metastable state and dependence on the electric field according to the Frenkel-Poole model must be confirmed.

An important result is noticed when the hole traps detected in cell QD630 (figure 4.5.(c)) are compared to the hole traps detected in cell SC630 (figure 4.4.(f)). According to the discussion of the last section, the hole traps in the active region of cell SC630 correspond to the hole traps in the active region of cell QD630 whose formation is not due to the QD growth conditions. The EL2 defect was detected in both cells but traps 4*630-0.25 and 4-630-0.5 were only detected in cell QD630. This result evidences that the formation of traps 4*630-0.25 and 4-630-0.5 are exclusively induced by the growth conditions of the QDs.

Defects may result from strain fields around the QD layers that extend into the surrounding GaAs layers. These strain fields, as already mentioned, are typical of GaAs/InAs QDs systems and, in consequence, plastic relaxation can take place inducing dislocations and stacking faults which act as carrier traps or recombination centers [(67), (68)]. In consideration, traps 4*630-0.25 and 4-630-0.5 could be related to any of these types of defects.

Since cells QD700 and QD-s700 have structures very similar to that of cell QD630, most likely the small hole injection, explained in figure 4.8.(a), also takes places in the active regions of these cells. Therefore, it should be possible to detect hole traps, if present, as in the case of cell QD630. Based on this assumption, we infer that the defects related to traps 4*630-0.25 and 4-630-0.5 are removed or their concentrations are appreciably reduced with the increase in the growth temperature of the spacer layers to 700 °C, as no traps with similar signatures were detected in cells QD700 and QD-s700.

To finalize the discussion about the DLTS results of IB solar cells, we will talk about how convenient it has been to use *p-i-n* solar cell structures to detect defects in the active regions by DLTS. As confirmed by figure 4.1 in section 4.1, the depletions yielded within the experimental reverse voltage

ranges ($V_r < -1$ V for QD-s-700 and $V_r < -0.25$ V for QD630 and QD700) have been wide enough to cover large portions of the active regions of the cells. These conditions have allowed the detection of a good part of the defects present and the determination of the respective average concentrations to a good approximation. However, the positions of the defects within the active regions could not be determined. It is solely possible in Schottky diodes for which the depletion is gradually extended with the reverse voltage.

If the trap positions were known as in Schottky diodes, it would have been possible to determine if the traps are uniformly concentrated on the GaAs layers, or if, for example, they are concentrated mainly over the p or n -sides or over the interfaces between the QD layers and the GaAs layers. Traps close to these interfaces would be a direct indication of the negative effect of the growth conditions of the QDs on the active regions. On the other hand, traps close to the p and n sides could increase the electrical resistance over the interfaces of these sides and reduce the current collected through the p and n -sides during the operation of the solar cells.

A one-sided $p^+ - n$ diode version of each one of our IB solar cells could be grown and studied by DLTS in the future in order to determine the trap positions and complement the information obtained in this work. The depletion region of a one-sided $p^+ - n$ diode is also gradually extended with the increase of the reverse voltage, as well as in the case of Schottky diodes. Thus, the concentration of the traps could be determined as a function of the depletion depth in this type of structure. Moreover, the depletion is formed over the less doped side n , being this side the target of the study when the diode is measured by DLTS. Then, the most doped side p^+ would be the p -side of the solar cell, while the target side n would be, of course, the respective active region, which is n -doped.

4.4

Summary

In this chapter, the DLTS and Laplace DLTS measurements of the IB solar cells QD630, QD700, and QD-s-700 were presented. A notable difference in the number of traps in the active regions of the cells was observed. Cell QD630, with the lowest growth temperature of the spacer layers (630 °C) and thick capping layers of 6 nm, shows many traps, most of which could not be identified. The formation of these traps, except trap EL2, is apparently inhibited at the highest spacer layers-growth temperature (700 °C) since they were not detected in the active regions of cells QD700 and QD-s-700. Meanwhile, the EL2 concentration is decreased for this same growth

temperature. These results coincide with the high efficiencies of cells QD700 and QD-s-700.

The spectra of the solar cells without QDs by DLTS and Laplace DLTS, cells SC630, SC700, and SCycle, showed the presence of trap EL2 and two unknown traps A and H. We have assumed that these last two traps should be also present in the IB solar cells given the similarity between the structures of these cells and the structures of the cells without QDs. The formation of the three above traps is strictly related to the growth conditions of the spacer layers. However, the growth temperature cycle of the QDs of cells QD700 and QD-s-700 induces the increase of their concentrations. In any case, the spacer layers-growth temperature of 700 °C represents the better growth conditions with the lowest trap concentrations.

Also, it was determined that the formation of a pair of hole traps in the active region of cell QD630 (traps 4*630-0.25 and 4-630-0.5) are due to the growth conditions of the QDs, based on the comparison between the DLTS spectra of this cell and the DLTS spectrum of cell SC630. The misfit strain that extends from the top of the QDs into the surrounding GaAs layers is among the possible causes of these defects.

Additional studies on individually doped GaAs samples showed that probably there are also traps EL2 in the carbon-doped and silicon doped GaAs layers of the *p* and *n*-sides of the IB solar cells. Besides EL2, an Arsenic antisite-related defect ($(As_{Ga})^{++}$) and an unknown trap E were also detected in the carbon-doped GaAs samples, while another unknown trap C was also detected in one of the silicon-doped GaAs samples. These last traps are probably also present in the *p* and *n*-sides and are closely related to the growth temperatures of the GaAs layers of the cells.

5 Photoluminescence results

In this chapter, the photoluminescence (PL) spectra of the samples as a function of temperature and excitation laser power, as well as the subsequent spectra analysis, will be presented. The PL spectra and the identification of the PL emissions are presented in the first section, while a discussion of the PL results is presented in the second section.

The measured samples are the three solar cells without quantum dots (SC630, SC700 and SCycle), the three solar cells with quantum dots (QD630, QD700 and QD-s-700) and the two individually doped GaAs samples p570 and n630. All the samples were measured as grown, without any processing, being exposed directly to the laser beam with the substrate at the opposite side. In the case of the solar cells, the *p*-sides were directly exposed to the laser beam, whereas the *i*-sides (active regions) and *n*-sides were optically excited by light transmitted and not absorbed by the *p*-sides or by light absorbed in the *p*-side and isotropically re-emitted.

The PL spectra obtained as a function of temperature were measured at a fixed laser power of 50 mW, whereas the spectra obtained as a function of laser power were measured at 20 K. The measurements were made within the energy range of 1.0 eV to 1.60 eV. The intensity of emissions were referenced to that of a GaAs sample with a quantum well which exhibits an intense PL peak at room temperature. These referenced peak intensities have been named as PL Intensity/PL max-ref and will appear in the plots corresponding to the peak analysis. Additionally, the spectra were fitted using the Voigt function (71). Usually, the lineshape of PL emissions of GaAs samples are found to be either Gaussian [(72), (31), (73)] or Lorentzian profiles [(74), (75)]. The Voigt function is a convolution of these two profiles, so we considered this function appropriate to fit our spectra in case the lineshapes have one of the above profiles or result from the contribution of both profiles.

The emission peaks emerged on the PL spectra have been analyzed in order to determine their nature. The analysis follows the theory and analysis methods described in sections 3.5.1 and 3.5.2. Three parameters have been obtained from the Voigt fit of each peak: the PL intensity, more precisely, PL Intensity/PL max-ref, the energy position (also called as center) and the full

width at a half maximum (FWHM). The fitted parameters as a function of temperature have been included in the following plots:

- (I) Natural logarithm of PL Intensity/PL max-ref as a function of the inverse of temperature
- (II) Center as a function of temperature
- (III) FWHM as a function of temperature

The thermal activation energies of some emissions were calculated from the slope of plot (I), following the relation between the PL intensity and the inverse of temperature described by equation 3-20.

Similarly, the fitted parameters as a function of laser power have been included in the following plots:

- (IV) the logarithm of PL Intensity/PL max-ref as a function of the logarithm of laser power
- (V) Center as a function of laser power
- (VI) FWHM as a function of laser power

Some type of emissions were inferred based on the constant k , calculated from the slope of plot (IV), following the relations fixed between the PL intensity and the laser power described by equation 3-21.

In addition, the error ranges of the PL intensity, energy position and FWHM of each PL peak were calculated based on the degree of fit of the Voigt function to the experimental data. These error ranges are included in plots (I)-(VI), but most of them are not visible since they are as large as the symbols that represent the peak parameters.

The emissions corresponding to the band-to-band recombinations of the GaInP and AlGaAs layers of the solar cells were not observed on the PL spectra because the energy gap of these materials are higher than 1.6 eV for temperatures between 20 K and 290 K. Such emission energies lie outside of the energy range of the measurements. Moreover, we are only interested in the deep level defects and impurities of the solar cells which have energy levels lying within the band gaps of the materials that constitute the cells. Therefore, the emission energies from defects are expected to be lower than the band-to-band emission energies from the materials. For this reason, we defined the maximum of the PL energy range at 1.60 eV. The minimum of the PL energy range was defined at 1.0 eV in order to obtain reliable measurements with the available optical elements.

In the next section, the spectra of the samples and the respective analysis will be shown. Plots (I)-(VI) are on similar scales to allow the comparison between them.

5.1

Measured PL spectra and identification of the emission peaks

5.1.1

Sample p570

The PL spectra of sample p570 as a function of temperature are seen in figure 5.1, while the spectra as a function of laser power are shown in figure 5.2. Two overlapped peaks K and L have been fitted on these spectra, which are centered at 1.478 eV and at 1.495 eV for 20 K, respectively. No emission is observed below 1.4 eV. The fitted parameters of peaks K and L as a function of temperature and as a function of laser power are seen in figure 5.3. Neither peak K nor peak L corresponds to the emission from the band-to-band recombination, because their centers do not coincide with the GaAs energy gap of 1.52 eV at low temperature and of 1.42 eV at room temperature. In fact, the center Vs. temperature curves in figure 5.3.(3) have been fitted with the Varshni formula, equation 3-11. The resulting parameters $a = 0.11 \text{ eV/K}$ and $b = 9.2 \times 10^4 \text{ K}$ for peak K and $a = 1.53 \times 10^{-3} \text{ eV/K}$ and $b = 1.7 \times 10^3 \text{ K}$ for peak L are very different from the values found in the literature for GaAs samples, which are $a \approx 5 \times 10^{-4} \text{ eV/K}$ and $b \approx 2 \times 10^2 \text{ K}$ [(76), (77)].

Since the sample p570 has been doped with carbon, one of the two PL peaks probably corresponds to the conduction band-to-acceptor (A^0, e) recombination involving the carbon acceptor C_{As} (the carbon in an Arsenic site). Such PL emission has been reported with center about 1.495 eV [(16), (78)], since the C_{As} acceptor has a well-known ionization energy of about 20 meV in GaAs (79). In fact, the energy position of peak L is nearby, and the activation energy calculated for this emission, seen in table 5.1, is 29 meV. We believe, therefore, that peak L corresponds to the conduction band-to- C_{As} acceptor recombination.

Peak K corresponds to an emission of lower energy, therefore, there are only two possibilities: (1) peak K corresponds to a donor-acceptor ($D - A$) recombination, (2) peak K corresponds to another conduction band-to-acceptor recombination in which the acceptor energy level is above the C_{As} level, i.e., above 29 meV from the valence band. Figures 5.3.(4) and (6) show that the center and the FWHM of peak K do not vary with the laser power increase, so the possibility (1) is ruled out. Therefore, there is a probable second type of acceptor in sample p570 with an ionization energy equal to the activation energy of the emission of 52 meV.

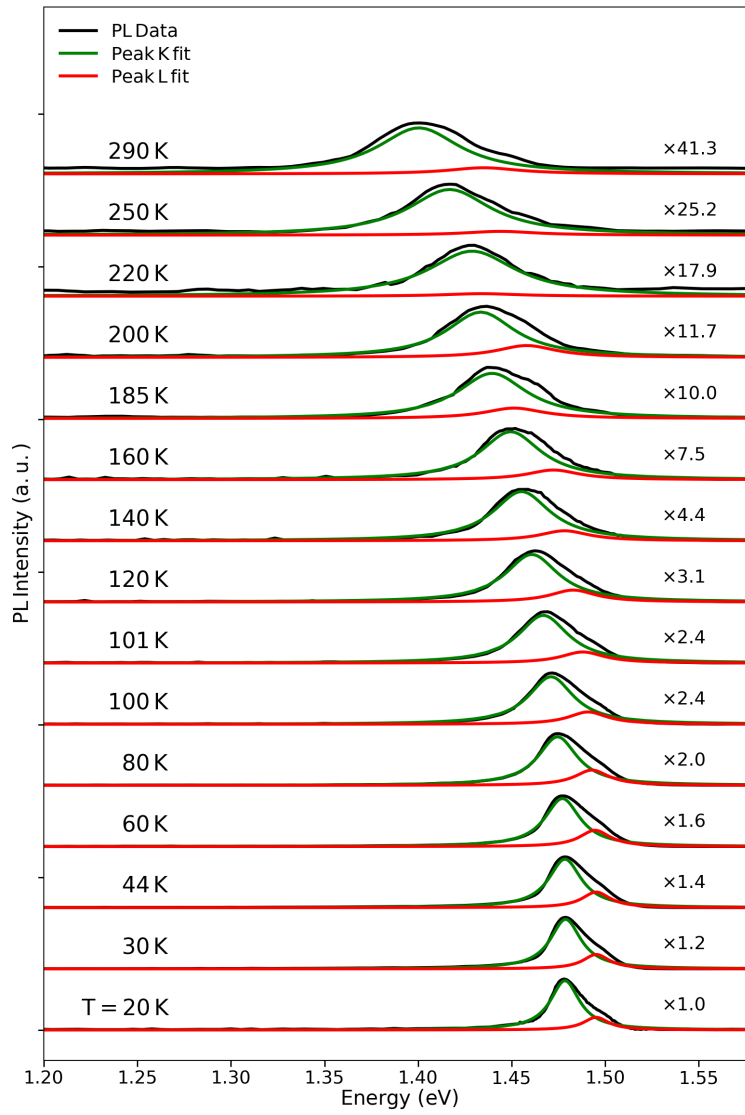


Figure 5.1: Photoluminescence spectra of sample p570 at 50 mW as a function of temperature.

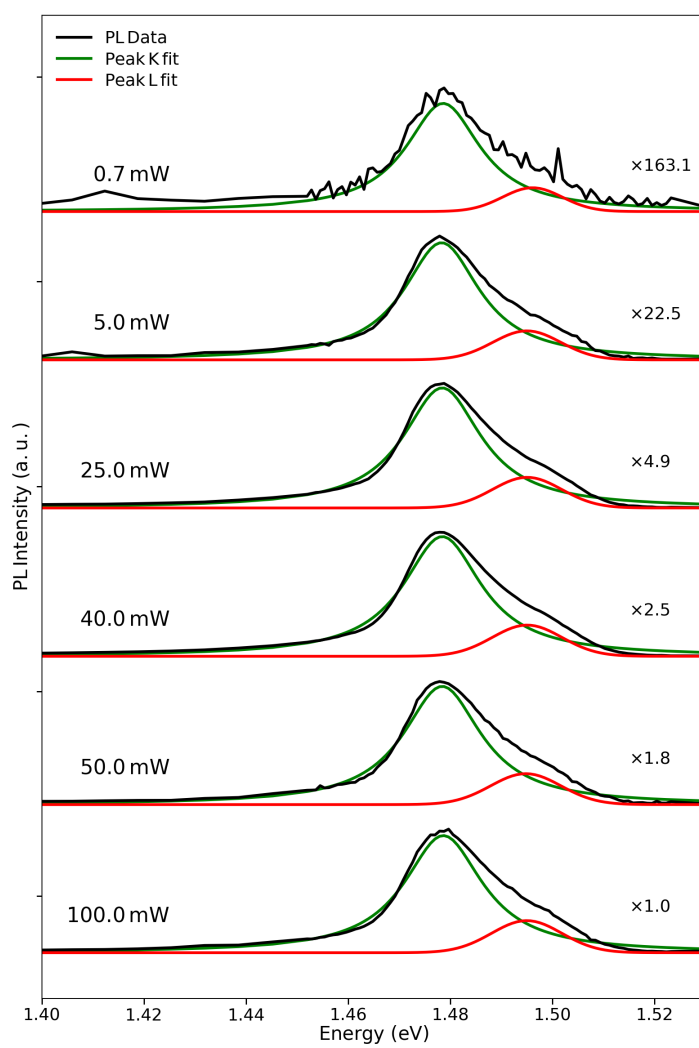


Figure 5.2: Photoluminescence spectra of sample p570 at 20 K as a function of laser power.

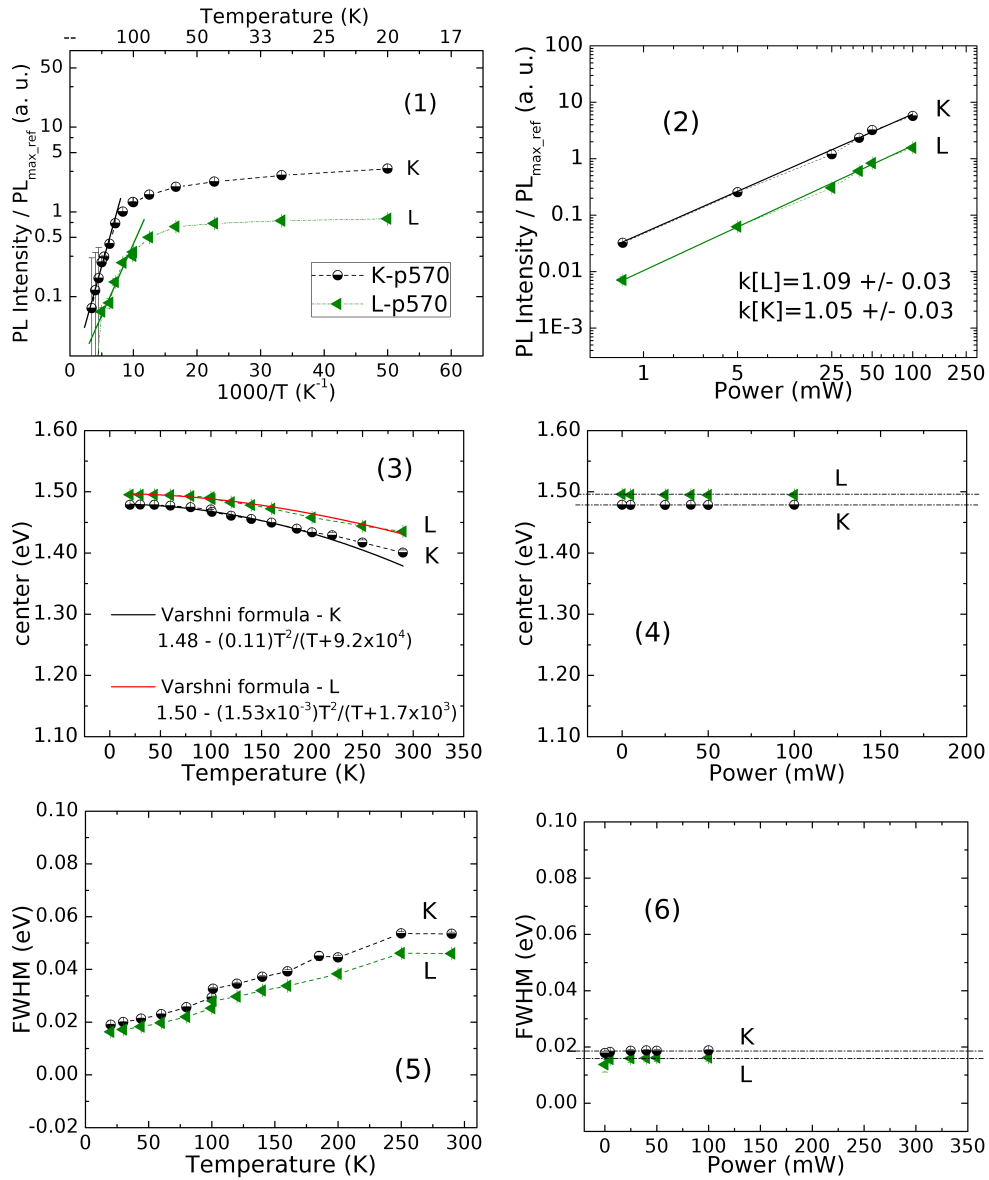


Figure 5.3: Plots corresponding to the analysis of emissions of sample p570. The fitted peak parameters (PL Intensity, center and FWHM) are plotted as a function of temperature (left) and as a function of laser power (right).

Peak	E_a	error
K	52 meV	3 meV
L	29 meV	3 meV

Table 5.1: Thermal activation energies E_a of emissions K and L of sample p570

We have not found acceptors in GaAs reported in the literature with similar ionization energy. Thus, it is just possible to affirm that a second type of acceptor impurity has been incorporated into sample p570 besides the carbon dopant. Furthermore, given the relatively higher intensity of peak K in comparison to peak L, we infer that the concentration of the unknown acceptor in the sample is higher than the carbon doping concentration.

The values of constant k (equation 3-21) calculated for peaks K and L, seen in figure 5.3.(2), are about 1, that is, the increase in intensity of both peaks is almost linear with the increase in laser power, in contrast to the constant $k < 1$ for (A^0, e) recombinations established in section 3.5.2. A valid explanation for this linear increase is that within the excitation power range used in our experiments, no saturation is observed due to the high concentrations of both acceptors.

On the other hand, the possibility of peaks K and L being emissions from excitons bound to carbon acceptors is ruled out: from equation 3-18, the transition energies of excitons bound to ionized and neutral carbons close to 0 K are 1.485 eV and 1.5142 eV, respectively. As all the emissions from shallow impurities have to follow the gap narrowing while increasing temperature, the above values have to decrease about 1 meV for 20 K, equal to the decrease in energy gap from 0 K to 20 K. However, the transition energies of the carbon-bound excitons do not coincide with the energy positions of peaks K and L (1.478 eV and 1.495 eV, respectively) at 20 K.

A scheme of the recombination processes that give rise to the emissions of peaks K and L are shown in figure 5.4.

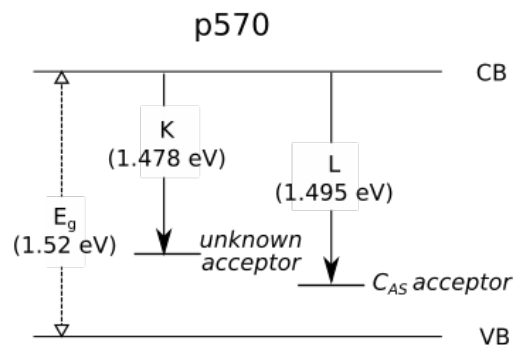


Figure 5.4: Scheme of the conduction band-to-acceptor recombinations giving rise to emissions K and L at 20 K.

5.1.2 Sample n630

The PL spectra of sample n630 as a function of temperature is seen in figure 5.5.(a), while the spectra as a function of laser power is shown in figure 5.5.(b). Five peaks can be observed on these spectra. These peaks have been named as α , β , θ , γ , and ε , and are centered about 1.15 eV, 1.34 eV, 1.46 eV, 1.50 eV, and 1.52 eV at 20 K, respectively. The fitted parameters of these peaks as a function of temperature and as a function of laser power are seen in figure 5.6.

The most intense peak ε clearly corresponds to the band-to-band recombination. As can be observed from figure 5.6.(3), the center of the peak coincides with the GaAs energy gap within the temperature range of measurement: the peak centers begin at 1.52 eV for 20 K and shifts to 1.42 eV as the temperature approaches room temperature. Additionally, the Varshni formula of equation 3-11 was used to fit the curve of the center of peak ε as a function of temperature. The resulting parameters $a = 4.67 \times 10^{-4} \text{ eV/K}$ and $b = 139K$ are in good agreement with the parameters reported in the literature for band-to-band transitions in GaAs layers, which are about $5 \times 10^{-4} \text{ eV/K}$ and $2 \times 10^2 \text{ K}$, respectively [(76),(77)].

The second highest peak γ has its central energy position near the central energy position of peak L of sample p570 at 20 K and 50 mW of optical excitation, as observed from figure 5.7. Moreover, the FWHM of both peaks is almost equal, about 15 meV at 20 K, as can be observed from plots (5) and (6) of figures 5.3 and 5.6. The difference between the energy position of peak ε and the energy position of peak γ at 20 K is about 20 meV, meaning that the energy level of the possible shallow impurity related to peak γ is about 20 meV below the conduction band edge or above the valence band edge. Such level is of the order of acceptor levels. In addition, the constant k of peak γ is lower than one, (see plot (2) of figure 5.6), as expected for transitions through shallow impurities which saturate at high laser power.

The above characteristics can be attributed to either radiative recombinations via carbon or silicon acceptor impurities since the energy levels of these acceptors are in the range of [19-26] meV above the GaAs valence band edge (79). Carbon acceptor can be incorporated into sample n630 as a residual impurity due to the use of the TMGa precursor for MOVPE growth, as explained in section 2.1. In fact, the carrier concentrations of undoped GaAs samples previously grown in our laboratory by MOVPE have been measured to be p -type, so most likely these samples were contaminated with carbon during MOVPE growth.

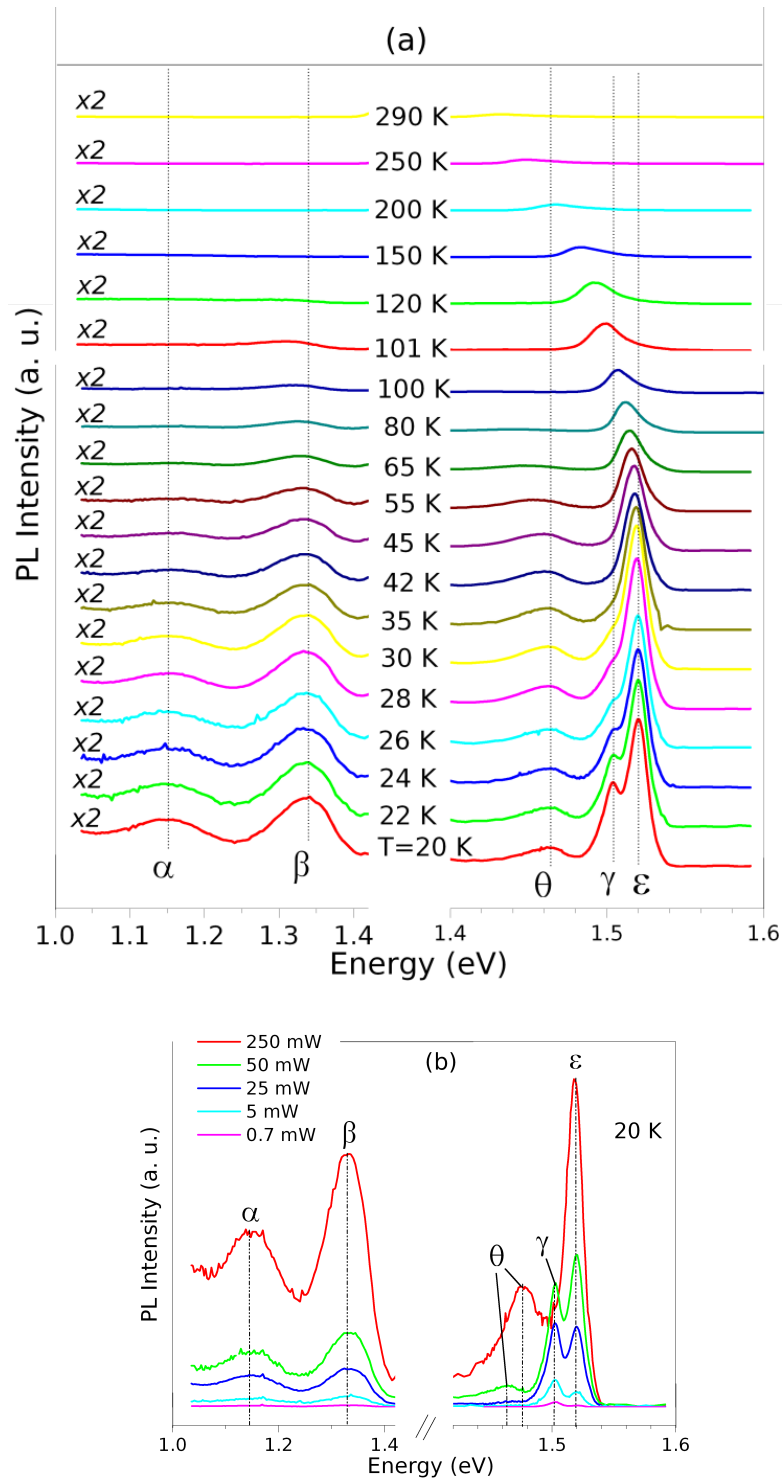


Figure 5.5: ((a) PL spectra of sample n630 at 50 mW as a function of temperature and (b) PL spectra of the same sample at 20 K as a function of laser power. Five emission peaks can be observed, including that one corresponding to the band-to-band recombination, peak ϵ .

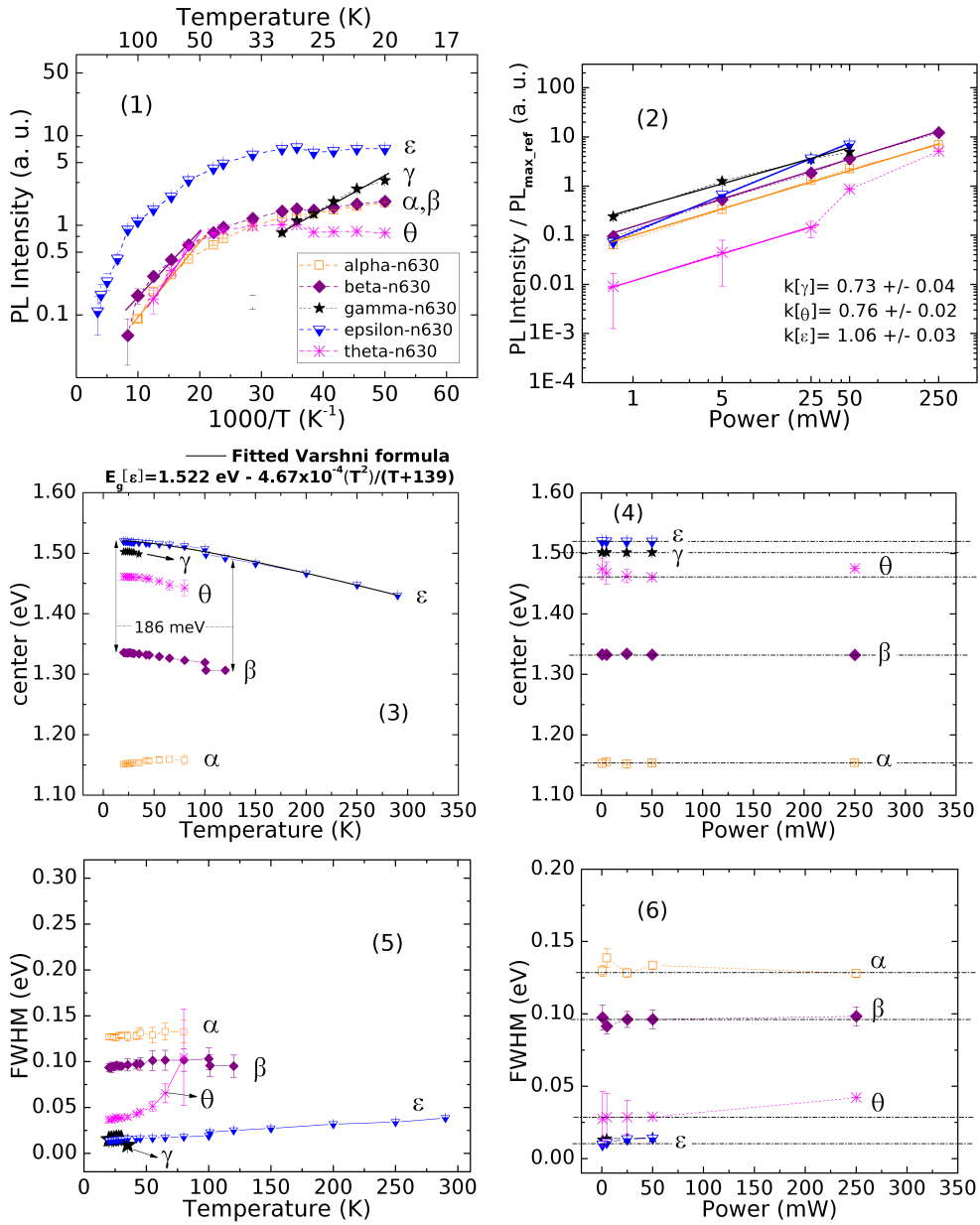


Figure 5.6: Analysis of emission peaks emerged on the PL spectra of sample n630. The peak parameters are plotted as a function of temperature (left) and as a function of laser power (right).

Peak	E_a	error E_a	k	error k
γ	—	—	0.73	0.04
θ	20 meV	1 meV	0.76	0.02
ϵ	—	—	1.06	0.03

Table 5.2: Thermal activation energies E_a and constants k of the emissions of sample n630.

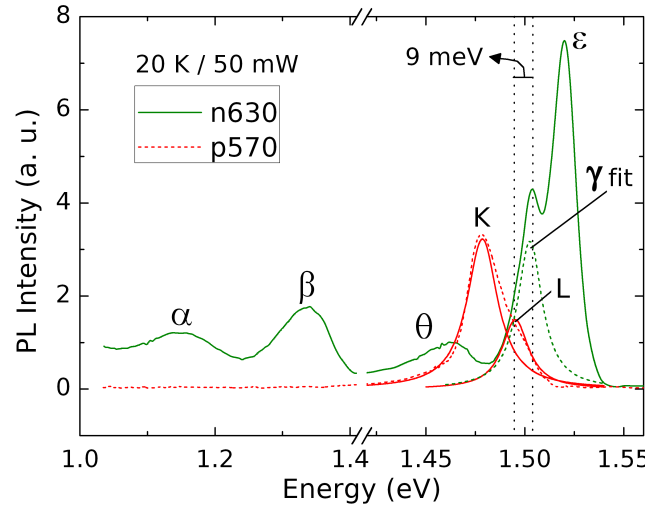


Figure 5.7: Comparison between the PL spectra of samples p570 and n630 at 20 K and 50 mW of laser excitation.

Therefore, it is quite probable that any GaAs sample grown in our MOVPE reactor is carbon-contaminated since the used gas precursors and growth parameters are very similar.

Silicon acceptor Si_{As} (a silicon atom in an Arsenic site) is very likely to be incorporated in sample n630 due to the well-known property of silicon to substitute either Gallium and Arsenic positions in the GaAs lattice for silicon doping concentrations $\geq 1 \times 10^{17} \text{ cm}^{-3}$ (80), which is almost the same doping concentration of sample n630.

Given the probability of incorporation of the two types of acceptors Si_{As} and C_{As} in sample n630, emission γ most likely results from a superposition of two PL peaks related to the conduction band-to- Si_{As} and conduction band-to- C_{As} transitions. This is plausible since the FWHM of peak γ (15 meV at 20 K) is larger than the maximum energy difference between the two transitions ($[26-19]=7$ meV according to (79)).

In relation to peak θ , this peak exhibits a small blue shift (an increase in emission energy) when the laser power is raised to 250 mW, as can be observed from the spectra as a function of laser power, figure 5.5.(b), and in the center Vs. laser power curve, figure 5.6.(4). The FWHM of this peak is also increased, as seen in figure 5.6.(6). The above characteristics are typical of $(D - A)$ recombinations, when the donor-acceptor distant pairs are saturated at high laser powers. Also, the constant k calculated for peak θ is lower than 1, indicating a limited increase of the intensity of emission due to the finite amount of neutral donors and acceptors. Based on the above results, we associate peak θ with $(D - A)$ recombinations.

Since sample n630 is silicon-doped, the silicon donor Si_{Ga} (a silicon atom

in a Gallium side) is the probable donor involved in the emission of peak θ . The involved acceptor can be deduced from the corresponding activation energy E_A calculated using equation 3-14. Putting $\hbar\omega = 1.46$ eV (the center of peak θ at 20 K), E_A is approximately 53 meV¹. This value coincides with the ionization energy of the unknown acceptor involved in emission K (52 meV), which dominates the spectra of sample p570.

As the shallow silicon donor ionizes rapidly at low temperatures, the Si_{Ga} -to-shallow acceptor recombination considered above is rapidly suppressed. However, the emission is gradually replaced by the conduction band-to-shallow acceptor recombination at higher temperatures. This is the reason for the high increase of the FWHM of peak θ seen in figure 5.6.(5), which would result from the overlapping of the two peaks corresponding to both types of recombination.

A scheme of the recombination processes giving rise to the emissions of peaks γ and ε at 20 K are shown in figure 5.8. The two possible transitions for peak θ are also shown: the Si_{Ga} -to-unknown acceptor transition at low temperatures, and the conduction band-to-unknown acceptor transition at higher temperatures.

Concerning the broad peaks α and β , the emission central energies of these peaks of 1.15 eV and 1.34 eV, respectively, are lower than the typical emission energies from recombinations through shallow impurities. We have searched for emissions from deep defects to identify these peaks.

The energy positions and the FWHM of peaks α and β at 20 K are similar to the energy positions and FWHM of low-temperature PL peaks associated with the defect complexes $Si_{Ga} - V_{Ga}$ and $Si_{As} - V_{As}$, respectively.

¹the term $e^2/(K\varepsilon_0 r)$ in equation 3-14 is about 1 meV ((30))

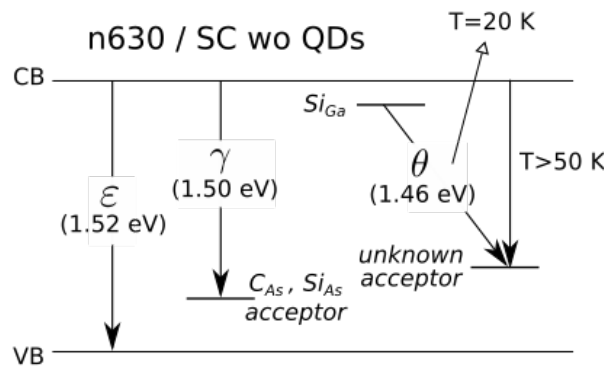


Figure 5.8: Scheme of the recombination processes attributed to peaks γ , ε and θ of sample n630 at 20 K. At the right-side is also shown the recombination giving rise to peak θ at higher temperatures. The two transitions at the left-side also accounts for peaks ε_i and γ_i of the spectra of solar cells without QDs.

These complexes result from Coulombic attraction between silicon donors or silicon acceptors and Gallium or Arsenic vacancies (V_{Ga} and V_{As}) in the GaAs crystal lattice, which act as deep acceptors and deep donors, respectively. The Coulombic attraction gives rise to the formation of localized donor–acceptor pairs, which acts as stationary molecules. The corresponding PL emissions have been considered as resulting from internal transitions of electrons between the excited and ground states of the complexes. The energy levels of such states, therefore, can not be represented by a discrete energy level within the GaAs band gap.

The peaks associated with the $Si_{Ga} - V_{Ga}$ complex have been reported at 1.14 eV (81), 1.18 eV (32), and at 1.23 eV (31), near the energy position of peak α of 1.15 eV at 20 K (see figures 5.6.(3) and (4)). In reference (31), the FWHM of the peak is 110 meV, whereas the FWHM of peak α is about 127 meV at 20 K (see figures 5.6.(5) and (6)). The peaks associated with $Si_{As} - V_{As}$ complex were reported between 1.35 eV and 1.37 eV [(31), (73)], very close to the energy position of peak β at 1.34 eV for 20 K. The FWHM of 105 meV reported in (31) is very close to the FWHM of peak β of 94 meV.

Based on the above similarities, we associate peaks α and β with emissions from the $Si_{Ga} - V_{Ga}$ and $Si_{As} - V_{As}$ defect complexes, respectively. Moreover, emission β also confirms the incorporation of silicon acceptors in sample n630, which is the base to assume that an intensity fraction of emission γ corresponds to the conduction band-to- Si_{As} transition.

5.1.3

Solar cells without QDs, samples SC630, SC700, and SCycle

The PL spectra of solar cells without QDs as a function of temperature are seen in figures 5.9.(a), 5.10.(a) and 5.11.(a). The PL spectra of these same cells as a function of laser power are shown in figures 5.9.(b), 5.10.(b) and 5.11.(b). The spectra as a function of temperature, as well as the spectra as a function of laser power, are very similar to each other and are also very similar to the corresponding spectra of sample n630. The spectra at 20 K and 50 mW excitation are plotted together in figure 5.12, in which the similarity between the spectra is evident. The three solar cells without QDs show four emission peaks centered at about 1.14 eV, 1.34 eV, 1.50 eV, and 1.52 eV, which are approximately the same energy positions as the emission peaks α , β , γ and ε of sample n630. Also, the corresponding linewidths seem to be similar. A tiny fifth peak is observed around the same position of peak θ of sample n630, but it could not be studied due to its low resolution.

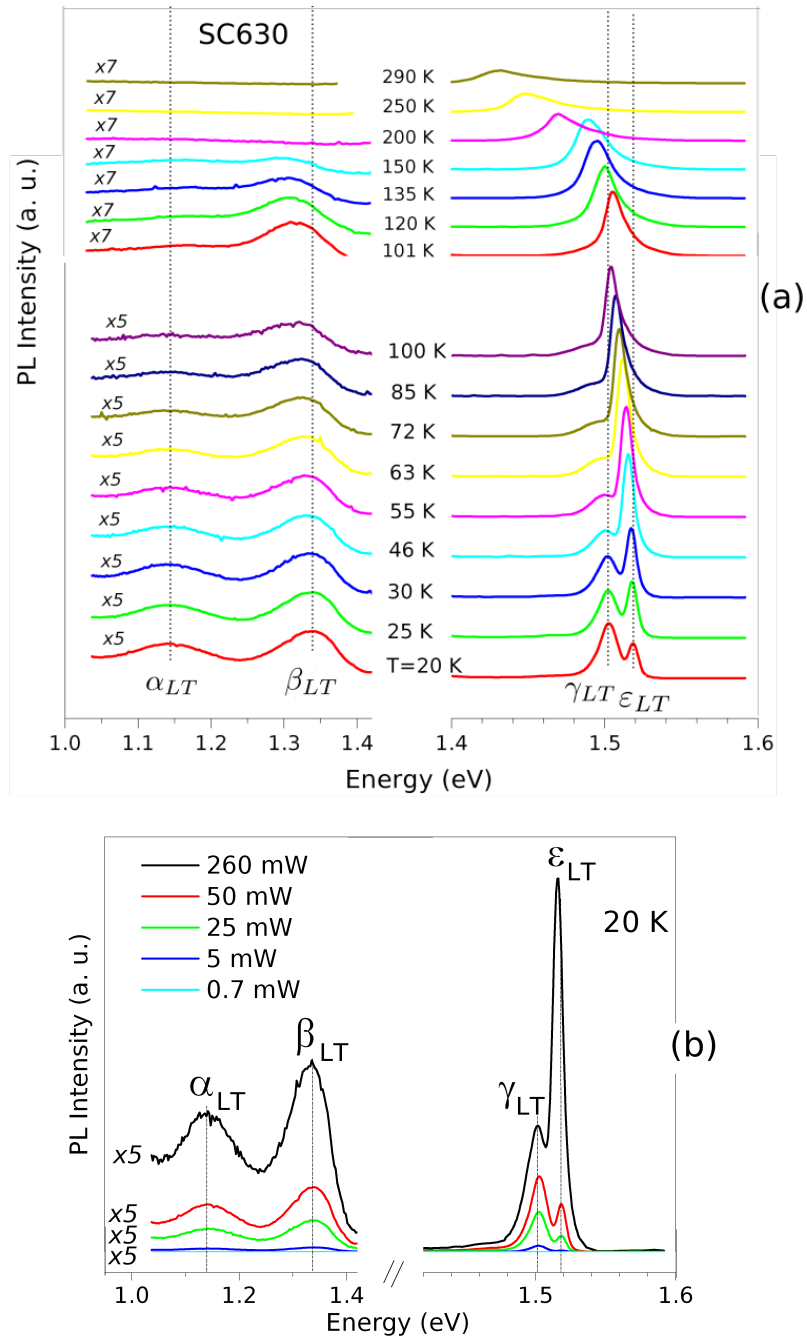


Figure 5.9: (a) PL spectra of solar cell SC630 at 50 mW as a function of temperature and (b) PL spectra of the same cell at 20 K as a function of laser power.

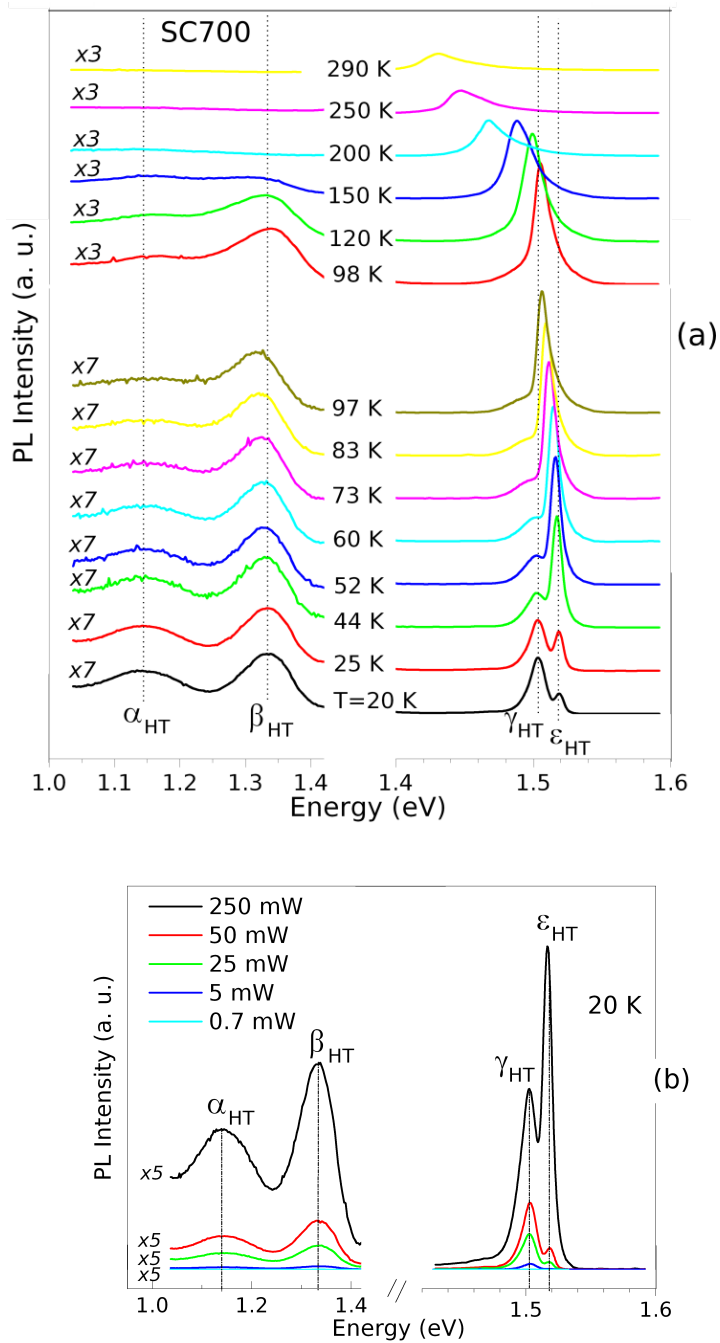


Figure 5.10: (a) PL spectra of solar cell SC700 at 50 mW as a function of temperature and (b) PL spectra of the same cell at 20 K as a function of laser power..

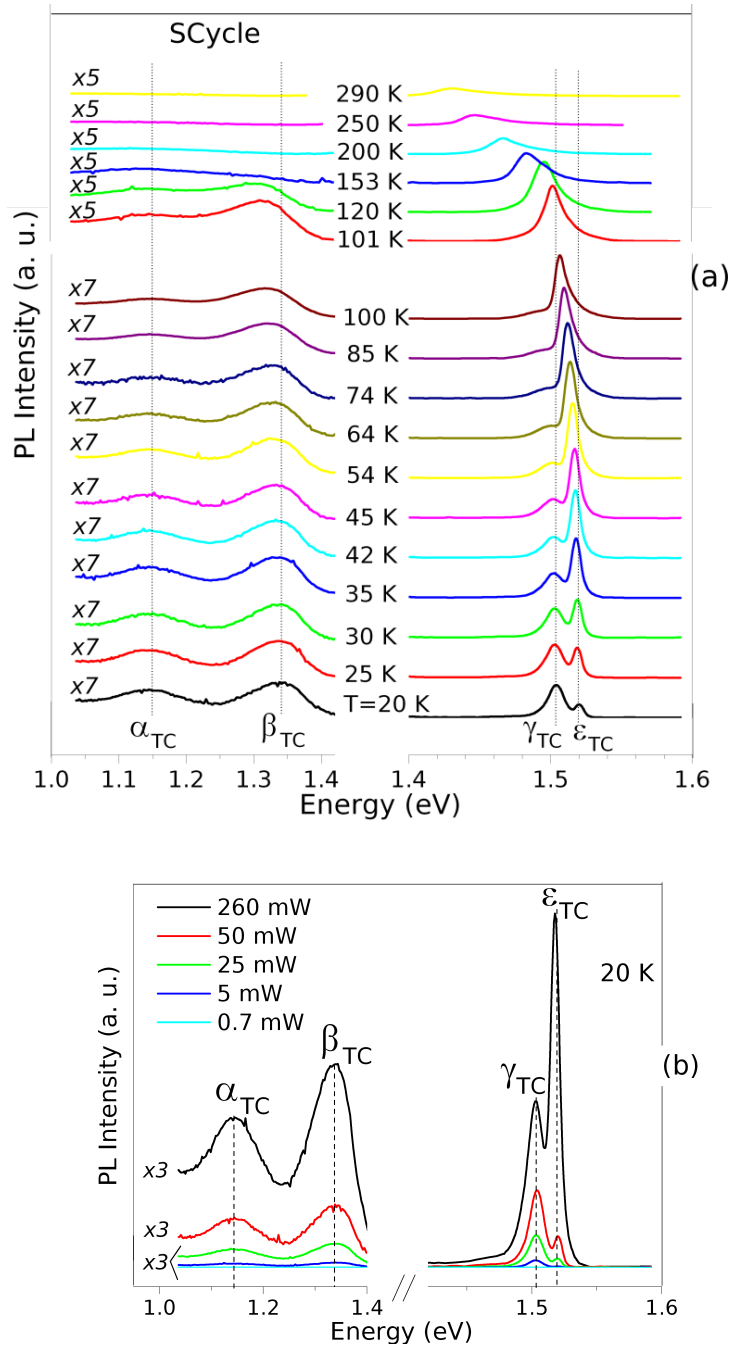


Figure 5.11: (a) PL spectra of solar cell SCycle at 50 mW as a function of temperature and (b) PL spectra of the same cell at 20 K as a function of laser power.

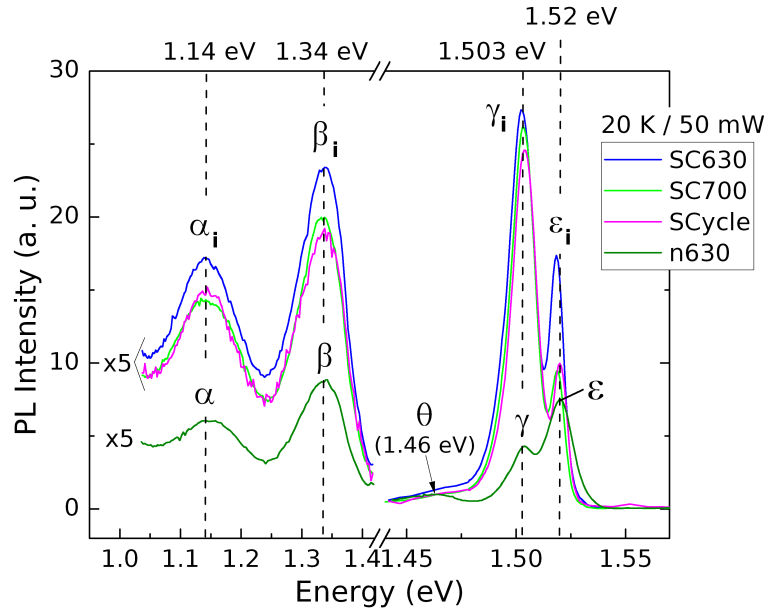


Figure 5.12: Comparison between the PL spectra of the solar cells without QDs and the PL spectrum of sample n630 at 20 K and 50 mW of excitation power.

Based on the similarity with the spectra of sample n630, it is very probable that the emissions of the solar cells without QDs correspond to the same types of recombinations attributed to the emissions of sample n630. In particular, the two emissions at 1.14 eV and 1.34 eV peaks, similar to peaks α and β , most likely correspond to emissions from silicon complexes located in the n -sides of the cells.

As mentioned at the beginning of this chapter, the surfaces of the p -sides of the solar cells were directly exposed to the excitation laser beam. Theoretically, the intensity of the light transmitted across the structure of the solar cells decreases exponentially as $e^{-\alpha z}$ as the light penetrates a distance z from the surface of the p -side, depending on the GaAs absorption coefficient α . Based on this assumption and taking into account the dimensions of the solar cells, the light intensity has been calculated to be essentially zero at the interface between the active region and the n -side of each cell. This calculation rules out the probability of optical excitation of the n -sides and the subsequent luminescence emission. Despite the total absorption of the light along the p -sides and active regions, a reasonable alternative to explain the luminescence of the n -sides observed in this work is that these sides re-absorb part of the photons emitted by recombination within the active region, near the active region/ n -side interfaces. In this way, the n -sides can be optically excited and induce the emissions related to the silicon complexes present in these sides.

The four emission peaks of the solar cells without QDs have been labeled

in a similar way to emission peaks of sample n630: α_i , β_i , γ_i and ε_i , for which the variable i is LT for cell SC630, HT for cell SC700 and TC for cell SCycle. The maximum intensities, FWHM, and centers of these peaks as a function of temperature and laser power are shown in figures 5.13, 5.14 and 5.15. In the following paragraphs, the similarities between the above peaks and the respective peaks of spectra of cell n630 will be shown.

The centers of peaks ε_{LT} (plot 5.13.(3)), ε_{HT} (plot 5.14.(3)), and ε_{TC} (plot 5.15.(3)) were fitted with the Varshni formula, and the resulting parameters $a \approx 5 \times 10^{-4} \text{ eV/K}$ and $b \approx 2 \times 10^2 \text{ K}$ are in good agreement with the values found in the literature for the temperature dependence of the GaAs gap [(76),(77)]. Therefore, peaks ε_{LT} , ε_{HT} , and ε_{TC} , in a similar way to peak ε of sample n630, correspond to band-to-band emissions, probably coming from all the doped and undoped GaAs layers comprising the solar cells.

Peaks γ_{LT} , γ_{HT} , and γ_{TC} , as well as peak γ of sample n630, are rapidly quenched at temperatures below 100 K, inducing the increase of the band-to-band emissions, as observed from the spectra as a function of temperature. Also, the difference between the energy positions of peaks γ_i and ε_i of each cell at 20 K is about 20 meV, which is close to the energy positions of the carbon and silicon acceptors (C_{As} and Si_{As}) above the GaAs valence band edge. The constants k of peaks γ_{LT} , γ_{HT} , and γ_{TC} , shown in table 5.3, are lower than one, in agreement with the characteristics of radiative emissions related to shallow impurities whose intensities at high laser power are limited by the impurity concentrations. Based on these features, peaks γ_{LT} , γ_{HT} , and γ_{TC} can be also attributed to combinations of the two emissions conduction band-to- C_{As} and conduction band-to- Si_{As} like peak γ . The conduction band-to- C_{As} emission most probably has its origin in the carbon-doped layers of the p -sides, while the conduction band-to- Si_{As} emission has its origin in the silicon-doped n -sides. Probably, the carbon-related emission is more intense than the silicon-related emission because the p -side is directly excited by the laser beam while the n -side is though to be excited by the light emitted after radiative recombination in the active region.

The two transitions shown in figure 5.8 for peaks ε and γ also represent the emissions ε_i and γ_i of the solar cells without QDs.

In relation to peaks α_{LT} , α_{HT} , and α_{TC} , their energy central positions of about 1.14 eV, and their FWHM of about [124-140] meV at 20 K, shown in plots (3)-(6) of figures 5.13, 5.14, and 5.15, are similar to the energy position and FWHM of peak α of sample n630, which are 1.15 eV and 127 meV, respectively (see plots (3)-(6) of figure 5.6).

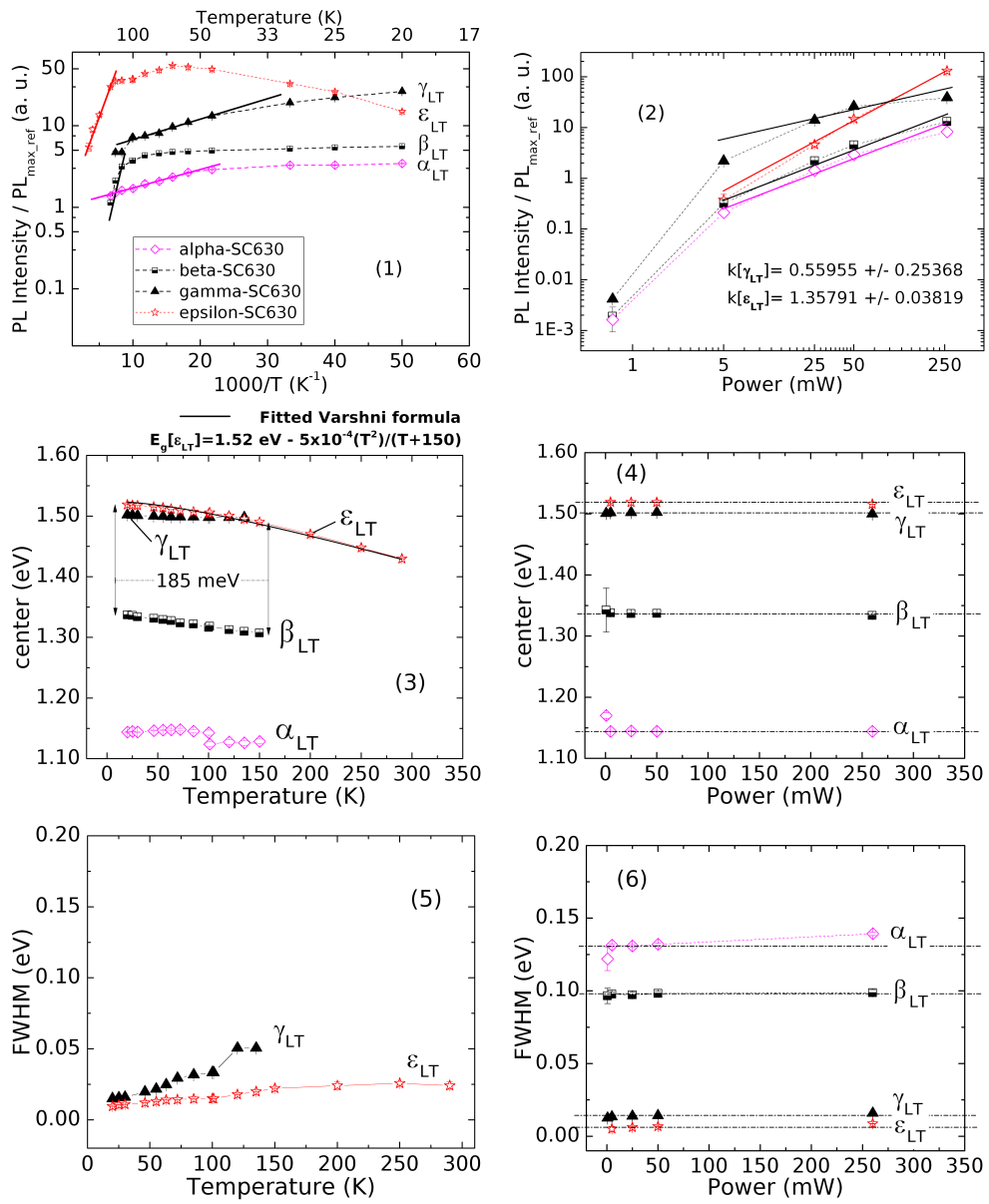


Figure 5.13: Fitted parameters of the emission peaks of sample SC630 plotted as a function of temperature (left) and as a function of laser power (right). Plot (5) only includes the FWHM of peaks γ_{LT} and ϵ_{LT} because the FWHM obtained for peaks α_{LT} and β_{LT} are not reliable.

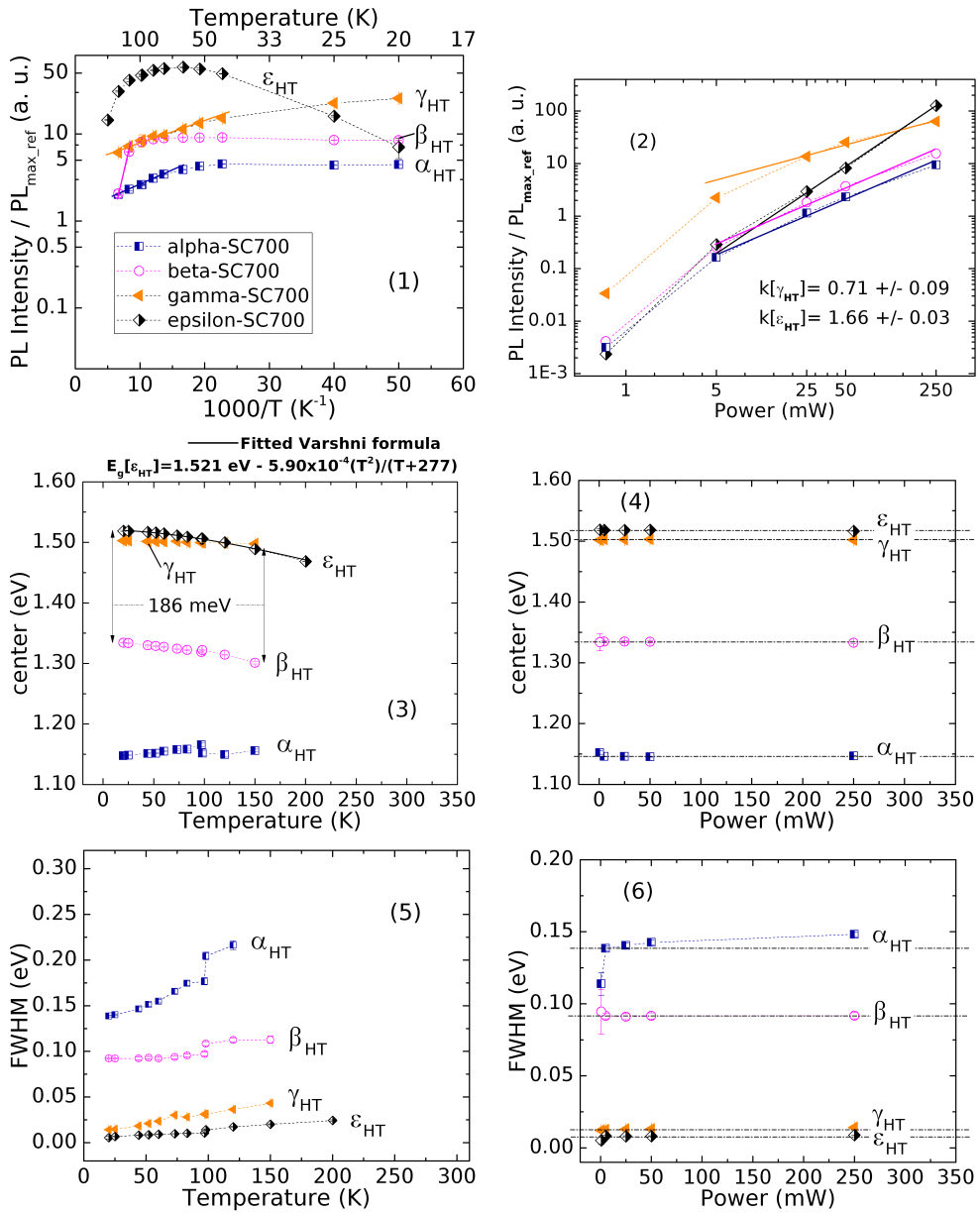


Figure 5.14: Fitted parameters of the PL emissions of sample SC700 plotted as a function of temperature (left) and as a function of laser power (right).

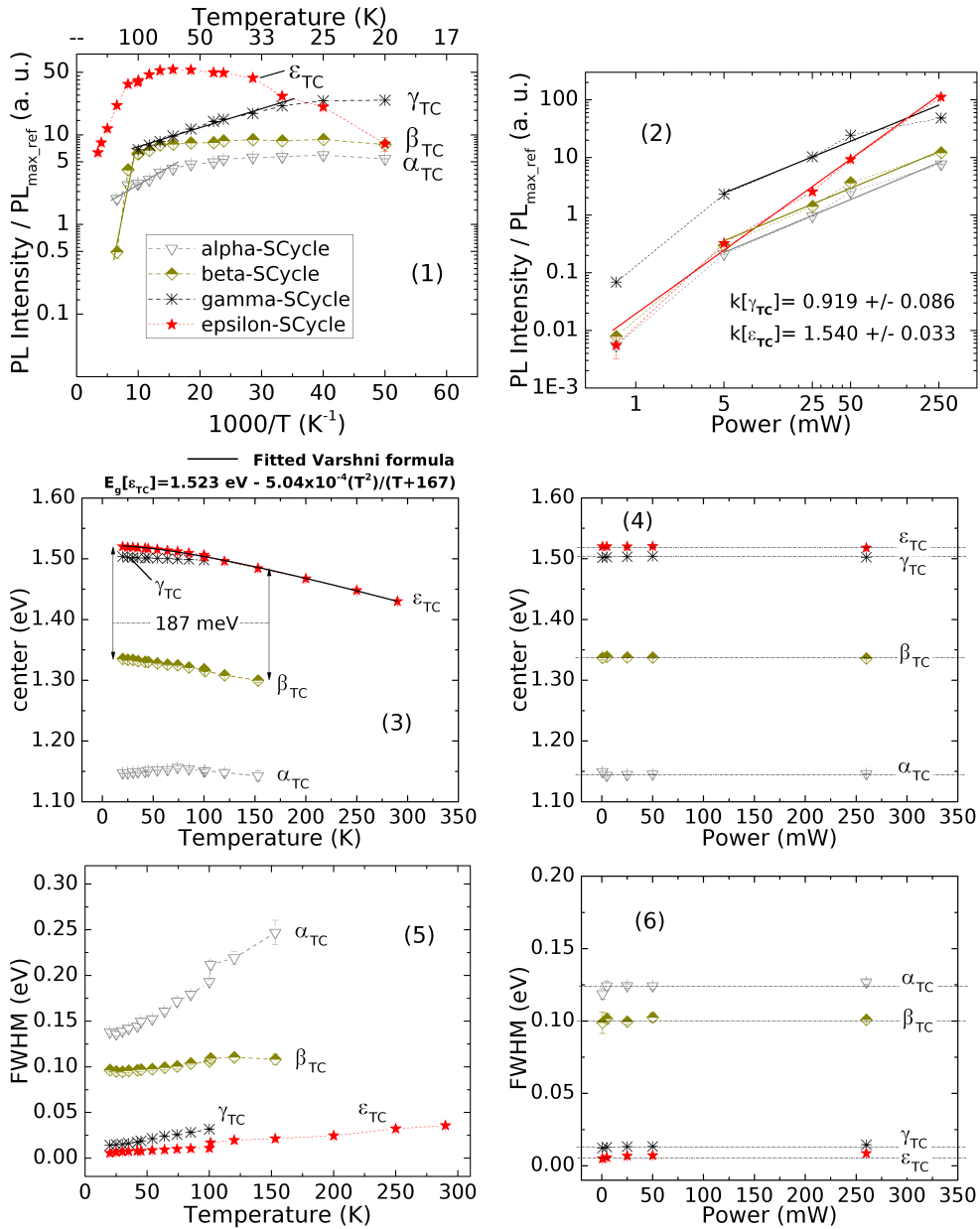


Figure 5.15: Fitted parameters of the PL emissions of sample SCycle as a function of temperature (left) and as a function of laser power (right).

sample	peak	k	error k
SC630	γ_{LT}	0.56	0.25
	ϵ_{LT}	1.36	0.04
SC700	γ_{HT}	0.71	0.09
	ϵ_{HT}	1.66	0.03
SCycle	γ_{TC}	0.92	0.09
	ϵ_{TC}	1.54	0.03

Table 5.3: Constants k of the PL emissions of the solar cells without QDs.

The case of peaks β_{LT} , β_{HT} , β_{TC} , and β of n630 for 20 K is similar: peak β is centered at 1.34 eV and has a FWHM of 94 meV, very similar to peaks β_{LT} , β_{HT} , and β_{TC} , centered about the same energy position, and with a FWHM between 92 meV and 100 meV. Additionally, as can be observed from the spectra as a function of temperature, the centers of peaks α_{LT} , α_{HT} , and α_{TC} , similarly to peak α , remain practically constant with the increase in temperature, while the centers of peaks β_{LT} , β_{HT} , and β_{TC} are red-shifted, in similar way to peak β .

The similarities described above allows us to associate peaks α_i and β_i with the defect complexes $Si_{Ga} - V_{Ga}$ and $Si_{As} - V_{As}$, respectively.

It is worth noting that there are two different regimes of increase for the PL intensities of all the emissions as a function of laser power, as observed in plots 5.13.(2), 5.14.(2), and 5.15.(2). The regime change occurs about 5 mW when the laser power is high enough to induce the saturation of the centers involved in the emissions. Below this laser power, the optical excitation is too low even to induce the band-to-band transition.

5.1.4

IB solar cells, samples QD630, QD700, and QD-s-700

The spectra of the IB solar cells as a function of temperature are shown in figures 5.16, 5.18, and 5.20. The spectra as a function of laser excitation are shown in figures 5.17, 5.19 and 5.21.

In all these spectra, a low peak, centered about 1.50 eV for 20 K, is observed. This peak was named as A_{LT} for cell QD630, A_{HT} for cell QD700, and A_s for QD-s-700. The activation energies corresponding to these peaks, shown in table 5.4, are 27 meV and 28 meV, respectively, very similar to the activation energy of 29 meV calculated for peak L of sample p570 (table 5.1), which was attributed to the conduction band-to- C_{As} transition. Moreover, the constants k of peaks A_i at 20 K, also shown in table 5.4, are lower than 1, in agreement with the saturation of impurities at high laser power. Given the above characteristics, peaks A_i most probably correspond to emissions from conduction band-to- C_{As} originated in the carbon-doped layers of the p -sides.

We rule out the possibility of the conduction band-to- Si_{As} emission be related to peaks A_i because the strong absorption of light by the QDs in the active regions of the IB solar cells limits the re-absorption of light on the n -side. The QDs themselves are able to re-absorb the photon energy emitted via the band-to-band-recombinations in the active region since the carriers confined in the QD energy levels need low energy to jump into the GaAs conduction and valence bands (< 250 meV for electrons at $T=[230-300]$ K according to the

values of table 4.1). Therefore, the incident laser light must be totally absorbed in the p -side and the active region of each IB solar cell.

Other broad PL peaks below 1.45 eV are found in the spectra of the IB solar cells. In the case of cell QD630 (spectra 5.16 and 5.17), the fitting showed two overlapped peaks B_{LT} and C_{LT} centered about 1.26 eV and 1.31 eV at 20 K, respectively. Similarly, two overlapped peaks B_{HT} and C_{HT} were fitted on the spectra of cell QD700 (figures 5.18 and 5.19), which are centered about 1.34 eV and 1.38 eV at 20 K, respectively. The spectra of cell QD-s-700 (figures 5.20 and 5.21) only exhibit a single intense peak B_s centered about 1.375 eV at 20 K.

Previously, low-temperature PL spectra of the same cells QD630, QD700, and QD-s-700 were reported by our laboratory group (21)². The same emission peaks B_{LT} , C_{LT} , B_{HT} , C_{HT} , and B_s were observed, as well as peaks A_{LT} , A_{HT} , and A_s around 1.50 eV. In particular, the peaks centered below 1.45 eV were associated with emissions from the QDs derived from radiative recombinations between electrons and holes confined in the ground and the first excited states of the QDs (this topic was detailed in section 3.5.1). The above assumption was based on simulations that showed that the possible energy ranges of such recombinations are around the emission energies of these peaks.

In this work, we will show more evidence that demonstrates that the peaks below 1.45 eV are related to QD emissions. New simulations based on parameters better adapted to the real characteristics of the QDs have been performed to confirm again that the emission energies of these peaks agree with the energies of the QD transitions. These simulations will be shown later. First, we will review the behavior of the peaks in question as a function of temperature and laser power to confirm the types of transitions to which they are related.

As observed from figure 5.17, peak C_{LT} increases in intensity with increasing the laser power more than peak B_{LT} does. This is better seen in figure 5.23.(a), where the ratio of the intensities of the two peaks is shown. The behavior of peak B_{LT} is consistent with the saturation of the ground state transition (the recombination between electrons and holes in the ground energy levels of a QD), whereas the behavior of peak C_{HT} is in agreement with the filling of the first excited states [(82), (83)].

²In this reference, these cells are labeled as 6-630, 6-700, and 3-700, respectively

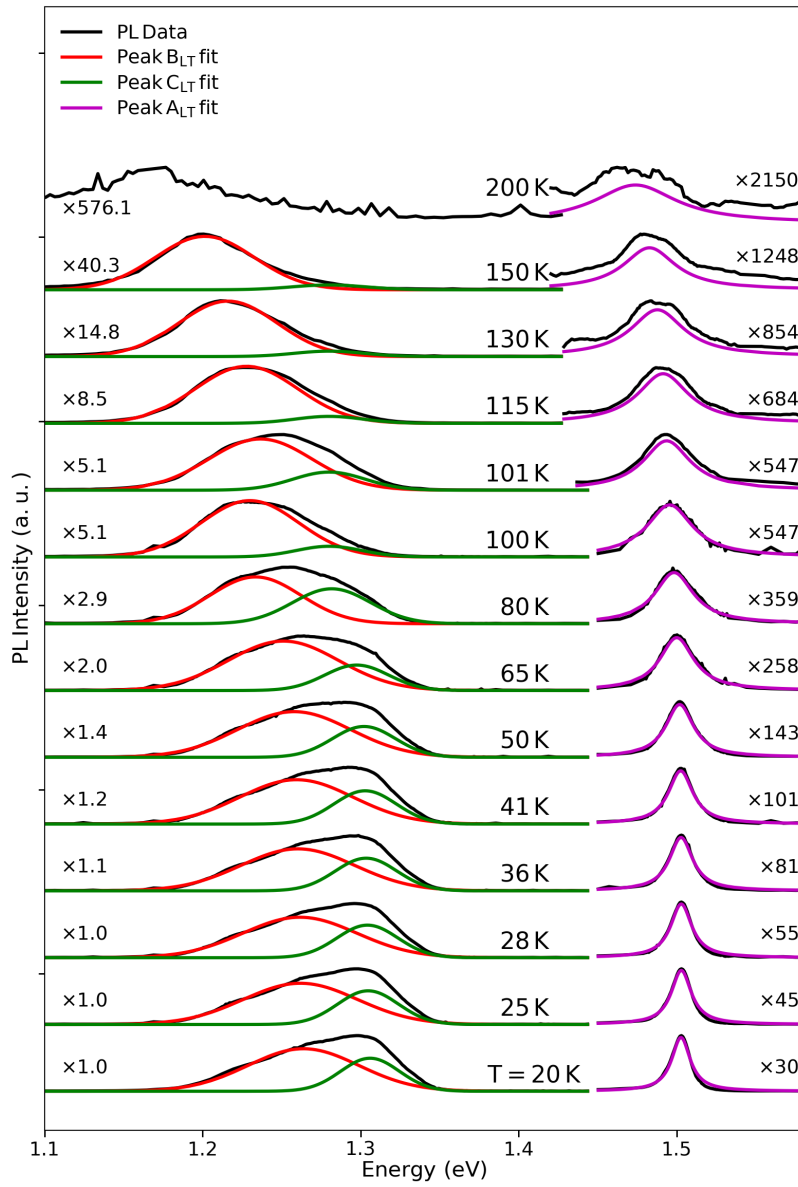


Figure 5.16: PL spectra of solar cell QD630 at 50 mW as a function of temperature.

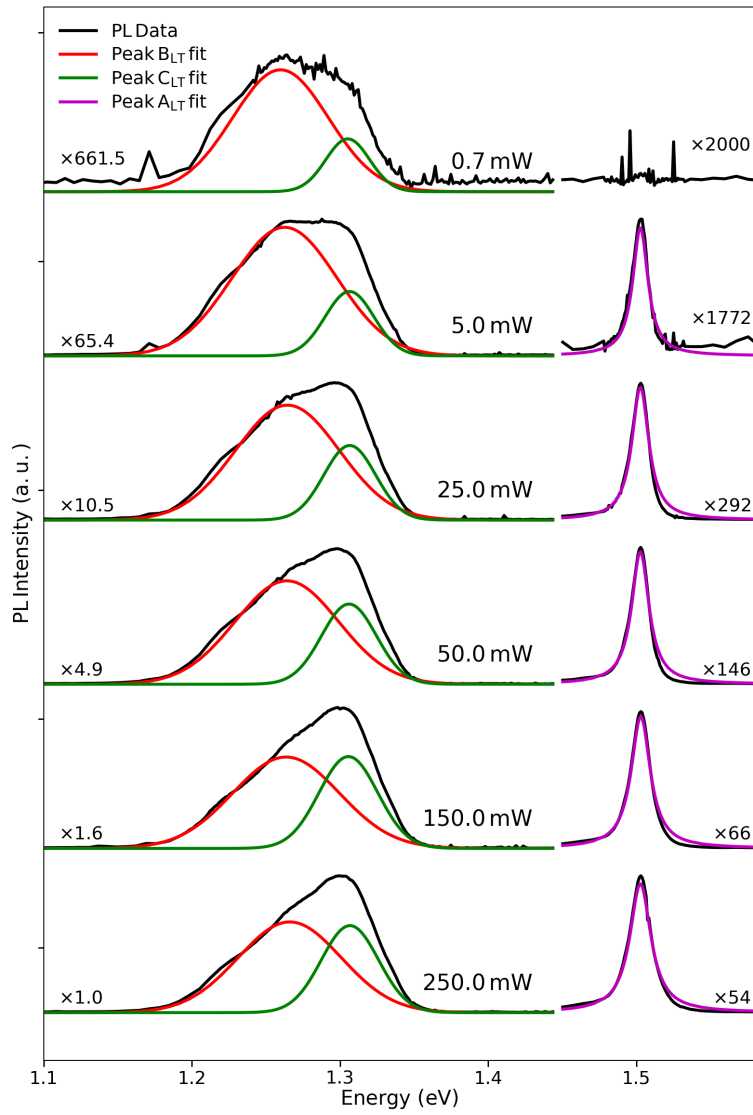


Figure 5.17: PL spectra of solar cell QD630 at 20 K as a function of laser power.

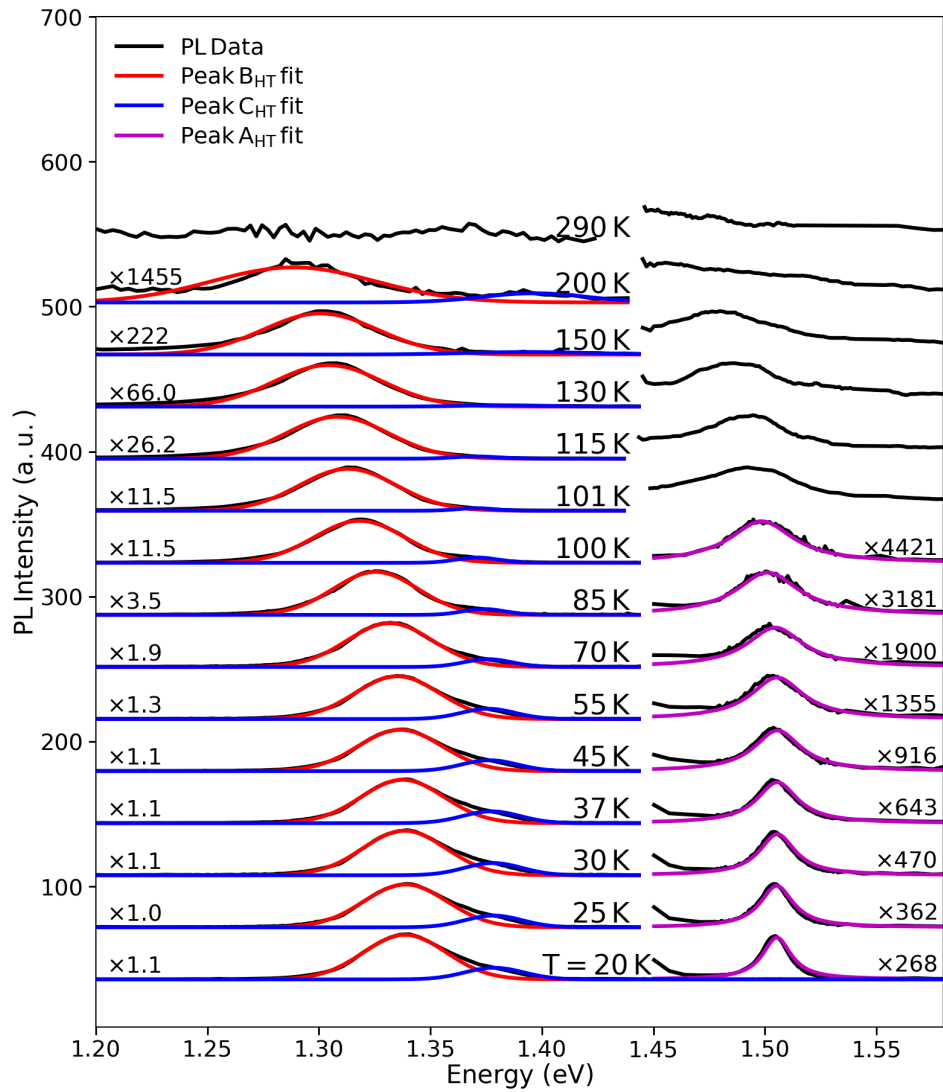


Figure 5.18: PL spectra of solar cell QD700 at 50 mW as a function of temperature.

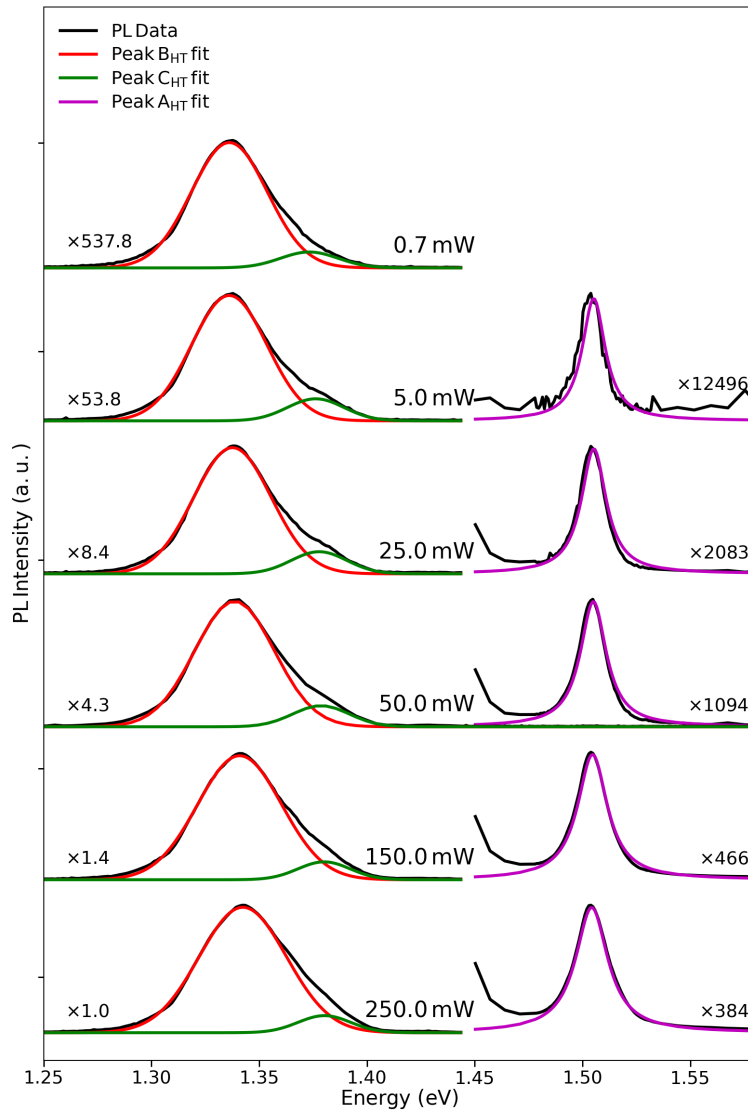


Figure 5.19: PL spectra of solar cell QD700 at 20 K as a function of laser power. The tail at the left of peak A_{HT} corresponds to peak C_{HT} .

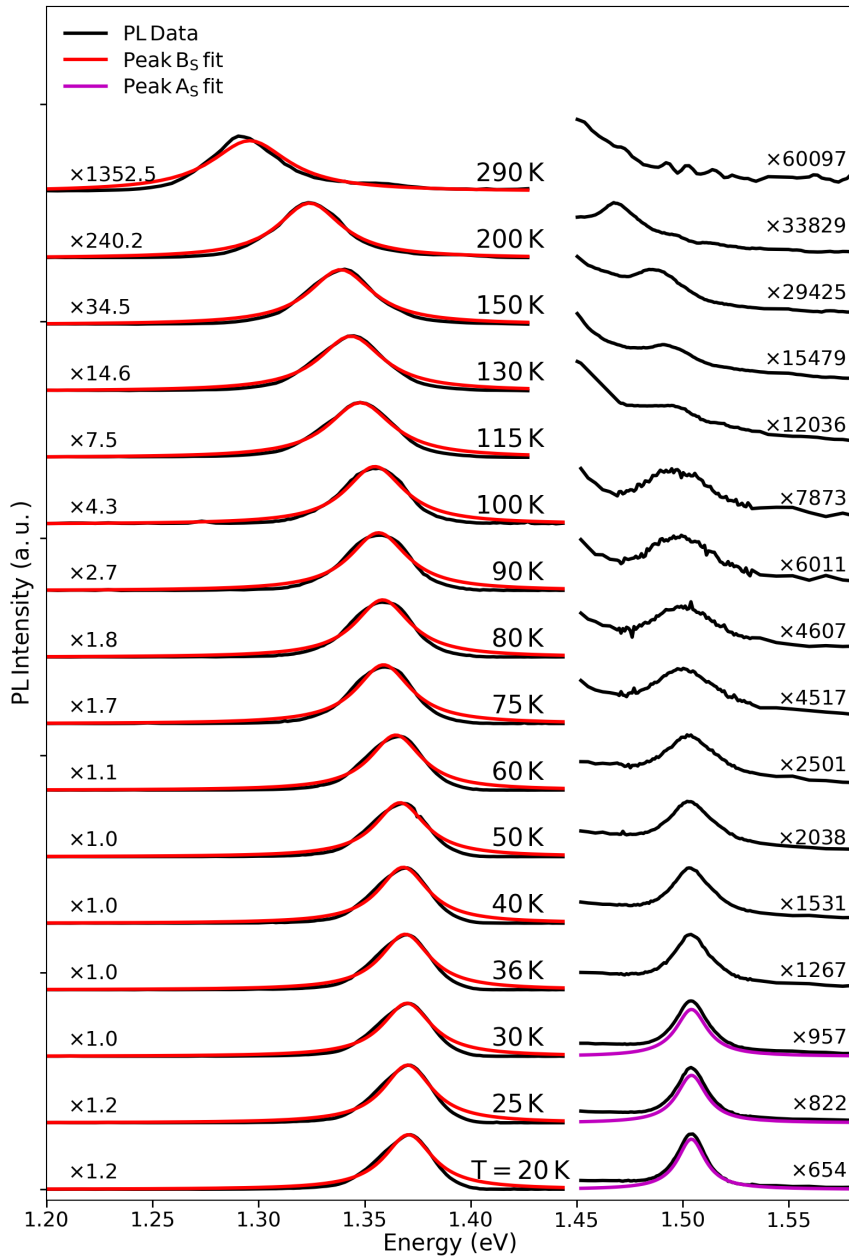


Figure 5.20: PL spectra of solar cell QD-s-700 at 50 mW as a function of temperature. The tail seen at the left of peak A_s above 75 K corresponds to peak B_s .

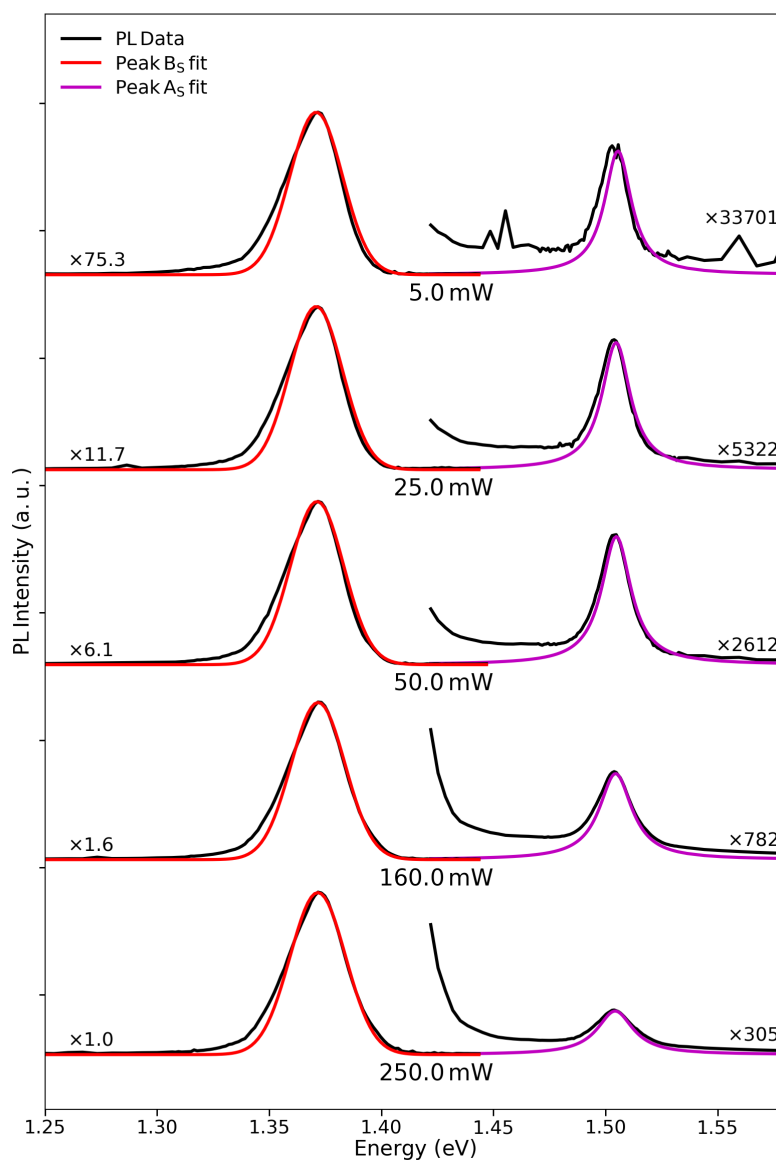


Figure 5.21: PL spectra of cell QD-s-700 at 20 K as a function of laser power. The tail at the left of peak A_s corresponds to peak B_s .

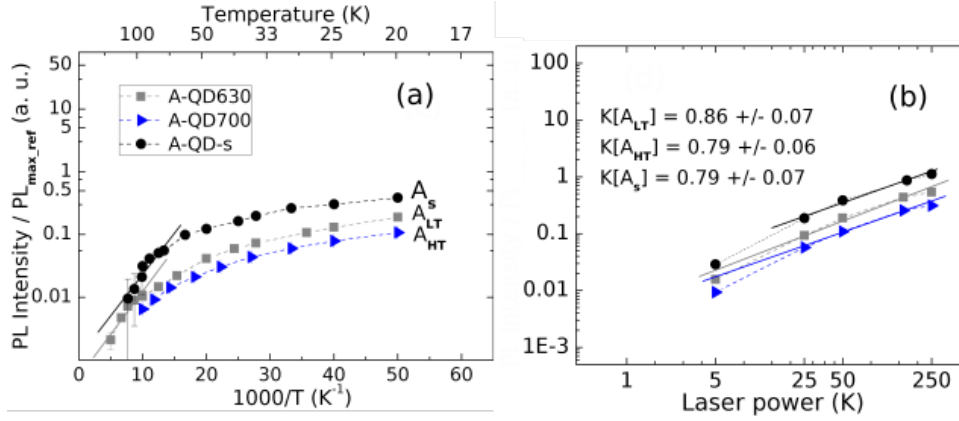


Figure 5.22: Intensity of peaks A_{LT} , A_{HT} , and A_s as a function of temperature (a) and as a function of laser power (b).

sample	peak	E_a	error E_a	k	error k
QD630	A_{LT}	27 meV	4 meV	0.86	0.07
QD700	A_{HT}	—	—	0.79	0.06
QD-s-700	A_s	28 meV	4 meV	0.79	0.07

Table 5.4: Activation energies E_a and constants k of peaks A_{LT} , A_{HT} , and A_s of the spectra of the IB solar cells. These values were calculated from the intensity data shown in figures 5.22.(a) and (b).

As the laser power increases, a higher number of electrons in the conduction band and holes in the valence band relax and fall in the confined energy levels. The higher degeneracy of the first excited state allows the confinement of more carriers which cannot be confined by the saturated ground states. Therefore, the intensity of the first excited state transition (the recombination between electrons and holes in the first excited energy levels) is stronger. Based on this assumption, we attribute peaks B_{LT} and C_{LT} to the ground and the first excited states transitions of the QDs, respectively.

The intensity of peak C_{LT} decreases with temperature faster than peak B_{LT} (see spectrum 5.16). This result also agrees with peak C_{LT} being a first excited state transition affected by carrier thermal escape (84) since the first excited energy levels for electrons and holes are relatively closer to the conduction band minimum level and valence band maximum level of GaAs, respectively (see figure 3.10). The pair of peaks B_{HT} and C_{HT} of the spectra of cell QD700 shows a similar result when the temperature is raised (see spectrum 5.18). However, the relative intensity of peak C_{HT} with respect to peak B_{HT} decreases with increasing the laser power, as observed from figure 5.23.(b). This indicates that C_{HT} does not follow the rule of the filling of the first excited states under high laser power.

Maybe the thermal excitation at 20 K is enough to induce carrier escape

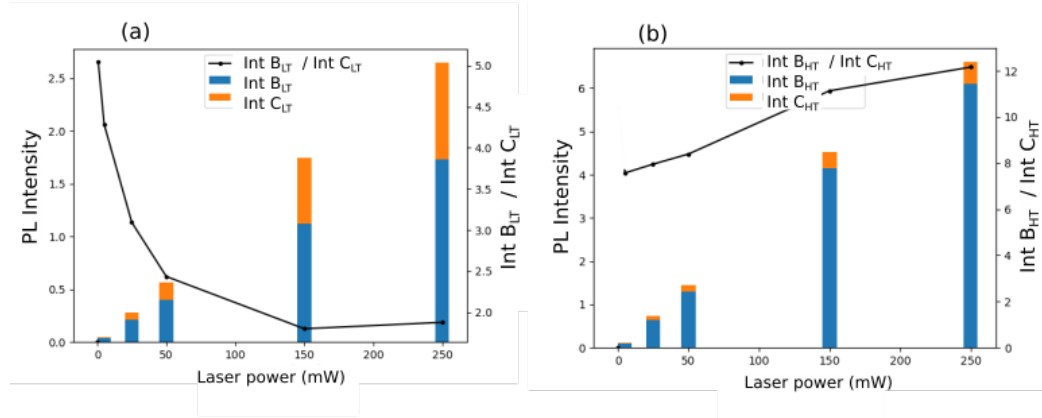


Figure 5.23: Dependence of the intensities of peaks B_{LT} , C_{LT} , B_{HT} , and C_{HT} with the laser power. Peaks B_{LT} and C_{LT} are analyzed in (a), and peaks B_{HT} and C_{HT} are analyzed in (b). The behaviour of the relative intensities are also shown.

from the first excited energy levels of the QDs to the bands, reducing in this way the probability of the first excited state transition and limiting the increase of intensity of peak C_{HT} . In fact, the energy levels corresponding to the transition C_{HT} are closer to the GaAs band edges than the energy levels corresponding to the transitions B_{LT} , C_{LT} , and B_{HT} because the emission energy of peak C_{HT} is higher. Considering the above assumptions, we attribute peaks B_{HT} and C_{HT} to the ground and first excited states transitions, respectively.

In the same way, we attribute peak B_s of the spectra of cell QD-s-700 (figures 5.20 and 5.21) to a ground state transition since it is the only one emission at low energy.

Concerning the simulations, these were performed at 20 K using the nextnano3 quantum nanostructure simulation code, based on a *Schrödinger* equation solver adapted to the effective mass approximation model (65). QDs with pyramid shape and aspect ratio height/diameter of 0.3 were simulated, according to the mean QD size found by microscopy measurements in a previous work (21). The QD material was simulated as a ternary compound $In_xGa_{1-x}As$, with Gallium compositions of 0%, 20% and 40%, taking into account possible Indium-Gallium intermixing during the growth of the GaAs capping layers above the QDs [(85),(86)]. This process can be seen in figure 5.24.

Figures 5.25.(a) and (b) show the energies of the ground and the first excited states transitions resulting from the simulations for cells QD630 and QD700. The ground and the first excited states transitions were named as E1-H1 and E2-H2, respectively. In both figures, each curve represents the transition energies for an interval of possible QD heights and for a fixed Gallium

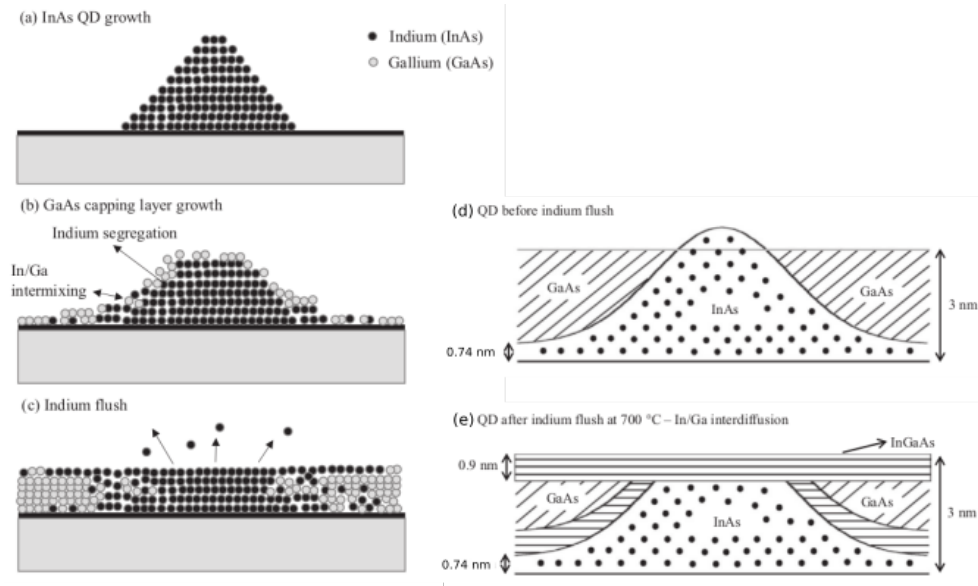


Figure 5.24: (a)-(c) Illustration of the QD morphology evolution during capping layer procedure and annealing. The Indium-Gallium intermixing takes place during the capping layer growth. (d)-(e) Removal of the tip of the QD that protrudes above the capping layer by Indium flush, shown for the case of cell QD-s-700. The formation of the InGaAs layer above the QDs of this cell is also shown at the bottom. All these figures were taken from (21).

composition. In the case of cells QD630 and QD700, the possible maximum QD height is 6 nm since the Indium flush is expected to limit the QD height at the height of the GaAs capping layers, as schematized in figure 5.24. The possible minimum QD height in the two cells is 2 nm, as observed from previous atomic force microscopy (AFM) results (21). These maximum and minimum heights were fixed as the ends of the intervals of height for the simulations.

The color boxes seen in the figures delimit both the QD heights interval and the range of emission energies of the PL peaks attributed to the ground and the first excited states transitions. The central emission energies of the peaks at 20 K are also indicated by a line at half of the height of the boxes, while the heights of the boxes were determined by the respective FWHM.

In the case of cell QD630, the simulated curves for the E1-H1 transition at 0%, 20%, and 40% of Gallium content cross the bottom color box (see figure 5.25.(a)). The same occurs with the simulations for the E2-H2 transition at 0%, 20%, and 40% (see figure 5.25.(b)). This suggests that peaks B_{LT} and C_{LT} correspond to emissions from InAs QDs or from InGaAs QDs with some Gallium content, which should not exceed 60% since the curves at 60% barely touch the top of the gray boxes. In the case of cell QD700, only the curves at 40% and 60% of Gallium composition cross the top color boxes. Therefore, peaks B_{HT} and C_{HT} would correspond to emissions from InGaAs QDs with

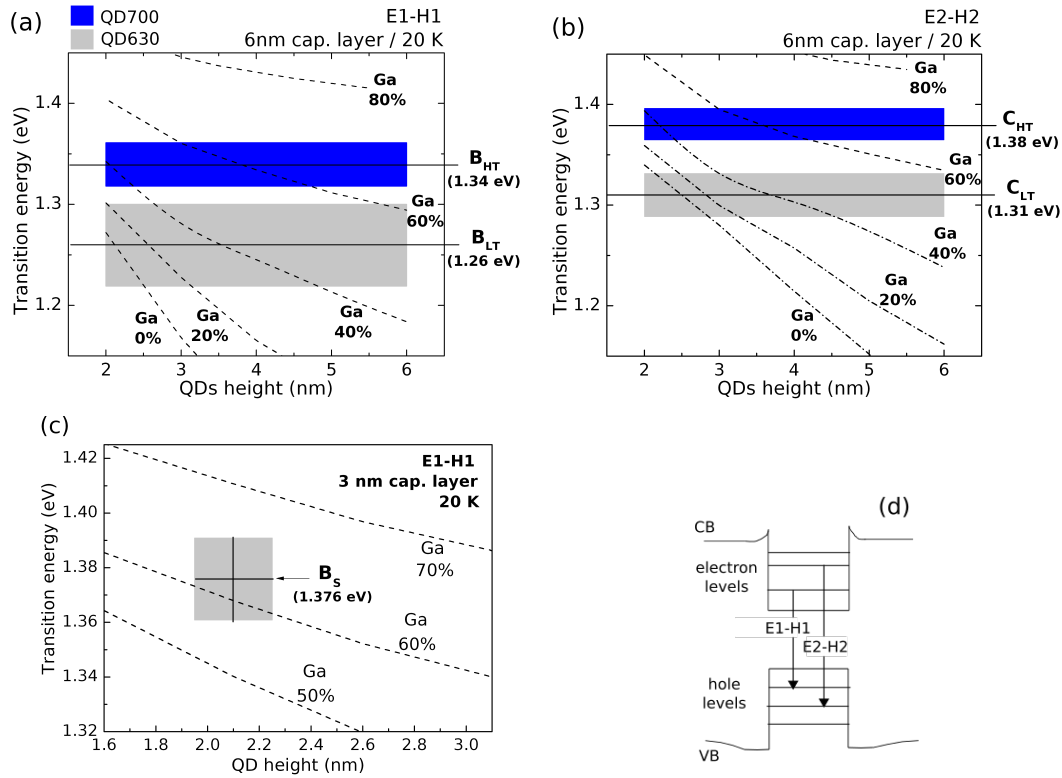


Figure 5.25: (a)-(c) Energies of the ground and first excited states transitions E1-H1 and E2-H2 obtained by simulation. E1-H1 and E2-H2 are schematized in (d). The QD PL emissions of solar cells QD630 and QD700 are compared to the simulations in (a) and (b), while the QD PL emission of cell QD-s-700 is compared to the simulations in (c). Figure (c) was taken from (21).

Gallium content above 20% and below 80%.

In relation to cell QD-s-700, the same simulations reported in the previous work (21) for QDs capped with 3nm-GaAs layers and annealed at 700 °C were used. Such simulations are based on QDs with an aspect ratio height/radius = 0.4, and include an additional InGaAs layer of 0.9 nm-thick (shown in figure 5.24.(e)) produced by Indium-Gallium interdiffusion that spreads over a larger area above the QDs, according to results of transmission electron microscopy (STEM). From those same results, the averaged QD height is estimated at 2.1 nm with a margin of error of 0.15 nm. Figure 5.25.(c) shows the simulated curves and also a color box delimiting both the estimated height range and the emission energy range of peak B_s . The intersection of the curve at 60% with the box indicates that peak B_s is an emission from InGaAs QDs with about 60% of Gallium content.

We confirm hence that the emission energies of peaks B_{LT} , C_{LT} , B_{HT} , C_{HT} , and B_s agree with the energies of the ground and the first excited state transitions for certain intervals of QD composition. Moreover, the results of the simulations indicate a possible increase of the maximum Gallium composition

when the annealing temperature of the QDs is raised from 630 °C (cell QD630) to 700 °C (cells QD700 and QD-s-700). This is possibly due to a higher Indium-Gallium intermixing.

The emissions identified on the PL spectra of the IB solar cells are summarized in figure 5.26.

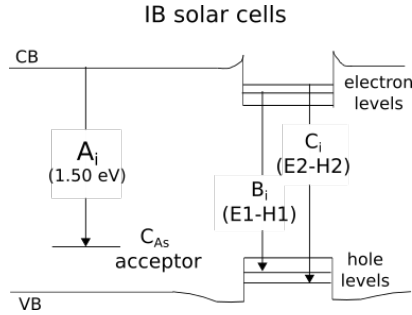


Figure 5.26: Emissions identified on the PL spectra of the solar cells QD630 ($i=LT$), QD700 ($i=HT$), and QD-s-700 ($i=s$). B_i and C_i are the PL emissions from the QDs and represent the ground and the first excited states transitions, respectively. The spectra of cell QD-s-700 show only the ground state transition, peak B_s .

5.2

Discussion of the PL results

5.2.1

PL results of the solar cells without QDs and samples p570 and n630

The emissions seen in the PL spectra of the solar cells without QDs, cells SC630, SC700, and SCycle, have shown the presence of carbon and silicon impurities, as well as silicon complexes in their structure. Since the structure of the IB solar cells QD630, QD700, and QD-s-700 is based on the structure of the above cells, we assume that carbon impurities and silicon complexes are also present in the IB solar cells.

The presence of carbon impurities in the p -sides and silicon acceptors in the n -sides are based on the detection of emissions γ_i of the cells without QDs which were attributed to the superposition of the two emissions conduction band-to- C_{As} and conduction band-to- Si_{As} (see figure 5.8). We make a new consideration here in relation to peaks γ_i : probably a (small) intensity fraction of the conduction band-to- C_{As} emission has origin in the GaAs capping and spacer layers of the active region, as well as in the silicon-doped layers of the n -side. The reason to make this assumption is that these layers are thought to be contaminated with low residual carbon concentrations since, as already mentioned, undoped GaAs samples of calibration, grown previously in our

laboratory, were found to be *p*-type doped. Based on this result, we believe that all the GaAs layers grown inside our MOVPE reactor under similar growth conditions are carbon-contaminated, including those intentionally doped with silicon. In this last case, the residual carbon concentration should be lower than in the case of undoped GaAs samples because silicon competes with carbon to substitute Arsenic atoms in the GaAs lattice.

The other (major) intensity fraction of the conduction band-to- C_{As} emission obviously corresponds to the recombinations via the carbon impurities in the highly carbon-doped *p*-side.

According to the above considerations, the active layers and *n*-sides of the solar cells without QDs and IB solar cells are carbon-contaminated. However, we cannot determine if the carbon contamination affects the efficiencies of the solar cells because the similar growth conditions of the active regions and *n*-sides are expected to allow the incorporation of the same carbon concentrations (the carbon concentrations in the GaAs layers of the active regions are about $1 \times 10^{15} \text{ cm}^{-3}$ for growth temperatures between 630 °C and 700 °C according to their nominal doping concentrations). It means that there is no appreciable difference between the cells in terms of residual carbon impurities so that the influence on the efficiency cannot be distinguished.

The same occurs to the silicon acceptors in the *n*-sides of the cells, whose concentrations are expected to be the same due to that the same growth parameters were applied to grow these sides. Therefore, we cannot establish if these acceptors have some negative influence on the efficiencies of the IB solar cells.

Concerning the silicon complexes $Si_{Ga} - V_{Ga}$ and $Si_{As} - V_{As}$, their presence in the *n*-sides of the solar cells was determined based on the detection of PL peaks α_i and β_i in the spectra of the cells without QDs, as well as peaks α and β in the spectra of sample n630 (see figure 5.12). These complexes are the only defects we have found in the structure of the IB solar cells by PL. Unfortunately, we cannot estimate their concentrations in the *n*-sides based on the intensities of peaks α_i and β_i because these emissions were obtained by the re-absorption of light emitted by the active region, so the emissions should represent only a small fraction of the complexes present in the *n*-sides. Hence, we cannot establish the difference in concentration of silicon complexes existing between the *n*-sides of the three IB solar cells and, therefore, it is not possible to determine how much the complexes affect their performances.

It is worth to note that an unknown acceptor was detected in sample p570 by means of emission K, attributed to a conduction band-to-shallow acceptor transition (see figure 5.4). Such acceptor seems to be the same acceptor

involved in the (D-A) transition attributed to emission θ of the spectra of sample n630 (figure 5.8) since the ionization energies of the two acceptors are quite similar ([52-53] meV). Most likely, the same unknown acceptor is also formed on sample n630.

However, we cannot affirm that such acceptor is also formed in the p and n -sides of the IB solar cells, because it was not identified any related emission in their PL spectra or in the PL spectra of the solar cells without QDs. This result is strange because the concentration of the acceptor seems to be even higher than the carbon concentration in sample p570 according to its relative higher PL intensity, as can be observed in figure 5.3.(a). Then, one would expect to see an intense PL emission in the spectra of the IB solar cells and cells without QDs at the same position than peak K (1.48 eV at 20 K), but it does not occur. Instead, a tiny peak appears around the same position as peak θ (1.46 eV at 20 K), as seen in figure 5.12. This tiny peak has almost the same intensity than peak θ , but it could not be studied due to their low resolution.

If this peak corresponds to the same (D-A) emission than peak θ , then it would confirm the presence of the unknown acceptor in the structure of the IB solar cells. Therefore, new PL measurements of higher resolution must be performed on the cells without QDs in order to identify the unresolved peak.

5.2.2 PL results of the IB solar cells

Concerning cells QD630, QD700, and QD-s-700, their spectra have shown two types of emission, as can be observed in figure 5.26: one corresponds to the conduction band-to-carbon acceptor transition (peaks A_i), which involves the carbon impurities in the p -side and also probably residual carbon in the active region. The other type of emission corresponds to the internal transitions of the QDs, it is, the ground and the first excited state transitions emissions. The ground state transition emissions were identified as peaks B_{LT} (cell QD630), B_{HT} (cell QD700), and B_s (cell QD-s-700), while the first excited state transition emissions were identified as peaks C_{LT} (cell QD630) and peak C_{HT} (cell QD700). Cell QD-s-700 did not exhibit this emission.

Unlike the PL spectra of the solar cells without QDs, the PL spectra of the IB solar cells did not show the presence of any defect. Most likely, the silicon complexes-related emissions are not observed on the spectra of the IB solar cells because of the strong absorption of light by the QDs in the active regions, which should limit the re-absorption on the n -side. However, the complexes are expected to be also present in the n -sides of these cells.

Despite the fact that the emissions of the IB solar cells are not related to defects, the results seen by DLTS and Laplace DLTS can be related to the evolution of the QD emissions from one cell to another. As observed from figure 5.27, there is a relative increase of the intensity of the emission attributed to the ground state transition at 20 K, from cell QD630 (peak B_{LT}) to cell QD700 (peak B_{HT}), and from this cell to cell QD-s-700 (peak B_s). The increase of this emission evidences an improvement of the optical quality of cells QD700 and QD-s-700 in comparison to cell QD630, which leads to higher sub-bandgap energy absorption in these cells, as shown by the external quantum efficiency measurements of figure 4.17.

The enhancement of the ground state transition from cell QD630 to cells QD700 and QD-s-700 (increases of peak intensity of 6 times and 46 times, respectively) is attained for the increase of the QD annealing temperature and the growth temperature of the spacer layers to 700 °C. This enhancement agrees with the reduction of the EL2 centers at this temperature seen by DLTS (figures 4.14 and 4.16), and with the drastic reduction of almost all the electron and hole traps detected by DLTS and Laplace DLTS in the active region of cell QD630, except for trap EL2, since no one of those traps were detected in the active regions of cells QD700 and QD-s700. This means that the reduction of defects in the active region by the increase in temperature induces the improvement of the optical quality of these cells. This improvement consists, therefore, of a better quality of the GaAs spacer layers and a better quality of the interfaces between the In(Ga)As QD layers and the surrounding GaAs layers. In these conditions, more electrons and more holes reach the lower confined energy levels of the QDs before radiatively recombining and, as a consequence, the emission related to the ground state transition becomes more intense.

The relative increase of the emission intensity of the ground state

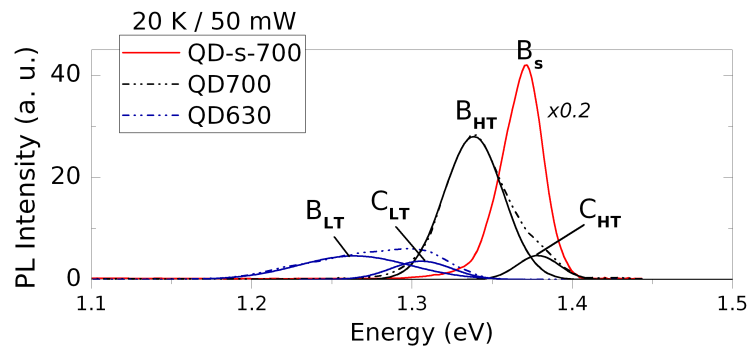


Figure 5.27: Comparison between the QD emissions observed in spectra of cells QD630, QD700, and QD-s-700 below 1.45 eV (figures 5.16 to 5.21).

transition from cell QD700 (peak B_{HT}) to cell QD-s-700 (peak B_s) of 7.5 times is attained due to the reduction of the capping layer thickness from 6 nm to 3 nm. The previous transmission electron microscopy measurements have confirmed the decrease of the QD height and the improvement of the homogeneity of the QD size for cell QD-s-700, in contrast to the case of cell QD630, whose QDs are of different shapes and heights. These changes in the QD morphology seem to be the main contribution to the higher efficiency of cell QD-s-700 since there is no appreciable difference between this cell and cell QD700 in terms of defects. As shown in the chapter of DLTS and Laplace DLTS results, EL2 is the only defect detected in the active region of these cells and is found in very similar concentrations in both cells ($4.2 \times 10^{15} \text{ cm}^{-3}$ and $2.6 \times 10^{15} \text{ cm}^{-3}$, see figure 4.16). Therefore, there is no appreciable reduction of defects in the active region of cell QD-s-700 caused by the reduction of the QD height.

The improved optical quality of cell QD-s-700 achieved by the reduction of the QD height is consistent with the relative increase of the sub-bandgap energy absorption of cell QD-s-700 in comparison to cell QD700, as observed in figure 4.17 and as already mentioned in section 4.3.3.

There is no significant increase in the intensity of the emission related to the first excited state transition from cell QD630 (peak C_{LT}) to cell QD700 (peak C_{HT}), probably due to the carrier thermal escape experienced by the first excited energy levels of the QDs of cell QD700, as assumed in the last section 5.1.4.

5.3

Summary

In this chapter, the photoluminescence spectra of the IB solar cells and solar cells without QDs, as well as the spectra of the individually doped GaAs samples, have been presented.

It was assumed that all the GaAs layers of the active regions and n -sides of the IB solar cells and solar cells without QDs most probably are carbon-contaminated. This assumption is based on the analysis of emissions γ_i of the solar cells without QDs, as well as the interpretation of the p -type carrier concentrations of undoped GaAs calibration samples previously grown under similar conditions.

Also, from the analysis of peaks γ_i , it was assumed the presence of silicon acceptors in the n -sides, which more probably are due to the amphoteric behavior of silicon in GaAs.

Another important result is the detection of the silicon complexes Si_{Ga} –

V_{Ga} and $Si_{As}-V_{As}$ in the n -sides of the solar cells by means of the measurement of the α_i and β_i emissions in the spectra of the solar cells without QDs. The origin of these complexes is confirmed by the identification of the same types of emissions in the spectra of sample n630. These complexes are also a consequence of the amphoteric behavior of silicon.

In addition, the relatively high optical quality of cells QD700 and QD-s-700 were evidenced by their intense QD emissions. These features coincide with the reduction of the number of traps and the reduction of the EL2 concentration in the active regions of these cells in comparison to cell QD630, according to the DLTS and Laplace DLTS results.

6

Conclusions

Three MOVPE-grown intermediate band solar cells with different growth temperatures of GaAs spacer layers and different GaAs capping layer thicknesses have been studied in this work in order to determine the influence of crystalline defects in their energy conversion efficiencies. These cells show different efficiencies (2.8%, 5.1%, and 6.9%), as previously established in another work. Among them, the cell with the highest growth temperature (700 °C) and the thinner capping layer (3 nm), cell QD-s-700, shows the highest efficiency (6.9%).

Important differences in the amount and concentration of traps over the active regions of the cells were determined by DLTS and Laplace DLTS. Cell QD630, with the lowest growth temperature of the spacer layers (630 °C) and thick capping layers (6 nm) exhibits a large number of traps. The formation of all these traps, except for trap EL2, is apparently inhibited at 700 °C since they were not detected in the active regions of the two cells with spacer layers grown at this temperature, cells QD700 and QD-s-700. Moreover, the concentration of trap EL2 is decreased. These results demonstrate that the reduction of the trap-related defects in the active regions by increasing the spacer layers-growth temperature influences positively the efficiency of the IB solar cells.

In addition, three new solar cells with equivalent structures to the IB cells but without QDs were grown and studied by DLTS and Laplace DLTS. The comparison between the DLTS and Laplace DLTS spectra of these cells and the ones of the IB solar cells allowed determining that a pair of hole traps in the active region of cell QD630 (traps 4*630-0.25 and 4-630-0.5) is strictly related to the QD growth conditions. On the other hand, trap EL2 and two unknown traps A and H thought to be present in the three IB solar cells, were found to be only related to the growth conditions of the spacer layers, but their concentrations increase by the influence of the growth temperature cycle of the QDs, which includes a period of low temperature (500 °C). These results evidence that the growth of the QDs is responsible for the formation of new hole defects and the increase in density of other spacer layers growth-related defects in the active regions, probably contributing to the low efficiency in the case of cell QD630. However, the experimental evidence showed that all

the traps, regardless of their origin, are reduced by the increase of the spacer layers-growth temperature to 700 °C, as is the case of cells QD700 and QD-s-700.

Probably, there are Arsenic antisites-related defects, including EL2, and other unidentified defects present in the p and n -sides of the IB solar cells, according to the DLTS and Laplace DLTS results of individually carbon and silicon-doped GaAs samples. Therefore, the photocurrent of the cells, which is collected via the p and n -sides, can be reduced due to recombination of carriers through such defects.

Unlike the DLTS and Laplace DLTS, the photoluminescence studies focused on the entire structure of the IB solar cells, which allowed us to search for impurities and defects at the p and n -sides besides the active regions of the solar cells. Based on the PL spectra of the cells without QDs, it was detected the presence of silicon defects complexes ($Si_{Ga} - V_{Ga}$ and $Si_{As} - V_{As}$) in the n -sides of the cells. We believe these complexes were measured in each cell due to the optical excitation of the n -side which re-absorbs a fraction of the photons emitted by the active region.

Also, it has been assumed that all the GaAs layers of the active regions and n -sides of the IB solar cells and solar cells without QDs most probably are carbon-contaminated. This assumption is based on the analysis of emissions γ_i of the spectra of the solar cells without QDs and the interpretation of the p -type carrier concentrations of undoped GaAs calibration samples previously grown under similar conditions. Furthermore, the characteristics of emissions γ_i also coincide with the ones of emissions through silicon acceptor impurities, whose presence in the n -sides was confirmed by the identification of the $Si_{As} - V_{As}$ complex.

Unfortunately, it was not possible to determine if there exists a relation between the concentrations of the complexes and residual carbon impurities and the efficiencies of the IB solar cells.

An interesting result is that the PL emissions associated with the QDs show an improvement in the optical quality of the cells with the highest growth temperature of the spacer layers, cells QD700 and QD-s-700. The optical improvement is seen as an increment of the intensities of the ground state transition emissions and is also evidenced by the relative high sub-bandgap photon absorption of these cells observed from previous external quantum efficiency measurements. This optical improvement coincides with the reduction of the number and intensity of defects in the active region at 700 °C shown by the DLTS and Laplace DLTS measurements. We think that this reduction improves the material quality of the GaAs spacers and capping

layers around the QDs, allowing more optically excited electrons in the QDs to escape and reach the GaAs conduction band without being captured by traps/recombination centers around the QDs during the operation of the solar cells. In this way, the sub-bandgap photon absorption through the QDs is increased, leading to higher photocurrent and higher efficiency.

On the other hand, the reduction and homogenization of the QD height, achieved by decreasing the capping layer thickness, has shown that it also improves the optical quality and the efficiency of cell QD-s-700. This reduction allows a stronger sub-bandgap photon absorption for this cell in comparison to cell QD700. Since there is no a significant difference between the EL2 concentrations (the only detected defects) in the active regions of both cells, we believe that the QD height reduction is the main contribution to the relatively high efficiency of cell QD-s-700. This reduction is, therefore, as beneficial as the increase of the spacer layers-growth temperature to 700 °C.

Bibliography

- [1] RITCHIE, H.; ROSER, M.. *CO₂ and other greenhouse gas emissions*. Our World in Data. <https://ourworldindata.org/co2-and-other-greenhouse-gas-emissions>. Last accessed: June 2019.
- [2] LUQUE, A.; HEGEDUS, S.. **Handbook of Photovoltaic Science and Engineering**. John Wiley and Sons, second edition, 2011.
- [3] **Global trends in renewable energy investment 2018**. <https://europa.eu/capacity4dev/unep/documents/global-trends-renewable-energy-investment-2018>. Frankfurt School – UNEP Collaborating Centre for Climate and sustainable energy finance, Frankfurt School of Finance and Management, Bloomberg New Energy Finance, United Nations Environment Programme. Last accessed: Jul 2019.
- [4] TIBBITS, T. N.; BEUTEL, P.; GRAVE, M.; KARCHER, C.; OLIVA, E.; SIEFER, G.; WEKKELI, A.; SCHACHTNER, M.; DIMROTH, F.; BETT, A. W. ; OTHERS. **New efficiency frontiers with wafer-bonded multi-junction solar cells**. In: 29TH EUROPEAN PV SOLAR ENERGY CONFERENCE AND EXHIBITION, p. 22–26. Amsterdam, Netherlands, 2014.
- [5] PHILIPPS, S. P.; DIMROTH, F. ; BETT, A. W.. **Chapter id-2 - High-Efficiency III-V Multijunction Solar Cells**. In: McEvoy, A.; Markvart, T. ; Castañer, L., editors, PRACTICAL HANDBOOK OF PHOTOVOLTAICS, p. 417–448. Academic Press, second edition, 2012.
- [6] LUQUE, A.; MARTÍ, A.. **Increasing the efficiency of ideal solar cells by photon induced transitions at intermediate levels**. Physical Review Letters, 78(26):5014, 1997.
- [7] LUQUE, A.; MARTÍ, A. ; STANLEY, C.. **Understanding intermediate-band solar cells**. Nature Photonics, 6(3):146–152, 2012.
- [8] MARTÍ, A.; ANTOLÍN, E.; CÁNOVAS, E.; LÓPEZ, N.; LINARES, P.; LUQUE, A.; STANLEY, C. ; FARMER, C.. **Elements of the design and**

- analysis of quantum-dot intermediate band solar cells. *Thin solid films*, 516(20):6716–6722, 2008.
- [9] CAPPER, P.; IRVINE, S. ; JOYCE, T.. **Epitaxial Crystal Growth: Methods and Materials**. Springer International Publishing, 2017.
- [10] SCHMIEDER, K. J.; ARMOUR, E. A.; LUMB, M. P.; YAKES, M. K.; PULWIN, Z.; FRANTZ, J. ; WALTERS, R. J.. **Effect of growth temperature on GaAs solar cells at high MOCVD growth rates**. *IEEE Journal of Photovoltaics*, 7(1):340–346, 2017.
- [11] LANG, R.; SCHÖN, J.; DIMROTH, F. ; LACKNER, D.. **Optimization of gaas solar cell performance and growth efficiency at MOVPE growth rates of 100 $\mu\text{m}/\text{h}$** . *IEEE Journal of Photovoltaics*, (99):1–5, 2018.
- [12] COMINATO WEINER, E.. **Células solares de banda intermediária de pontos quânticos baseadas em InAs/GaAs/AlGaAs**. Dissertação (mestrado), Pontifícia Universidade Católica do Rio de Janeiro, Departamento de Engenharia Elétrica, 2015.
- [13] WEINER, E. C.; MICHA, D. N.; JAKOMIN, R.; PINTO, L. D.; PIRES, M. P. ; SOUZA, P. L.. **Improving the figures of merit of intermediate band solar cells by controlling the capping procedure of the quantum dots**. In: 2016 IEEE 43RD PHOTOVOLTAIC SPECIALISTS CONFERENCE (PVSC), p. 2080–2083. IEEE, 2016.
- [14] STRINGFELLOW, G. B.. **Organometallic vapor-phase epitaxy: Theory and practice**, chapter 8. Academic Press, second edition, 1999.
- [15] STRINGFELLOW, G.. **Novel precursors for organometallic vapor phase epitaxy**. *Journal of crystal growth*, 128(1-4):503–510, 1993.
- [16] KUECH, T.; VEUHOFF, E.. **Mechanism of carbon incorporation in MOCVD GaAs**. *Journal of Crystal Growth*, 68(1):148–156, 1984.
- [17] HABERLAND, K.. **Optical in-situ studies during metal-organic vapor phase epitaxy with respect to III-V device production**. Thesis (ph.d.), Technical University of Berlin, Faculty of mathematics and natural sciences, 2002.
- [18] BAUER, G.; RICHTER, W.. **Optical Characterization of Epitaxial Semiconductor Layers**, chapter 2. Springer-Verlag, Berlin, Heidelberg, first edition, 1996.

- [19] OURA, K.; KATAYAMA, M.; LIFSHITS, V.; SARANIN, A. ; ZOTOV, A.. **Surface Science: An introduction**, chapter 14. Springer, first edition, 2003.
- [20] JAKOMIN, R.; KAWABATA, R.; MOURÃO, R.; MICHA, D.; PIRES, M.; XIE, H.; FISCHER, A.; PONCE, F. ; SOUZA, P.. **InAs quantum dot growth on AlGaAs by metalorganic vapor phase epitaxy for intermediate band solar cells**. *Journal of Applied Physics*, 116(9):093511, 2014.
- [21] WEINER, E.; JAKOMIN, R.; MICHA, D.; XIE, H.; SU, P.-Y.; PINTO, L.; PIRES, M.; PONCE, F. ; SOUZA, P.. **Effect of capping procedure on quantum dot morphology: Implications on optical properties and efficiency of InAs/GaAs quantum dot solar cells**. *Solar Energy Materials and Solar Cells*, 178:240–248, 2018.
- [22] LANG, D.. **Deep-level transient spectroscopy: A new method to characterize traps in semiconductors**. *Journal of applied physics*, 45(7):3023–3032, 1974.
- [23] STIEVENARD, D.; VUILLAUME, D.. **Profiling of defects using deep level transient spectroscopy**. *Journal of Applied Physics*, 60(3):973–979, 1986.
- [24] AZIZ, M.; MARI, R.; FELIX, J.; MESLI, A.; TAYLOR, D.; LEMINE, M.; HENINI, M.; PILLAI, R.; STARIKOV, D.; BONEY, C. ; OTHERS. **Deep level transient spectroscopy characterisation of defects in Al-GaN/Si dual-band (UV/IR) detectors grown by MBE**. *physica status solidi (c)*, 10(1):101–104, 2013.
- [25] DOBACZEWSKI, L.; PEAKER, A. ; BONDE NIELSEN, K.. **Laplace-transform deep-level spectroscopy: The technique and its applications to the study of point defects in semiconductors**. *Journal of Applied Physics*, 96(9):4689–4728, 2004.
- [26] DOBACZEWSKI, L.; HAWKINS, I. ; PEAKER, A.. **Laplace transform deep level transient spectroscopy: new insight into defect microscopy**. *Materials science and technology*, 11(10):1071–1073, 1995.
- [27] KRZYSZTOF GOSCINSKI. **Laplace transform Transient Processor and Deep Level Spectroscopy**. http://info.ifpan.edu.pl/Dodatki/WordPress/laplacedlts/?page_id=9. Last accessed: October 2017.

- [28] DEIXLER, P.; TERRY, J.; HAWKINS, I.; EVANS-FREEMAN, J.; PEAKER, A.; RUBALDO, L.; MAUDE, D.; PORTAL, J.-C.; DOBACZEWSKI, L.; BONDE NIELSEN, K. ; OTHERS. **Laplace-transform deep-level transient spectroscopy studies of the G4 gold-hydrogen complex in silicon.** Applied physics letters, 73(21):3126–3128, 1998.
- [29] BOGARDUS, E. H.; BEBB, H. B.. **Bound-exciton, free-exciton, band-acceptor, donor-acceptor, and Auger recombination in GaAs.** Physical Review, 176(3):993, 1968.
- [30] LUSTOZA DE SOUZA, P.. **A dopagem silicio em camadas epitaxiais AlGaAs sob o ponto de vista da fotoluminescencia.** Thesis (ph.d. in physics), Pontifícia Universidade Católica do Rio de Janeiro, Departamento de Física, 1989.
- [31] KY, N. H.; REINHART, F.. **Amphoteric native defect reactions in Si-doped GaAs.** Journal of applied physics, 83(2):718–724, 1998.
- [32] VISSER, E.; TANG, X.; WIELEMAN, R. ; GILING, L.. **Deep-level photoluminescence studies on Si-doped, metalorganic chemical vapor deposition grown Al_xGa(1-x)As.** Journal of applied physics, 69(5):3266–3277, 1991.
- [33] LIDEIKIS, T.; TREIDERIS, G.. **Photoluminescence study of acceptors in silicon-doped gallium arsenide grown by metalorganic chemical vapor deposition.** Journal of crystal growth, 96(4):790–794, 1989.
- [34] LEROUX, M.; GRANDJEAN, N.; BEAUMONT, B.; NATAF, G.; SEMOND, F.; MASSIES, J. ; GIBART, P.. **Temperature quenching of photoluminescence intensities in undoped and doped GaN.** Journal of Applied Physics, 86(7):3721–3728, 1999.
- [35] WELLS, N. P.; DRISKELL, T. U.; HUDSON, A. I.; LALUMONDIERE, S. D.; LOTSHAW, W. T.; FORBES, D. V. ; HUBBARD, S. M.. **Carrier quenching in InGaP/GaAs double heterostructures.** Journal of Applied Physics, 118(6):065703, 2015.
- [36] SCHMIDT, T.; LISCHKA, K. ; ZULEHNER, W.. **Excitation-power dependence of the near-band-edge photoluminescence of semiconductors.** Physical Review B, 45(16):8989, 1992.
- [37] SZE, S. M.. **Physics of semiconductor devices**, chapter 3. John Wiley and Sons, Inc., New York, first edition, 1969.

- [38] SCHRODER, D. K.. **Semiconductor material and device characterization**, chapter 3. John Wiley and Sons, Inc., New Jersey, third edition, 2006.
- [39] VAN ZEGHBROECK, B.. **Principles of electronic devices**. https://ecee.colorado.edu/~bart/book/book/chapter4/ch4_3.htm. Last accessed: January 2019.
- [40] JIANG, Z.. **Deep level transient spectroscopy measurements of GaAsBi/GaAs**. Thesis (master of science), Simon Fraser University, Department of Physics, 2010.
- [41] WANG, P.; KUECH, T.; TISCHLER, M.; MOONEY, P.; SCILLA, G. ; CARDONE, F.. **Deep levels in p-type GaAs grown by metalorganic vapor phase epitaxy**. *Journal of applied physics*, 64(10):4975–4986, 1988.
- [42] SCHRODER, D. K.. **Semiconductor material and device characterization**, chapter 2. John Wiley and Sons, Inc., New Jersey, third edition, 2006.
- [43] MITROFANOV, O.; MANFRA, M.. **Poole-frenkel electron emission from the traps in AlGaIn/GaN transistors**. *Journal of Applied Physics*, 95(11):6414–6419, 2004.
- [44] NAZ, N. A.; QURASHI, U. S. ; IQBAL, M. Z.. **Arsenic antisite defects in p-GaAs grown by metal-organic chemical-vapor deposition and the EL2 defect**. *Journal of Applied Physics*, 106(10):103704, 2009.
- [45] LAGOWSKI, J.; LIN, D.; CHEN, T.-P.; SKOWRONSKI, M. ; GATOS, H.. **Native hole trap in bulk GaAs and its association with the double-charge state of the arsenic antisite defect**. *Applied physics letters*, 47(9):929–931, 1985.
- [46] MANASREH, M.; BROWN, G.. **The double donor issue of the EL2 defect in GaAs**. *MRS Online Proceedings Library Archive*, 163, 1989.
- [47] BENCHERIFA, A.; BRÉMOND, G.; NOUAILHAT, A.; GUILLOT, G.; GUIV-ARC'H, A. ; REGRENY, A.. **On the identification of the double donor state of EL2 in p-type GaAs**. *Revue de Physique Appliquée*, 22(8):891–895, 1987.
- [48] ALONSO-ÁLVAREZ, D.; WILSON, T.; PEARCE, P.; FÜHRER, M.; FARRELL, D. ; EKINS-DAUKES, N.. **Solcore: a multi-scale, Python-based**

- library for modelling solar cells and semiconductor materials. *Journal of Computational Electronics*, p. 1–25, 2018.
- [49] MITONNEAU, A.; MARTIN, G. ; MIRCEA, A.. **Hole traps in bulk and epitaxial GaAs crystals**. *Electronics Letters*, 13(22):666–668, 1977.
- [50] MOONEY, P.; TARUN, M.; BAHRAMI-YEKTA, V.; TIEDJE, T.; LEWIS, R. ; MASNADI-SHIRAZI, M.. **Defect energy levels in p-type GaAsBi and GaAs grown by MBE at low temperatures**. *Semiconductor Science and Technology*, 31(6):065007, 2016.
- [51] BUCHWALD, W.; JOHNSON, N. ; TROMBETTA, L.. **New metastable defects in GaAs**. *Applied physics letters*, 50(15):1007–1009, 1987.
- [52] SHINAGAWA, T.; OKUMURA, T.. **Role of the EL2 center on the formation of metastable hydrogen-related defects (M3/M4) in n-GaAs**. *Japanese journal of applied physics*, 37(4R):1939, 1998.
- [53] TOKUDA, Y.; KAMIYA, K. ; OKUMURA, T.. **Properties of metastable hydrogen-related defects in n-type GaAs studied by isothermal deep-level transient spectroscopy**. *Journal of Applied Physics*, 88(4):1943–1947, 2000.
- [54] SOLTANOVICH, O.; KOLKOVSKY, V.; YAKIMOV, E. ; WEBER, J.. **Metastable hydrogen-related defects in epitaxial n-GaAs studied by laplace deep level transient spectroscopy**. In: *AIP CONFERENCE PROCEEDINGS*, volumen 1583, p. 195–198. AIP, 2014.
- [55] LEITCH, A.; PRESCHA, T. ; WEBER, J.. **Hydrogen-related metastable defects in passivated n-type GaAs grown by metal-organic vapor-phase epitaxy**. *Physical Review B*, 45(24):14400, 1992.
- [56] MOONEY, P.; WATKINS, K.; JIANG, Z.; BASILE, A.; LEWIS, R.; BAHRAMI-YEKTA, V.; MASNADI-SHIRAZI, M.; BEATON, D. ; TIEDJE, T.. **Deep level defects in n-type GaAsBi and GaAs grown at low temperatures**. *Journal of Applied Physics*, 113(13):133708, 2013.
- [57] KRAMBROCK, K.; LINDE, M.; SPAETH, J.-M.; LOOK, D. C.; BLISS, D. ; WALUKIEWICZ, W.. **Arsenic antisite-related defects in low-temperature MBE grown GaAs**. *Semiconductor science and technology*, 7(8):1037, 1992.
- [58] LOOK, D. C.; FANG, Z.-Q.; YAMAMOTO, H.; SIZELOVE, J.; MIER, M. ; STUTZ, C.. **Deep traps in molecular-beam-epitaxial GaAs grown at low temperatures**. *Journal of applied physics*, 76(2):1029–1032, 1994.

- [59] LIU, X.; PRASAD, A.; CHEN, W.; KURPIEWSKI, A.; STOSCHEK, A.; LILIENTAL-WEBER, Z. ; WEBER, E.. **Mechanism responsible for the semi-insulating properties of low-temperature-grown GaAs.** Applied physics letters, 65(23):3002–3004, 1994.
- [60] LUYSBERG, M.; SOHN, H.; PRASAD, A.; SPECHT, P.; LILIENTAL-WEBER, Z.; WEBER, E.; GEBAUER, J. ; KRAUSE-REHBERG, R.. **Effects of the growth temperature and As/Ga flux ratio on the incorporation of excess As into low temperature grown GaAs.** Journal of applied physics, 83(1):561–566, 1998.
- [61] VON BARDELEBEN, H.; STIEVENARD, D.; DERESMES, D.; HUBER, A. ; BOURGOIN, J.. **Identification of a defect in a semiconductor: EL2 in GaAs.** Physical Review B, 34(10):7192, 1986.
- [62] BOURGOIN, J.; VON BARDELEBEN, H. ; STIEVENARD, D.. **Native defects in gallium arsenide.** Journal of applied physics, 64(9):R65–R92, 1988.
- [63] SOBOLEV, M.; KOVSH, A.; USTINOV, V.; EGOROV, A. Y. ; ZHUKOV, A.. **Metastable population of self-organized InAs/GaAs quantum dots.** Journal of electronic materials, 28(5):491–495, 1999.
- [64] NOWOZIN, T.; MARENT, A.; BONATO, L.; SCHLIWA, A.; BIMBERG, D.; SMAKMAN, E.; GARLEFF, J.; KOENRAAD, P.; YOUNG, R. ; HAYNE, M.. **Linking structural and electronic properties of high-purity self-assembled GaSb/GaAs quantum dots.** Physical Review B, 86(3):035305, 2012.
- [65] BIRNER, S.; ZIBOLD, T.; ANDLAUER, T.; KUBIS, T.; SABATHIL, M.; TRELLAKIS, A. ; VOGL, P.. **Nextnano: general purpose 3-D simulations.** IEEE Transactions on Electron Devices, 54(9):2137–2142, 2007.
- [66] ANTOLÍN, E.; MARTI, A.; FARMER, C.; LINARES, P.; HERNÁNDEZ, E.; SÁNCHEZ, A.; BEN, T.; MOLINA, S.; STANLEY, C. ; LUQUE, A.. **Reducing carrier escape in the InAs/GaAs quantum dot intermediate band solar cell.** Journal of Applied Physics, 108(6):064513, 2010.
- [67] LINARES, P.; FARMER, C.; ANTOLÍN, E.; CHAKRABARTI, S.; SÁNCHEZ, A.; BEN, T.; MOLINA, S.; STANLEY, C.; MARTÍ, A. ; LUQUE, A.. **In(GaAl)As quaternary alloys for quantum dot intermediate band solar cells.** Energy Procedia, 2(1):133–141, 2010.

- [68] MARTÍ, A.; LOPEZ, N.; ANTOLIN, E.; CANOVAS, E.; LUQUE, A.; STANLEY, C.; FARMER, C. ; DIAZ, P.. **Emitter degradation in quantum dot intermediate band solar cells.** Applied Physics Letters, 90(23):233510, 2007.
- [69] SAMUELSON, L.; TITZE, P. O. ; GRIMMEISS, H.. **Electrical and optical properties of deep levels in MOVPE grown GaAs.** Journal of Crystal Growth, 55(1):164–172, 1981.
- [70] POLOJÄRVI, V.; SCHRAMM, A.; AHO, A.; TUKIAINEN, A. ; GUINA, M.. **Removal of strain relaxation induced defects by flushing of InAs quantum dots.** Journal of Physics D: Applied Physics, 45(36):365107, 2012.
- [71] THOMPSON, W. J.. **Numerous neat algorithms for the voigt profile function.** Computers in physics, 7(6):627–631, 1993.
- [72] BRAMMERTZ, G.; MOLS, Y.; DEGROOTE, S.; MOTSNYI, V.; LEYS, M.; BORGHS, G. ; CAYMAX, M.. **Low-temperature photoluminescence study of thin epitaxial GaAs films on Ge substrates.** Journal of applied physics, 99(9):093514, 2006.
- [73] GALIEV, G.; KLIMOV, E.; KLOCHKOV, A.; PUSHKAREV, S. ; MALTSEV, P.. **Photoluminescence studies of Si-Doped epitaxial GaAs films grown on (100) and (111) a-oriented GaAs substrates at lowered temperatures.** Semiconductors, 52(3):376–382, 2018.
- [74] KROTKUS, A.; MARCINKEVIČIUS, S. ; VISELGA, R.. **Ultrafast photoluminescence decay in GaAs grown by low-temperature Molecular-Beam-Epitaxy.** In: HOT CARRIERS IN SEMICONDUCTORS, p. 113–115. Springer, 1996.
- [75] AMO, A.; MARTÍN, M.; VIÑA, L.; TOROPOV, A. ; ZHURAVLEV, K.. **Interplay of exciton and electron-hole plasma recombination on the photoluminescence dynamics in bulk GaAs.** Physical Review B, 73(3):035205, 2006.
- [76] THURMOND, C.. **The standard thermodynamic functions for the formation of electrons and holes in Ge, Si, GaAs, and GaP.** Journal of the Electrochemical Society, 122(8):1133–1141, 1975.
- [77] LAUTENSCHLAGER, P.; GARRIGA, M.; LOGOTHETIDIS, S. ; CARDONA, M.. **Interband critical points of GaAs and their temperature dependence.** Physical Review B, 35(17):9174, 1987.

- [78] OZEKI, M.; NAKAI, K.; DAZAI, K. ; RYUZAN, O.. **Photoluminescence study of carbon-doped Gallium Arsenide.** Japanese Journal of Applied Physics, 13(7):1121, 1974.
- [79] SZE, S. M.. **Physics of semiconductor devices**, chapter 2, p. 30. John Wiley and Sons, Inc., New York, first edition, 1969.
- [80] TANG, X.; LOCHS, H.; HAGEMAN, P.; DE CROON, M.; GILING, L. ; BONS, A.. **Si-doping of MOCVD GaAs: Closer analysis of the incorporation process.** Journal of crystal growth, 98(4):827–837, 1989.
- [81] BAEUMLER, M.; MAIER, M.; HERRES, N.; BÜNGER, T.; STENZENBERGER, J. ; JANTZ, W.. **2K PL topography of silicon doped VGF GaAs wafers.** Materials Science and Engineering: B, 91:16–20, 2002.
- [82] XIE, H.; PRIOLI, R.; TORELLY, G.; LIU, H.; FISCHER, A.; JAKOMIN, R.; MOURÃO, R.; KAWABATA, R.; PIRES, M.; SOUZA, P. ; OTHERS. **Correlation between size distribution and luminescence properties of spool-shaped InAs quantum dots.** Semiconductor Science and Technology, 32(5):055013, 2017.
- [83] GRUNDMANN, M.; LEDENTSOV, N.; STIER, O.; BIMBERG, D.; USTINOV, V.; KOP'EV, P. ; ALFEROV, Z. I.. **Excited states in self-organized InAs/GaAs quantum dots: theory and experiment.** Applied physics letters, 68(7):979–981, 1996.
- [84] LUQUE, A.; MARTI, A.. **The intermediate band solar cell: progress toward the realization of an attractive concept.** Advanced Materials, 22(2):160–174, 2010.
- [85] GARCIA, J.; MEDEIROS-RIBEIRO, G.; SCHMIDT, K.; NGO, T.; FENG, J.; LORKE, A.; KOTTHAUS, J. ; PETROFF, P. M.. **Intermixing and shape changes during the formation of InAs self-assembled quantum dots.** Applied physics letters, 71(14):2014–2016, 1997.
- [86] BABIŃSKI, A.; JASIŃSKI, J.; BOŹEK, R.; SZEPIELOW, A. ; BARANOWSKI, J.. **Rapid thermal annealing of InAs/GaAs quantum dots under a GaAs proximity cap.** Applied Physics Letters, 79(16):2576–2578, 2001.

A Emission rate spectra from Laplace DLTS measurements

The following figures are the emission rate spectra in the form of color maps of all the samples studied in this work. The characteristics of these figures were described in section 3.2. The defects detected and identified by Laplace DLTS are indicated by symbols on the figures. The data points highlighted by these symbols correspond to the data points included in the respective Arrhenius plots of section 4.2. Also, the reverse voltage at which each spectrum was obtained is specified in brackets in the legends, except for the individually doped GaAs samples which were measured only at -1 V.

PUC-Rio - Certificação Digital Nº 1412785/CA

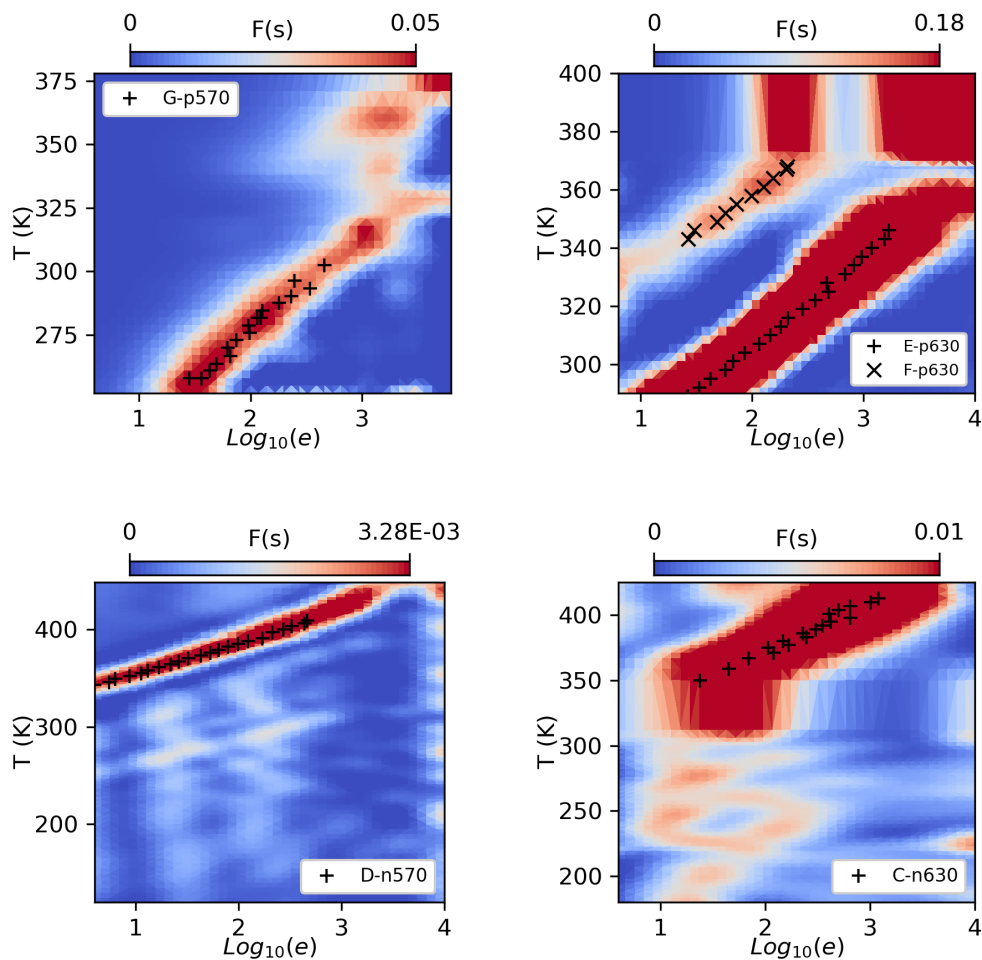


Figure A.1: Emission rate spectra of the individually doped GaAs samples p570, p630, n570, and n630 taken at -1 V.

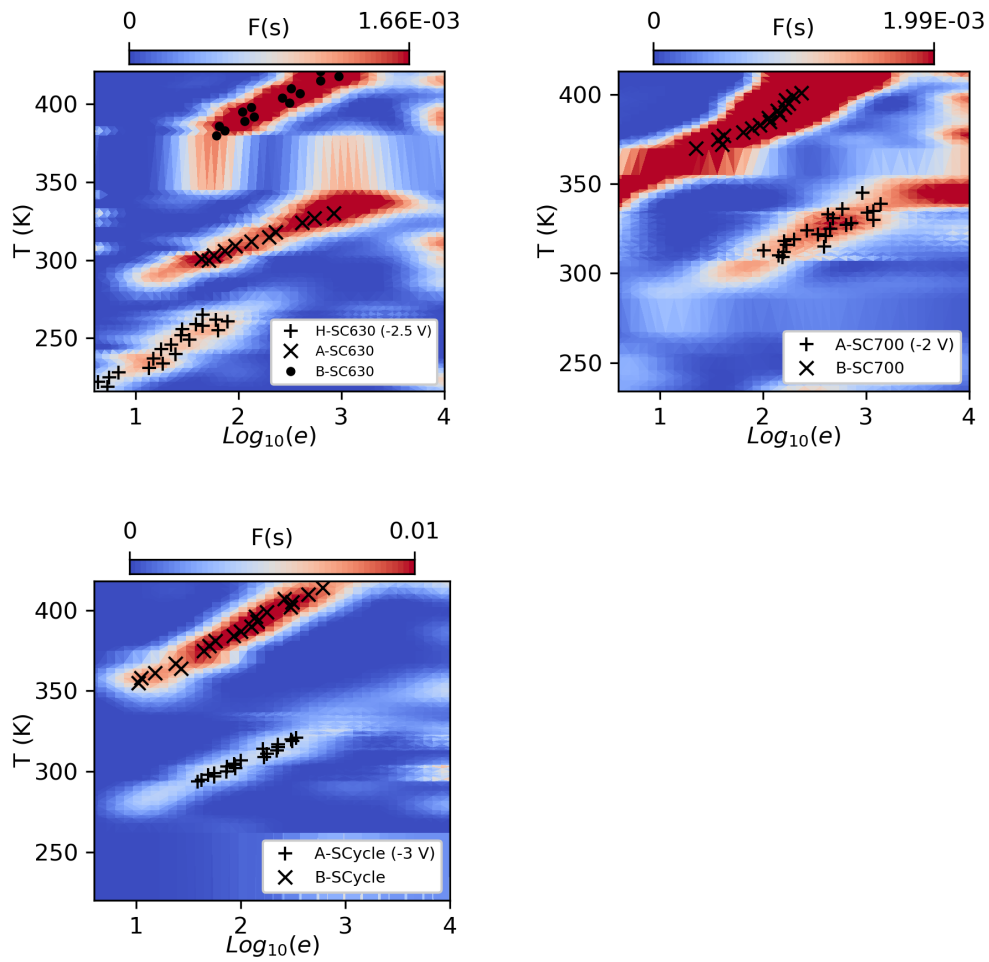


Figure A.2: Emission rate spectra of the solar cells without QDs (SC630, SC700, and SCycle).

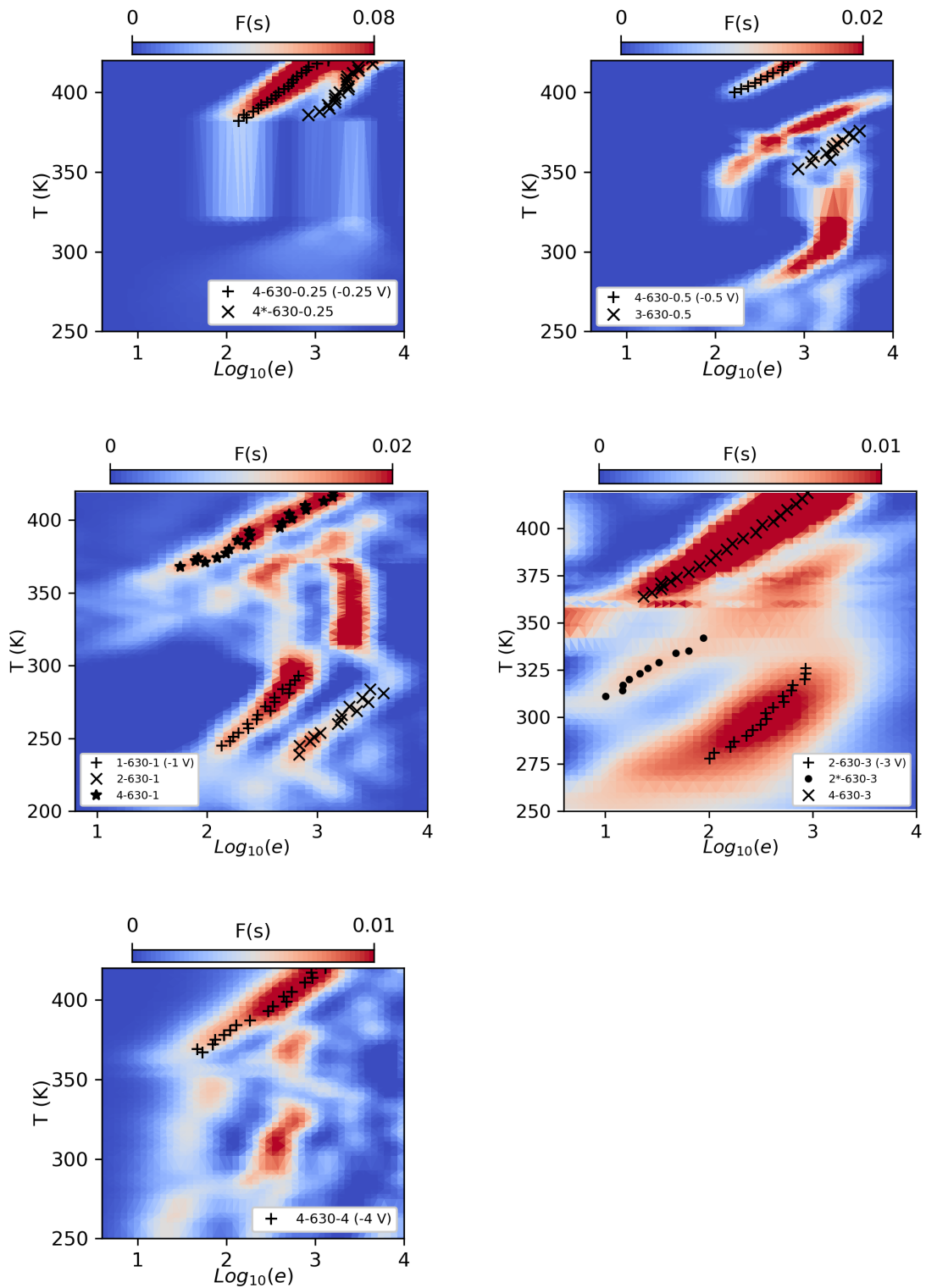


Figure A.3: Emission rate spectra of solar cell QD630 taken at different reverse voltages.

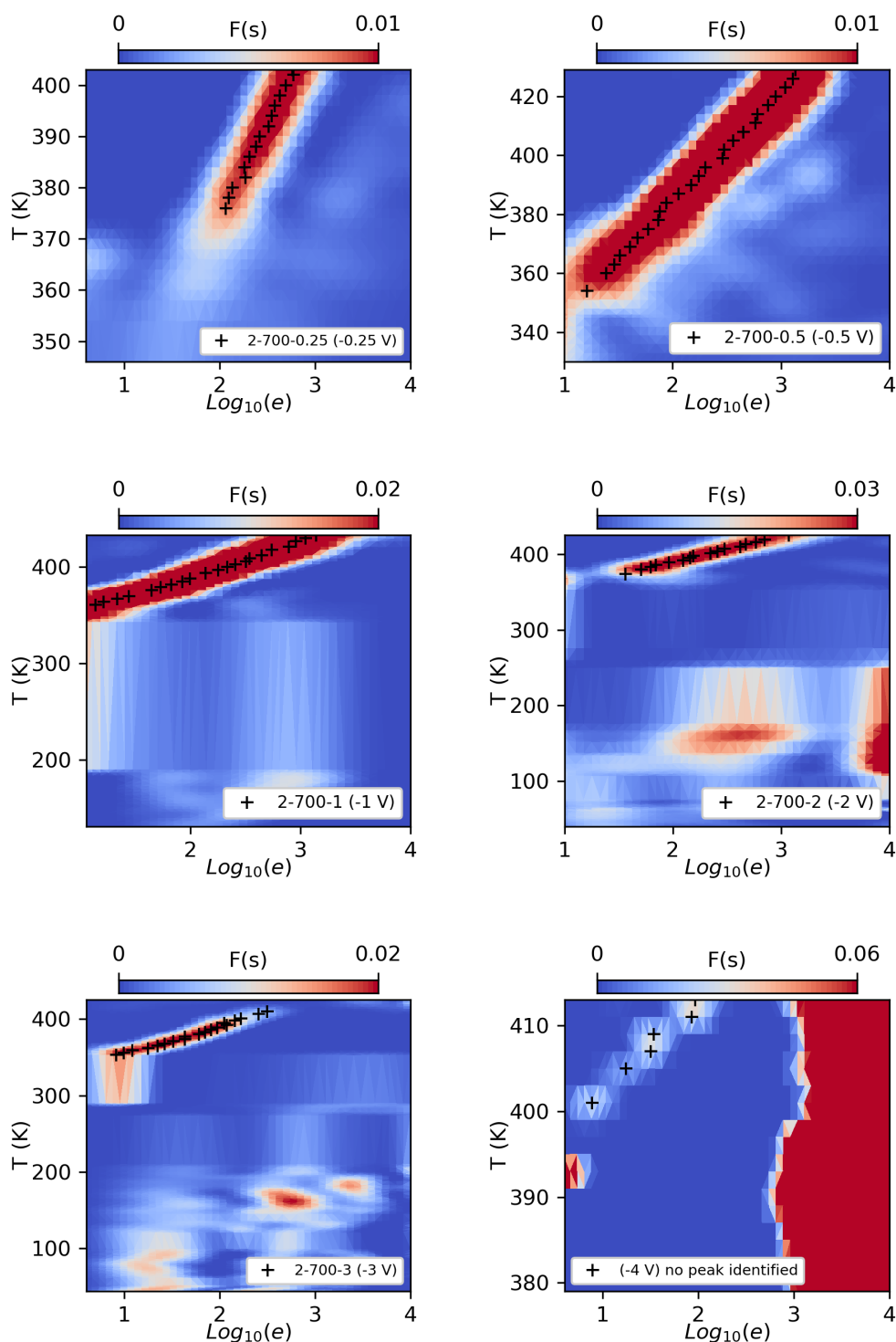


Figure A.4: Emission rate spectra of solar cell QD700 taken at different reverse voltages. The spectrum at -4 V (lower right figure) did not show clearly the peak 2-700-4 measured by DLTS around 400 K .

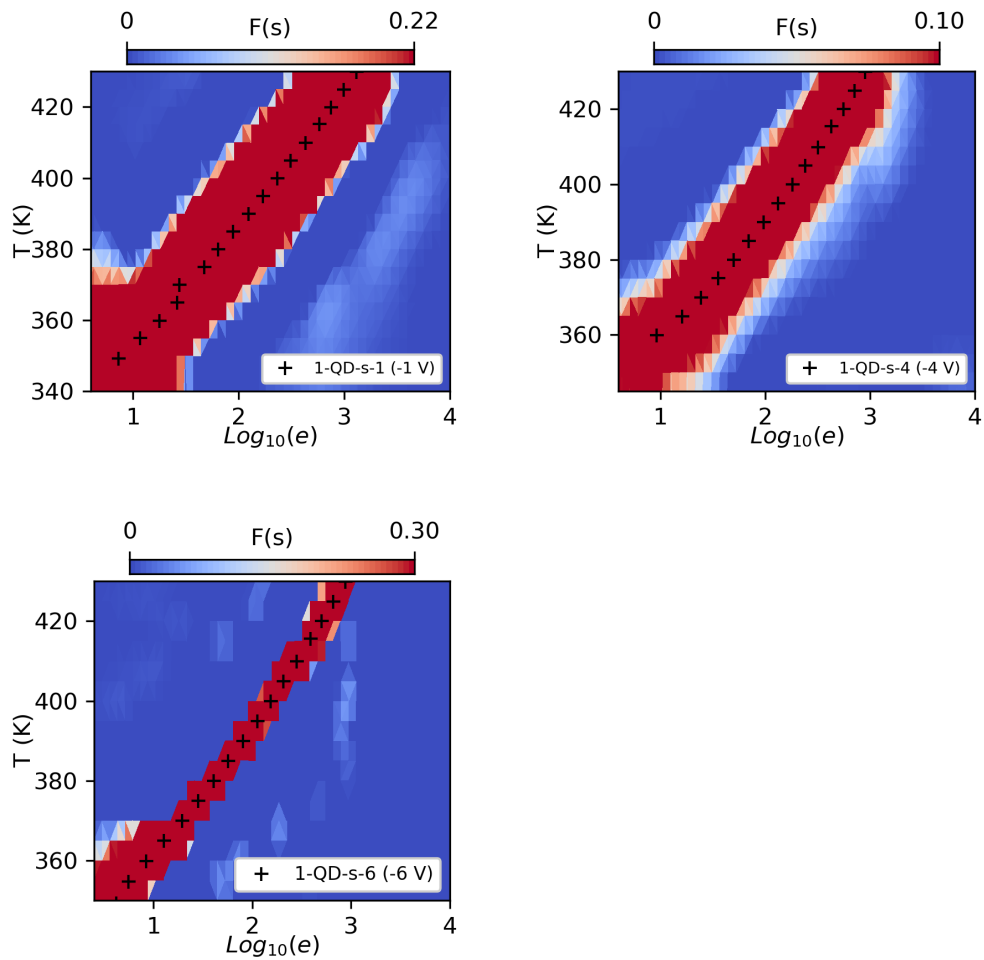


Figure A.5: Emission rate spectra of solar cell QD-s-700 taken at different reverse voltages.